
Electronic Thesis and Dissertation Repository

4-4-2024 1:45 PM

Optimization of Full-Inversion Techniques Towards Clinical Ultrasound Elastography

Matthew A. Caius, *Western University*

Supervisor: Samani, Abbas, *The University of Western Ontario*

A thesis submitted in partial fulfillment of the requirements for the Master of Engineering Science degree in Biomedical Engineering

© Matthew A. Caius 2024

Follow this and additional works at: <https://ir.lib.uwo.ca/etd>



Part of the [Bioimaging and Biomedical Optics Commons](#), and the [Biomechanics and Biotransport Commons](#)

Recommended Citation

Caius, Matthew A., "Optimization of Full-Inversion Techniques Towards Clinical Ultrasound Elastography" (2024). *Electronic Thesis and Dissertation Repository*. 10032.
<https://ir.lib.uwo.ca/etd/10032>

This Dissertation/Thesis is brought to you for free and open access by Scholarship@Western. It has been accepted for inclusion in Electronic Thesis and Dissertation Repository by an authorized administrator of Scholarship@Western. For more information, please contact wlsadmin@uwo.ca.

Abstract

Breast cancer is one of the most common cancers, representing 25% of all new cancers and 13% of all cancer related deaths in Canadian women. Early detection before treatment of breast cancer is paramount as survival rates decrease significantly over time. Some of the most common diagnostic and screening procedures include breast manual examination, X-ray mammography, ultrasonography, and magnetic resonance imaging (MRI). These methods are either unreliable, associated with dangerous ionization or too costly, while they all have difficulty differentiating malignant tumors from benign ones without a follow-up biopsy. One technique that has shown a potential to minimize the number of biopsy cases is ultrasound elastography (USE), which images the breast tissue stiffness that is known to be substantially different for normal and pathological tissue.

One of the issues plaguing USE is the lack of data quality due to input tissue displacement data quality and quantity. This data are obtained through processing radio-frequency data acquired at two compression states of the tissue that need to be acquired under the same ultrasound probe orientation to ensure high quality tissue stiffness image. Moreover, there exists no objective and automatic way to assess the quality and consistency of radio-frequency acquired throughout USE. Furthermore, methods capable of producing high-quality lateral displacements are limited. These issues compromise the practical utility of USE in clinical settings. As such, part of this research was dedicated to address these issues. This thesis introduces methodologies to tackle these issues, with the aim of optimizing USE for real time clinical settings, hence allowing reliable breast cancer assessment. It also introduces a series of metrics that can be used to objectively measure data quality. Finally, an open-source software solution was developed to guarantee data quality by generating it in-silico to facilitate the development and assessment of new displacement estimators.

Keywords

Elastography, Breast Cancer, Liver Cancer, Oncology, Ultrasound, Finite Element Modelling, Open-Source Software

Summary for Lay Audience

Breast cancer is one of the most common cancers, representing 25% of all new cancers and 13% of all cancer-related deaths in Canadian women. Early detection to enable treatment of breast cancer is paramount as survival rates decrease significantly over time. Some of the most common diagnostic and screening procedures include breast manual examination, X-ray mammography, ultrasonography and Magnetic Resonance Imaging (MRI). These methods are either unreliable, associated with dangerous ionization or too costly while they all have difficulty detecting or differentiating malignant tumors from benign ones without a follow-up biopsy. One technique that has shown a potential to minimize the number of biopsy cases is ultrasound elastography, which images the breast tissue stiffness that is known to be substantially different for normal and pathological tissue.

To perform ultrasound elastography, the clinician needs to take two ultrasound images, one before applying pressure, and one after applying pressure manually through the ultrasound probe. The differences between these two images are captured by an algorithm called a displacement estimator, which is then used to calculate tissue stiffness. One of the issues with this technique, however, is that it is almost impossible to guarantee that the pair of image frames will result in good quality stiffness imaging data without manually assessing the resulting images, making it too labor intensive to be used in the clinical setting. Moreover, it makes developing new algorithms difficult, as it can be nearly impossible to determine if the algorithm has failed, or the quality of the data is insufficient. Another relevant issue is most current displacement estimators fail to capture the tissue displacement completely, hence further degrading the stiffness image quality.

This thesis introduces methodologies to tackle these issues, towards developing accurate and real-time breast-stiffness imaging technique, which allows for effective breast cancer assessment. It also introduces a series of metrics that can be used to objectively measure data quality. Finally, an open-source software solution was developed to guarantee data quality by generating it completely on the computer to facilitate the development and assessment of new displacement estimation techniques.

Co-Authorship Statement

The major contributors are Matthew Caius and Dr. Abbas Samani where Matthew Caius was the first author who wrote the initial draft of the manuscript and developed all the code. Dr. Samani was responsible for conceiving ideas and consultation for algorithms development, supervision, and editing the manuscripts. Chapter 2 has been published in the Journal of Applied Sciences and Chapters 3 and 4 are in the editing process to be published.

Caius M, Samani A. Comparative Study of Ultrasound Tissue Motion Tracking Techniques for Effective Breast Ultrasound Elastography. *Applied Sciences*. 2023; 13(21):11912. <https://doi.org/10.3390/app132111912>

Acknowledgements

I would like to acknowledge my supervisor, Dr. Abbas Samani for his guidance and advice throughout the development and writing of this thesis, along with my advisory committee members, Dr. Aaron Fenster, and Dr. Jeffery Carson for their invaluable advice. I would like to acknowledge and thank Amal Aziz for her help in implementing some of the code using my algorithms and Jonah Boutin for his help in debugging Elastosynth and generating some figures. A special thanks to Dr. Hassan Rivaz's group for their help in debugging FIELD II. Moreover, I would like to thank Dr. Niusha Kheirkhah as my work expands on her dissertation. Finally, I would like to thank my lab members Xi Feng, Halimah Alsurayhi, Tristan Curry, and Jonah Boutin for their help and support.

Table of Contents

Abstract	i
Summary for Lay Audience.....	ii
Co-Authorship Statement.....	iii
Acknowledgements.....	iv
Table of Contents	v
List of Tables	ix
List of Figures	xi
Table of Abbreviations	xvii
Chapter 1	1
1 Introduction	1
1.1 Breast Cancer Statistics and Screening.....	1
1.2 Introduction to Elastography.....	2
1.3 Introduction to Ultrasound Physics.....	4
1.3.1 Sound Propagation	4
1.3.2 Piezoelectric Effect and Transducer Design	6
1.3.3 Ultrasound Image Formation	7
1.4 In-Silico Ultrasound Image Generation	7
1.5 Time Delay Estimation	9
1.6 Theory of Elasticity.....	11
1.7 Regularization	13
1.7.1 Mathematical Regularization.....	13
1.7.2 Tissue-Mechanics Based Regularization	14

1.8	Iterative Reconstruction	15
1.8.1	The Finite-Element Method.....	16
1.8.2	Iterative Reconstruction of the Young’s Modulus.....	16
1.9	Overview of Current Issues	18
1.10	Research Objectives.....	19
1.11	Thesis Outline	19
1.11.1	Chapter 2: Categorization and Comparison of Displacement Estimators at the Full Stiffness Reconstruction Level.....	19
1.11.2	Chapter 3: Elastosynth - An Open-Source software package for the generation of realistic in-silico data for ultrasound elastography	20
1.11.3	Chapter 4: A Method to Quantitatively Assess the Quality of Displacement Estimations.....	20
1.11.4	Chapter 5: Discussion and Conclusions.....	21
1.12	References.....	21
	Chapter 2.....	30
2	Comparative Study of Ultrasound Tissue Motion Tracking Techniques for Effective Breast Ultrasound Elastography	30
2.1	Introduction.....	30
2.2	Methods.....	31
2.2.1	Strain Refinement Algorithm.....	31
2.2.2	Data Generation	32
2.2.3	Displacement Estimators	33
2.2.4	Young’s Modulus and Data Processing.....	34
2.3	Results.....	35
2.4	Discussion.....	50
2.5	Conclusion	56
2.6	References.....	56

Chapter 3	60
3 Elastosynth – An Open-source software package for the generation of realistic in-silico data for ultrasound elastography	60
3.1 Introduction	60
3.2 Background	61
3.3 Design Considerations	62
3.4 Methods and Capabilities.....	63
3.4.1 Procedural Phantom Generation	63
3.4.2 Finite Element Modelling	66
3.4.3 Generation of Radiofrequency Data	67
3.5 Comparison to Clinical Data.....	68
3.6 Optimization Procedure	69
3.7 Supported Workflows	70
3.8 Discussion and Significance	71
3.9 Hardware/Software Specification and Distribution	72
3.10 References	73
Chapter 4.....	78
4 Data Quality Analyzer – Towards Optimal Radio-frequency Frame Pair Selection for Ultrasound Elastography	78
4.1 Introduction.....	78
4.2 Methods.....	80
4.2.1 Overview of Proposed Method	80
4.2.2 Evaluation Algorithm.....	81
4.2.3 Synthetic Data, Tissue Mimicking and Clinical Data.....	81
4.3 Results.....	83
4.4 Discussion	90

4.5 References	93
Chapter 5	97
5 Conclusions and Future Work.....	97
5.1 Chapter 3 – A Comparison of Displacement Estimators	97
5.2 Chapter 4 – Elastosynth - An Open-Source software package for the generation of realistic in-silico data for ultrasound elastography	98
5.3 Chapter 5 - Data Quality Analyzer – Towards Optimal Radio-frequency Frame Pair Selection for Ultrasound Elastography	99
5.4 Future Work	100
5.4.1 Chapter 2	100
5.4.2 Chapter 3	100
5.4.3 Chapter 4	101
5.5 Closing Remarks	102
6 Curriculum Vitae.....	103

List of Tables

Table 2.1 Specificity, sensitivity, and kappa statistics for the agreement of thresholded inclusions of each displacement estimator compared to the ground truth.	37
Table 2.2 CNR, SNR, and inclusion to background Young's Modulus ratio values obtained for reconstructed Young's Modulus images of phantoms computed using each displacement estimator with and without STREAL.	39
Table 2.3 CNR and SNR values obtained for axial strain images of tissue mimicking phantom computed using each displacement estimator with and without STREAL.....	41
Table 2.4 CNR and SNR values obtained for lateral strain image of the tissue mimicking phantom computed using each displacement estimator with and without STREAL.....	42
Table 2.5 CNR, SNR and Inclusion to background ratios obtained for stiffness images of Patient 1 computed using each displacement estimator with and without STREAL.	44
Table 2.6 CNR, SNR and inclusion to background ratio values obtained for axial strain images of Patient 2 computed using each displacement estimator with and without STREAL.	46
Table 2.7 CNR, SNR, and inclusion to background values obtained for stiffness images of Patient 3 computed using each displacement estimator with and without STREAL ...	48
Table 3.1 An overview of the three major modules contained within Elastosynth. Each module has a specific task and can be used independently of each other. The first is the procedural phantom generator, which is used to generate phantom geometry based on parameters provided. The second module performs finite element modelling, which is responsible for simulating the compression of the phantom. The final module generates the radiofrequency data using FIELD II.	63
Table 4.1 Mean MSE and Correlation for top 5 and bottom 5 frame pairs for clinical examples 1 and 2, as can be seen, there is a considerable difference in error metrics between the two groups	90

List of Figures

Figure 1.1 An illustration of absorption, reflection, scattering and refraction due to sound waves propagating through media; figure taken from [56].	5
Figure 1.2 An illustration of the changing charge distribution that causes the piezoelectric effect. Either by applied mechanical force or an electric field. The figure is taken from [57]......	6
Figure 1.3 Sample RF data image acquired from a breast cancer case along with corresponding B-Mode ultrasound image	7
Figure 1.4 Sample pressure wave emission for a curvilinear probe. This process was performed with the open-source software FIELD II [59][60].	9
Figure 1.5 An illustration of time delay estimation on radiofrequency data taken from [61]. $\mathbf{y1}(t)$ and $\mathbf{y2}(t)$ are the RF – signals from the pre- and post-compression images that correspond to the same portion of the image. T_s represents the sampling time for the RF signal (which has been interpolated).....	10
Figure 1.6 An illustration of the mechanical stresses described in Hooke’s law illustrating the different modes of stress and strain that can occur in each direction. Note that shearing can occur in any combination of directions as well. This figure was taken from https://dewesoft.com/blog/measure-strain-and-pressure	12
Figure 1.7 An overview of the iterative reconstruction algorithm used to calculate the Young’s modulus of the tissue being studied. This is an iterative technique whereby the Young’s modulus is calculated by repeatedly simulating the stress field and recalculating the E field using Hooke’s law until convergence is achieved.	17
Figure 2.1 An overview of the STREAL methodology and its 3-step process. The first step is a second order derivative filtering procedure. The second step enforces the incompressibility of tissue. The third step enforces the compatibility of tissue (no	

apparent tearing). Note that this procedure requires an estimate of out-of-plane deformation. Figure taken from [7].	32
Figure 2.2 Errors in reconstructed inclusion-to-background Young’s modulus ratios, Hausdorff distances between truth and reconstructed outlines of the inclusion, and MSE between ground truth and reconstructed Young’s modulus images obtained using the four displacement estimation methods of AM2D, GLUE, OVERWIND, and SOUL with and without STREAL, The red and blue lines with stars indicate statistical significance ($p < 0.05$) between results generated by pairs of estimators. In this comparison, pre- and post-STREAL were separate groups; hence, the statistical comparisons are between estimators, not pre- and post-STREAL.....	36
Figure 2.3 An example of Young’s modulus image reconstruction obtained with synthetic displacement data generated by each displacement field estimator with and without STREAL enhancement. The “ground truth” reconstruction image was obtained by processing the ground truth displacement field using the iterative Young’s modulus reconstruction algorithm.	38
Figure 2.4 Reconstructed Young’s modulus images of a tissue mimicking phantom obtained with each displacement estimator with and without STREAL enhancement. ...	38
Figure 2.5 Axial Strain Images of the tissue mimicking phantom obtained using each displacement field estimator applied with and without STREAL enhancement. The differences between each image and its STREAL version are subtle.	40
Figure 2.6 Lateral strain images of the tissue mimicking phantom obtained using each displacement field estimator applied with and without STREAL. Lateral strain images obtained with STREAL enhanced show remarkable improvement over their pre-enhancement counterparts.....	42
Figure 2.7 Reconstructed Young’s modulus images of Patient 1 computed from displacement fields obtained by each displacement estimator with and without STREAL. Approximate tumor ROI is highlighted in red based on outlines provided in [2]. AM2D provides reasonably high-quality images at a very low computational cost.	43

- Figure 2.8 Axial strain images of Patient 1 computed from displacement fields obtained by each displacement estimator with and without STREAL. AM2D provides reasonably high-quality images at a very low computational cost..... 44
- Figure 2.9 Lateral strain images of Patient 1 computed from displacement fields obtained by each displacement estimator with and without STREAL. AM2D with STREAL provides reasonably high-quality images at a very low computational cost. 45
- Figure 2.10 Reconstructed Young’s modulus images of Patient 2 computed from displacement fields obtained by each displacement estimator with and without STREAL. Approximate tumor ROI is highlighted in red [2]. AM2D provides a reasonably high-quality image at a very low computational cost..... 45
- Figure 2.11 Axial strain images of Patient 2 computed from displacement fields obtained by each displacement estimator with and without STREAL. AM2D provides reasonably high-quality images at a very low computational cost..... 46
- Figure 2.12 Lateral strain images of Patient 2 computed from displacement fields obtained by each displacement estimator with and without STREAL. AM2D with STREAL provides reasonably high-quality images at a very low computational cost. ... 47
- Figure 2.13 Reconstructed Young’s modulus images of Patient 3 computed from displacement fields obtained by each displacement estimator with and without STREAL. Approximate tumor ROI is highlighted in red [2]. AM2D provides a reasonably high-quality image at a very low computational cost..... 47
- Figure 2.14 Axial strain images of Patient 3 computed from displacement fields obtained by each displacement estimator with and without STREAL. AM2D provides reasonably high-quality images at a very low computational cost..... 48
- Figure 2.15 Lateral strain images of Patient 3 computed from displacement fields obtained by each displacement estimator with and without STREAL. AM2D with STREAL provides reasonably high-quality images at a very low computational cost. ... 49

Figure 2.16 B-Mode images alongside Segmented Young’s modulus images computed from displacements estimated through the AM2D estimator with STREAL, which are overlaid on top of B-mode images of a) and b) Patients 1, c) and d) Patient 2 and e) Patient 3. Highlighted are regions with Young’s modulus values larger than 1.5 times the median of Young’s modulus of respective background tissue. Apart from artefacts at the top of the images, the stiffness elevation in the tumor area is consistent with their respective ROIs. Moreover, the stiffness image reveals features that are not immediately obvious from the B-Mode. 50

Figure 2.17 A hypothetical flow chart for a real-time US elastography system that could be deployed in the clinical setting. The red box indicates a real-time loop that the clinician can use to assess the quality of images in real time, where once a sufficiently high-quality strain image is found, it can be processed to reconstruct a reliable Young’s modulus image. 53

Figure 3.1 The algorithm used to generate randomized inclusion locations for the elastography phantom uses a Monte-Carlo approach to finding valid locations. 64

Figure 3.2 Generation of a heterogenous stiffness field from an initially homogenous image (a). This was achieved through a three step process which begins with noise contamination of the homogenous phantom (b), followed by superpixel segmentation and then further changing the superpixel E values which results in a heterogenous phantom (c). 65

Figure 3.3 Finite element simulation of the phantom illustrated in Figure 3.2. See Figure 4.1 for strain images simulated using a homogenous sample. 67

Figure 3.4 Scatterer displacements used to move the scatterers in the generation of the second frame. These were taken from the finite element simulation and resampled to the location of the randomly generated scatterers. 68

Figure 3.5 A comparison of Young’s modulus reconstruction using clinical data (a) with a tumor in the circled ROI versus a reconstruction with a synthetic data sample (b). As

can be seen, both images show very similar heterogeneity patterns, illustrating that heterogeneity has been effectively captured.	69
Figure 3.6 Displacement estimation using synthetic data where 100% (a), 1% (b), 0.7% (c), and 0.5% (c) of the scatterers are used, as can be seen, an artefact only appears at 0.7%, which means 1% can be safely used.	70
Figure 3.7 Currently supported workflows. The main workflow includes starting from a parameter dataset and flowing through the whole generation pipeline. However, at every opportunity, the user may input custom data into the process to avoid earlier steps, allowing for manual and custom phantom generation.	71
Figure 4.1 Axial and Lateral strain images for the ground truth finite element phantom with Young's Moduli X and Y for the inclusion and background, respectively.	82
Figure 4.2 Metrics of quality as the out-of-plane displacement increases (standard deviation of out-of-plane displacement in mm) for the synthetic data. As the out-of-plane corruption increases, SNR and CNR become unreliable, while MSE and Correlation scores progressively get worse. Interestingly, at higher corruption levels we see less consistent trends.	83
Figure 4.3 The progressive degradation of axial strain image quality and increased artefacts with increasing out-of-plane displacement data corruption of synthetic phantoms. The artefacts appear in the form of unrealistically high- and low-strain areas.	84
Figure 4.4 Correlation without warping shows a similar pattern to the warped correlation where correlation and mean squared error become progressively worse with increased out-of-plane displacement. Without warping however, the values for the errors are much less convincing, as correlation starts at 0.16. Therefore, warped correlation is a much more robust method than naïve correlation.	85
Figure 4.5 B-Mode image of the patient breast tumour, segmented by a clinician.	86

Figure 4.6 First clinical example for top 5 ranked frame-pairs (top) and bottom-5 frame-pairs (bottom row) as can be seen the low bottom 5 frame-pairs are inferior compared to the top 5. The tumour boundary is outlined in white.	86
Figure 4.7 The histogram of mean squared error and correlation coefficients for each pair in clinical example 1. For this example, the majority of pairs are at least passable in terms of correlation coefficients, with the standard taken arbitrarily at 0.5 correlation and 1.4 MSE.	87
Figure 4.8 B-Mode image of the patient breast tumour, segmented by a clinician.	88
Figure 4.9 Second clinical example for top 5 ranked frame-pairs (top) and bottom-5 frame-pairs (bottom row) as can be seen the low bottom 5 frame-pairs are inferior compared to the top 5. The tumour boundary is outlined in white.	88
Figure 4.10 The histogram of mean squared error and correlation coefficients for each pair in clinical example 1. For this particular example, the majority of pairs are of very low quality and should not be used for elastography, with the standard taken arbitrarily at 0.5 correlation and 1.4 MSE.	89

Table of Abbreviations

MRI	Magnetic Resonance Imaging
CNR	Contrast-to-Noise Ratio
SNR	Signal-to-Noise Ratio
STREAL	Strain Enhancement Algorithm
MSE	Mean-Squared-Error
AM2D	Analytic Minimization in 2D
GLUE	Global Ultrasound Elastography
OVERWIND	Total Variation Regularization and Window-Based Time Delay Estimation
SOUL	Second-Order Ultrasound Elastography
USE	Ultrasound Elastography
QUSE	Quasi-Static Ultrasound Elastography
RF	Radiofrequency

Chapter 1

1 Introduction

All figures in this chapter that are taken from other sources have been released under the creative commons license, or permission has been acquired from the respective copyright holders.

1.1 Breast Cancer Statistics and Screening

Breast cancer is one of the most common cancers, representing 25% of all new cancers and 13% of all cancer deaths in Canadian women [1]. Worldwide, breast cancer represents 1 in 8 cancer diagnoses with a total of 2.3 million diagnoses across both sexes along with 685 000 deaths [2]. These numbers are predicted to increase to 3 million and 1 million respectively, by 2040. Breast cancer is a cancer in which the stage of disease influences the 5-year survival rate massively. This survival rate ranges from nearly 100% down to <30% depending on the localization, covering local to metastatic breast cancers [3]. Therefore, screening procedures need to be robust, to attempt to capture these tumours as early as possible.

To catch these cancers as early as possible, many countries and organizations have created screening methodologies and guidelines for clinicians to follow [4], [5]. Guidelines vary but in general screening starts around the age of 50 years with X-ray mammography for average risk populations, though some guidelines recommend starting screening at the age of 40. For high-risk populations who have confirmed gene mutation or have had genetic counseling determining that they are at high risk for breast cancer, screening starts at the age of 30 years. For both groups, the major method is X-ray mammography, but in the high-risk category, supplemental screening is recommended, usually with MRI or breast ultrasound if the MRI is not appropriate. In general, MRI is very good for assessing the potential for surgery and the capability to get good margins around the tumour. Unfortunately, MRI is a very costly imaging technology which also results in a larger

number of false positive outcomes that represent lesions suspected to be malignant but are later proven to be benign [6], [7]. Ultrasound on the other hand, is an inexpensive and convenient modality that is effective at detection of breast cancer [8], [9]. In either scenario, secondary screening is recommended in high-risk individuals and those with dense breasts.

Moreover, there are other diseases which can benefit from the use of USE, namely liver cancer, which is the 5th most common cancer in men, and 8th most common in women, with total incidence per year at 564 000 cases per year, where rates in men are 2-4 times higher compared to women [10].

Screening for liver cancer is also a common practice, although for a much more restricted patient population, namely those with cirrhosis and hepatitis, to check for presence of tumours. The usual screening protocol involves ultrasonography and alpha-fetoprotein [11], which implies that the integration of elastography into the screening workflow would be trivial. Note that while transient elastography is currently being used in the diagnosis of fatty liver disease and other liver conditions, this diagnosis criteria is based on an absolute value for the stiffness of the liver, which quasi-static elastography cannot provide as it can only image the stiffness ratio.

1.2 Introduction to Elastography

One issue that is common in each screening procedure is a relatively low diagnosis accuracy without a follow-up biopsy. While minimally invasive biopsies are the gold standard, it is important to reduce the number of unnecessary biopsies, as imaging is entirely non-invasive, may be cheaper, while its results can be given immediately, reducing stress and accelerating time to treatment. One potential method to reduce the need for biopsy and allow for higher accuracy is elastography – imaging the stiffness of tissues via various means including MRI and ultrasound. This method is motivated by the fact that malignant tumors exhibit wildly different mechanical properties, including increased tissue stiffness and heterogeneity, which is necessary for their microenvironment adaptation and proliferation [12]–[33]. In general, there are many ways to perform elastography, each with their own strengths, weaknesses, and applications. One of the highest quality methods to

performing elastography is magnetic resonance elastography (MRE) [34]–[38]. Unfortunately, the issues with this method include low spatial resolution despite very high contrast-to-noise (CNR) – implying that larger lesions are easily seen while smaller lesions cannot be seen. Moreover, performing an MRI for breast or liver cancer screening is quite cost-prohibitive. USE on the other hand is cost effective and convenient to use, and has high spatial resolution, although it does not have very good CNR compared to MRE. In order to obtain high quality displacement estimates of the tissue, 3D USE has been performed with great success [39]–[42]. While high quality, 3D USE is less accessible than 2D USE. Unfortunately, 2D USE introduces complications due to the compression of a 3D problem into 2D, which makes development challenging. This generally means that assumptions need to be made about the 3D mechanical behavior of tissues based on the 2D image data. Moreover, if there is any out-of-plane movement during acquisition like sliding, it introduces data quality problems.

In 2D USE, there are two major methods: strain imaging and shear wave elastography. Strain imaging has two methodologies: quasi-static and acoustic radiation force imaging [43]–[45]. Both work on the same fundamental methodology, where the tissue is displaced by way of applied force, or by acoustic pulses generated by the probe (note that applied force may be internal movement such as blood pulsing). The advantage of this methodology is that the hardware required is relatively simpler and requires fewer assumptions than shear elastography. Shear wave elastography on the other hand generates shear waves propagating perpendicular to the ultrasound beam causing displacement stimulation [46], [47]. In this case, the speed of propagation of these tissue waves are measured and related to the shear modulus. In this case, the technique assumes that the tissue is linear, non-viscous and incompressible, which are not always reasonable assumptions and can lead to overestimation. One very large advantage to shear wave elastography techniques is that they provide quantitative measurement of the underlying shear modulus, whereas strain imaging can only give relative stiffness measurements at best. This makes shear wave elastography very well suited to diseases like hepatitis and fibrosis where an objective measurement is required [48], [49]. In the case of cancer, however, quasi-static and strain imaging allows for a good characterization of relative

stiffness. This investigation focuses on Quasi-static Ultrasound Elastography (QUSE), where the tissue is mechanically stimulated externally by the operator.

The methodology behind QUSE is generally a 3-step process:

1. Provide an initial rough estimate of the displacement based on the acquired radiofrequency (RF) data pre- and post-manual compression, generally with a correlation metric or dynamic programming [50], [51]. This can be done in real-time or via comparison of frame pairs in a recorded video.
2. Refine the resultant displacements and strains via some form of regularization [52]–[55].
3. Iteratively reconstruct the Young’s Modulus (E) to measure the relative stiffness of the tumor [55].

1.3 Introduction to Ultrasound Physics

Ultrasound imaging is a convenient, low-cost, non-ionizing imaging modality that leverages the propagation and reflection of sound from a tissue. In general, ultrasound is performed by using a probe which emits a series of sound waves to stimulate the tissue. Then, the same probe listens to sound waves coming out of the tissue in order to analyze the radiofrequency (RF) signals and turn it into an image (B-Mode image).

1.3.1 Sound Propagation

The propagation of sound within any given medium is governed by the acoustic wave equation, which is a second order partial differential equation derived from Newton’s law, the equation of state, continuity, conservation of mass, and the conservation of momentum. The derivation is omitted as it is out of scope, however the equation is shown as follows in general Laplacian form.

$$\nabla^2 P - \frac{1}{c_0^2} \frac{\partial^2 P}{\partial t^2} = 0 \quad 1.1$$

where P is the acoustic pressure, t is time, and c_0 is the speed of sound in the stimulated medium. The consequences of this equation result in various properties of sound as it passes a boundary between two different media as illustrated in Figure 1.1:

1. Absorption – Sound waves can be absorbed by the medium.
2. Reflection – Some sound waves bounce back toward the source.
3. Refraction – If the sound wave is incident on an angle compared to the normal of the surface being struck, the change in speed of sound will cause a change in wave direction.
4. Scattering – In a heterogenous medium, sound waves are scattered as a result of both reflection and refraction as the sound keeps interacting with different media

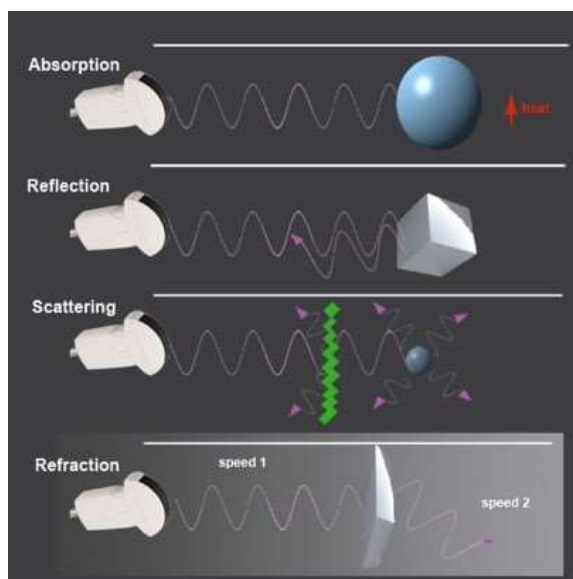


Figure 1.1 An illustration of absorption, reflection, scattering and refraction due to sound waves propagating through media; figure taken from [56].

Equation 1.1 is a simplified version of the true wave equation, which does not account for reflection, attenuation, scattering, and refraction, as it is a highly idealized version. However, it is included to give a general sense of the equation and concepts while the “true” wave equation is far more complicated with many more terms.

1.3.2 Piezoelectric Effect and Transducer Design

To produce the sound waves required for imaging, transducers are designed to use the piezoelectric effect, a physical phenomenon where electric signals are turned into mechanical signals and vice-versa, allowing the same array to both transmit and receive signals. In general, this effect is a consequence of a material's tendency to minimize internal energy. When an external electric field is applied, the piezoelectric material deforms, leading to force generation. The reverse is also true, when the crystal is deformed, a voltage is developed at the surface of the crystal, which can be measured. Figure 1.2 taken from [57] illustrates the piezoelectric effect.

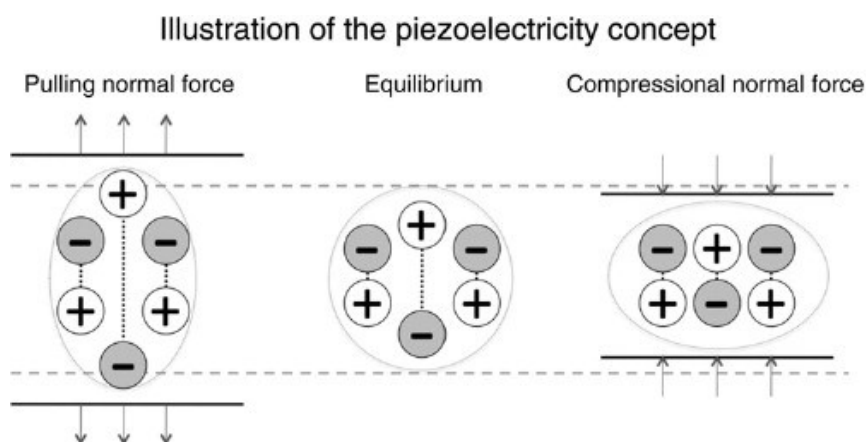


Figure 1.2 An illustration of the changing charge distribution that causes the piezoelectric effect. Either by applied mechanical force or an electric field. The figure is taken from [57].

To exploit this effect, transducers are designed with piezoelectric crystals arranged in a sensor array. Each sensor within the array is capable of both transmitting and receiving sound waves in the frequency range of 2 to 18 MHz [58]. While transducers are capable of a wider range of frequencies, this range is chosen as a good balance between resolution and tissue penetration, as higher frequencies yield higher resolution but lower tissue penetration.

1.3.3 Ultrasound Image Formation

Each ultrasound image is formed from radiofrequency information acquired from the sensor array in the form of A-lines. In order to form an A-line, the piezoelectric elements in the sensor array are pulsed in such a way to create a pressure beam in the area of interest. This pressure beam is swept through the tissue, using the resulting sound waves to form beamformed radiofrequency (RF) data as it goes. Then, the RF data is enveloped (the oscillations are removed, and the overall shape is extracted), which is turned into an A-line. The A-lines are then mathematically processed to form a B-Mode image usually by taking the log of the absolute value of the A-lines. A sample image is provided in Figure 1.3. While A-Lines are generally understood to be specifically the enveloped signal, for the purposes of this thesis, A-Lines refer to the beamformed RF signal pre-enveloping.

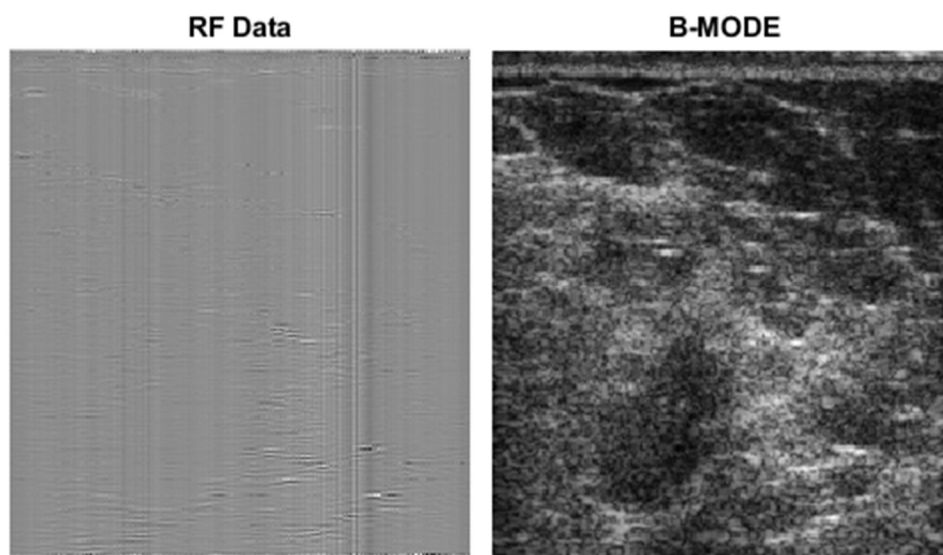


Figure 1.3 Sample RF data image acquired from a breast cancer case along with corresponding B-Mode ultrasound image .

1.4 In-Silico Ultrasound Image Generation

One of the techniques used in this thesis is the generation of fully in-silico ultrasound image generation for the purposes of generating bespoke data for validation.

The overall process to achieve this follows the same concepts described in Section 1.3 wherein the function of a transducer and the propagation of sound are simulated in silico. In general, there are 4 steps:

1. Simulate the scatterers present in tissues by specifying location and scattering coefficients.
2. Simulate the emission of pressure waves from the transducer.
3. Simulate the propagation of sound by solving the wave equation.
4. Calculate the received signal from the transducer.

The first step is easily done by randomizing the location of the desired number of scatterers in a field of view with a specified depth, width, and out-of-plane thickness. Each scatterer is given an amplitude or reflection coefficient. Next, the transducer emission is simulated based on the specified parameters. The exact details of the emission are not relevant for this thesis, but it should be noted that the computer simulator simulates the pressure propagation generated by the transducer. This pressure wave propagates through the tissues (Figure 1.4) before the returning pressure signal is calculated and recorded. This results in a set of radiofrequency signals that simulate what the transducer would see. The calculation of the returning signals however, has a significant limitation in its realism. Accurate calculation of the sound wave propagation is computationally highly demanding. As such, FIELD II approximates the signal as an incident sound wave that has only traveled through a homogenous medium. While this leads to good results overall, it is not capable of simulating the physics of artefacts that may be present in clinical examples (e.g acoustic shadowing). FIELD II was chosen because of a combination of computational efficiency and its presence in the existing literature, lending more credibility to its performance.

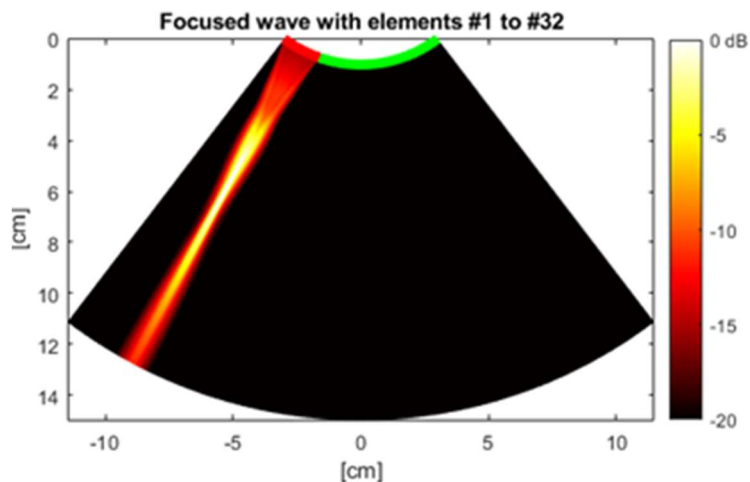


Figure 1.4 Sample pressure wave emission for a curvilinear probe. This process was performed with the open-source software FIELD II [59][60].

1.5 Time Delay Estimation

For elastography to be achieved, tissue displacements must be estimated to eventually calculate stiffness of the tissue. To do this, time delay estimation is used wherein the displacement of the tissue is related to the time delay difference in the radiofrequency data. This concept is illustrated in Figure 1.5 which is taken from [61].

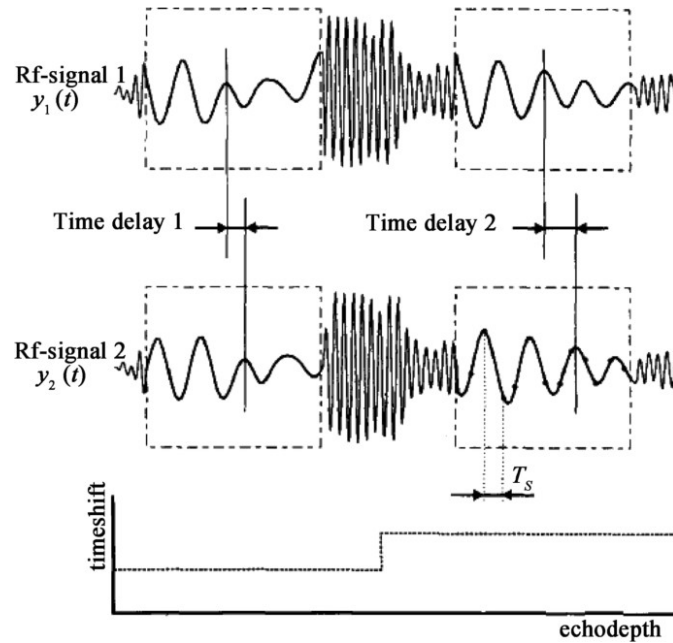


Figure 1.5 An illustration of time delay estimation on radiofrequency data taken from [61]. $y_1(t)$ and $y_2(t)$ are the RF – signals from the pre- and post-compression images that correspond to the same portion of the image. T_s represents the sampling time for the RF signal (which has been interpolated).

As can be seen in Figure 1.5, corresponding A-lines (y_1 and y_2) are compared based on a loss function to find the corresponding time delay between signals at every point along the A-line. This time delay can then be related to a depth measurement via the speed of sound (assumed to be 1540 m/s within tissue). The comparison can be done via many methods, but dynamic programming will be the basis of all further discussion in this thesis, where a loss function is evaluated recursively over the course of the A-line to determine displacements [52]. A primary issue with these methods is that they only yield integer displacements along the axial direction. More methodology must be employed to obtain sub-pixel axial displacements and lateral displacement estimates. In general, the displacement field should satisfy Equation (1.2) which maps the pre-compression image I_1 to the post-compression image I_2 where $\Delta a_{i,j}$ and $\Delta l_{i,j}$ are the axial and lateral displacement values of pixel (i,j) in the image.

$$I_1(i + \Delta a_{i,j}, j + \Delta l_{i,j}) - I_2(i, j) = 0 \quad 1.2$$

1.6 Theory of Elasticity

Before moving on to more sophisticated sub-pixel estimation techniques, the theory of elasticity must be discussed to motivate the methodology needed to improve the integer displacement techniques. In general, the theory of elasticity describes the way continuous materials deform under loading. The fundamental equation of interest to this thesis is Hooke's law, which relates stress—the internal force per unit area as given in Equation (1.3) which is used to calculate the normal stress in the x direction. The corresponding strain, which represents the deformation of the material normal to the x direction is given by Equation 4 as described by the spatial derivative of displacement in the material under question. The stress and strain are tensor quantities that have 9 components in the 3D space. These tensors are symmetric under small deformation, leading to 6 independent components. As such, Hooke's law, in its most general sense, is described by Equation (1.5) where ε represents the axial, lateral, and out-of-plane strains (ε_{xx} , ε_{yy} , and ε_{zz}), γ represents shear strains in different directions (γ_{xy} , γ_{yz} , γ_{xz}), σ represents the stress tensor, and the 6x6 matrix represents the stiffness matrix, which is a 6x6 matrix that describes the material's response to stresses in every direction where E is the Young's modulus and ν is the Poisson's Ratio of the material. Curly brackets indicate that the quantity is a vector. Figure 1.6 illustrates some of the modes of strain that can occur in any axis of the material.

$$\sigma_{xx} = \frac{F_x}{A_x} \quad 1.3$$

$$\varepsilon_{xx} = \frac{\partial u_x}{\partial x} \quad 1.4$$

$$\begin{Bmatrix} \varepsilon_{xx} \\ \varepsilon_{yy} \\ \varepsilon_{zz} \\ \gamma_{xy} \\ \gamma_{yz} \\ \gamma_{xz} \end{Bmatrix} = \begin{bmatrix} 1 & -\nu & -\nu & 0 & 0 & 0 \\ -\nu & 1 & -\nu & 0 & 0 & 0 \\ -\nu & -\nu & 1 & 0 & 0 & 0 \\ 0 & 0 & 0 & 2 + 2\nu & 0 & 0 \\ 0 & 0 & 0 & 0 & 2 + 2\nu & 0 \\ 0 & 0 & 0 & 0 & 0 & 2 + 2\nu \end{bmatrix} \begin{Bmatrix} \sigma_{xx} \\ \sigma_{yy} \\ \sigma_{zz} \\ \sigma_{xy} \\ \sigma_{yz} \\ \sigma_{xz} \end{Bmatrix} \quad 1.5$$

However, given that ultrasound elastography is a 2D modality, using the 3D form of Hooke's law is unnecessary, and we can collapse the problem into two dimensions. Moreover, we may assume that the tissues under study are isotropic. Under these two conditions, we have 2 major ways of collapsing Hooke's law into two dimensions—plane stress and plane strain—where it is assumed that either the out of plane stress or strain is 0, respectively depending on which is more appropriate given the desired simulation. More generally, Hooke's law can be expressed as a 2D problem using any assumption about the out of plane stress or strain, but the most popular are setting each to 0. Nonetheless, the plane stress and plane strain versions of the Hooke's law are shown in Equations (1.6) and (1.7).

$$\begin{Bmatrix} \varepsilon_{xx} \\ \varepsilon_{yy} \\ \gamma_{xy} \end{Bmatrix} = \frac{1}{E} * \begin{bmatrix} 1 & -\nu & 0 \\ -\nu & 1 & 0 \\ 0 & 0 & 2 + 2\nu \end{bmatrix} \begin{Bmatrix} \sigma_{xx} \\ \sigma_{yy} \\ \sigma_{xy} \end{Bmatrix} \quad 1.6$$

$$\begin{Bmatrix} \varepsilon_{xx} \\ \varepsilon_{yy} \\ \gamma_{xy} \end{Bmatrix} = \frac{1 + \nu}{E} * \begin{bmatrix} 1 - \nu & -\nu & 0 \\ -\nu & 1 - \nu & 0 \\ 0 & 0 & 2 \end{bmatrix} \begin{Bmatrix} \sigma_{xx} \\ \sigma_{yy} \\ \sigma_{xy} \end{Bmatrix} \quad 1.7$$

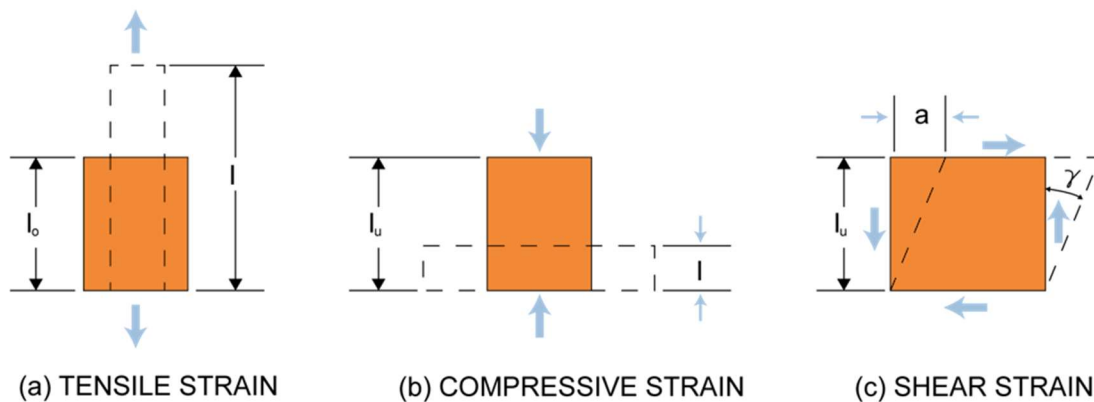


Figure 1.6 An illustration of the mechanical stresses described in Hooke's law illustrating the different modes of stress and strain that can occur in each direction. Note that shearing can occur in any combination of directions as well. This figure was taken from <https://dewesoft.com/blog/measure-strain-and-pressure>.

1.7 Regularization

1.7.1 Mathematical Regularization

The first way to improve the displacement estimate given by dynamic programming is by applying some regularization metrics. These essentially attempt to enforce certain properties upon the displacement field to make it more reasonable, including smoothness. The first method to be proposed to this end is analytic minimization in 2D, also known as AM2D [49]. In this method, the displacements are enhanced by the following cost function:

$$\begin{aligned}
 C_j(\Delta a_i, \dots, \Delta a_m, \Delta l_1 \dots \Delta l_i) \\
 &= \sum_{i=1}^m \left\{ [I_1(i, j) - I_2(i + a_i + \Delta a_i, j + l_i + \Delta l_i)]^2 \right. \\
 &\quad + \alpha (a_i + \Delta a_i - a_{i-1} - \Delta a_{i-1})^2 + \beta_a (l_i + \Delta l_i - l_{i-1} - \Delta l_{i-1})^2 \\
 &\quad \left. + \beta_l (l_i - \Delta l_i - l_{i,j-1})^2 \right\}
 \end{aligned} \tag{1.8}$$

Where I_1, I_2 are the RF images acquired pre- and post- compression, a_i and l_i are the i^{th} axial and lateral initial displacement estimate for an A-Line in question, Δa_i and Δl_i represent the subpixel displacement components in the axial and lateral directions, respectively. α , β_a and β_l are all regularization coefficients for the displacement field. This cost function essentially has two components. The first is the $[I_1(i, j) - I_2(i + a_i + \Delta a_i, j + l_i + \Delta l_i)]^2$ term which ensures that the displacement does not deviate too much such that the integrity of the displacement is destroyed. The other terms in the cost function ensures that the displacements between adjacent pixels does not change too much in the axial and lateral directions. This acts as a de-noising procedure and allows for smoother images. Equation (1.8) is then formed for each A-line, leading to a linear system of equations before it is solved for Δa_i and Δl_i values.

The next version of this method is called global ultrasound elastography (GLUE) which applies a similar cost function, but to the whole image simultaneously [51]. This

further increases the quality of the displacement image in both the axial and lateral directions. There are many other methods for improving the axial and lateral displacement estimates, such as window-based approaches and second order smoothing, but those will be discussed in later chapters [52, 53, 63, 64].

1.7.2 Tissue-Mechanics Based Regularization

One of the limitations to the mathematical regularization methods is that they rely entirely on mathematical constraints on the displacement field without incorporating other known information about the behaviour of the tissue under study. This can lead to limited improvement of the displacement or a very high computational requirement while complex constraints are applied to the data. An effective way to circumvent these limitations is to use what is known about the intrinsic behavior of biological tissues. For instance, human soft tissues are known to be near-incompressible, and we know that the tissue must keep its integrity and remain free of tears throughout the compression process. From these two facts, the strain refinement algorithm (STREAL) was developed [65]. This algorithm uses both incompressibility and compatibility to improve the estimate of displacement and strain. Both incompressibility and compatibility equations are shown in Equations (1.9) through (1.15). Note that incompressibility can simply be written as the divergence of the vector field U which describes the 3D displacement of the tissue.

$$\nabla \cdot U = \frac{\partial u_x}{\partial x} + \frac{\partial u_y}{\partial y} + \frac{\partial u_z}{\partial z} = 0 \quad 1.9$$

$$\frac{\partial^2 \varepsilon_x}{\partial y \partial z} = \frac{\partial^3 u_x}{\partial x \partial y \partial z} \quad 1.10$$

$$\frac{\partial^2 \varepsilon_y}{\partial x \partial z} = \frac{\partial^3 u_y}{\partial x \partial y \partial z} \quad 1.11$$

$$\frac{\partial^2 \varepsilon_z}{\partial x \partial y} = \frac{\partial^3 u_z}{\partial x \partial y \partial z} \quad 1.12$$

$$\frac{\partial \gamma_{xy}}{\partial z} = \frac{\partial^2 u_x}{\partial x \partial y} + \frac{\partial^2 u_y}{\partial x \partial z} \quad 1.13$$

$$\frac{\partial \gamma_{yz}}{\partial x} = \frac{\partial^2 u_y}{\partial x \partial z} + \frac{\partial^2 u_z}{\partial x \partial y} \quad 1.14$$

$$\frac{\partial \gamma_{xz}}{\partial y} = \frac{\partial^2 u_x}{\partial y \partial z} + \frac{\partial^2 u_z}{\partial x \partial y} \quad 1.15$$

The issue with these equations is that they require an assumption or *a priori* knowledge about the behaviour of the tissue in 3D, in order to be used with 2D QUSE modality. To address this issue, one can simply assume plane strain and ignore the impact of the third dimension, in which case all strain component in the z direction are 0. Furthermore, analytic assumptions can be made about the tissue and its geometry (e.g. idealizing it as a semi-infinite medium [66]). These methods can be very powerful as they are well motivated by underlying knowledge about the tissue, but require an understanding of the tissue behaviour, which may or may not be entirely known.

1.8 Iterative Reconstruction

The final step to elastography is to use the finite element method to reconstruct the stiffness or the Young's modulus of the tissue. The fundamental method behind this is to construct a finite element simulation based on measured displacements from the displacement estimator. This can be performed through starting with an initial guess for the Young's modulus distribution. Having this distribution facilitates conducting finite element analysis to calculate stresses. The strains calculated using the measured tissue displacements are used via Hooke's law to update the estimation of the Young's modulus image. This calculation process is repeated until the changes in the calculated Young's moduli are negligible.

1.8.1 The Finite-Element Method

One of the major techniques in engineering is called the finite element method (FEM) which was developed to provide approximate solutions to partial differential equations, including equations governing solid mechanics. This method is used to estimate the response to mechanical stimulation on arbitrary geometry, including internal stresses, allowing engineers to design arbitrary parts and shapes for any given application. It involves the decomposition of a continuous geometry of the object of interest into finite elements with specific geometry which are made up of nodes within the object's geometry. From there, stiffness matrices are formed for each element, which are then assembled into a global stiffness matrix. Once that is assembled, boundary conditions are imposed, and the following equation (1.16) is solved [67].

$$F = KU \quad 1.16$$

Where F is the force vector, describing external forces on the geometry, K in this case is the global stiffness matrix, and U is the displacement vector of the nodes. From these vectors, element stresses and strains can be calculated. In other engineering applications, this can be used to determine if a given design can withstand certain prescribed load conditions.

In USE, a finite element analysis can be formulated to mimic the compression of the tissues. First, a grid is created and populated with elements. Then, stiffness is assigned to each element based on current estimate of the Young's modulus distribution before the global stiffness matrix is assembled. Then, displacements from the border of the displacement field are taken from the estimation algorithm and are imposed as prescribed displacement boundary conditions in the finite element simulation. The displacements for the rest of the image are calculated, and the strain values for each element are calculated.

1.8.2 Iterative Reconstruction of the Young's Modulus

Solving for the Young's modulus from the displacement and strains acquired from the displacement estimators is called an inverse problem, whereas applying the actual

mechanical stimulation is the “forward” problem. One method to solve inverse problems is by iteratively converging on the solution through successive calculations. In the case of Young’s modulus reconstruction, Hooke’s law can be used to re-calculate the Young’s modulus before updating the finite-element model. Figure 1.7 shows a flow chart of the iterative reconstruction while the full method is described in [58]. This methodology is also known as a full-inversion reconstruction, because it takes into account the tissue actual nonuniform stress distribution and fully solves the inverse problem, rather than applying approximations.

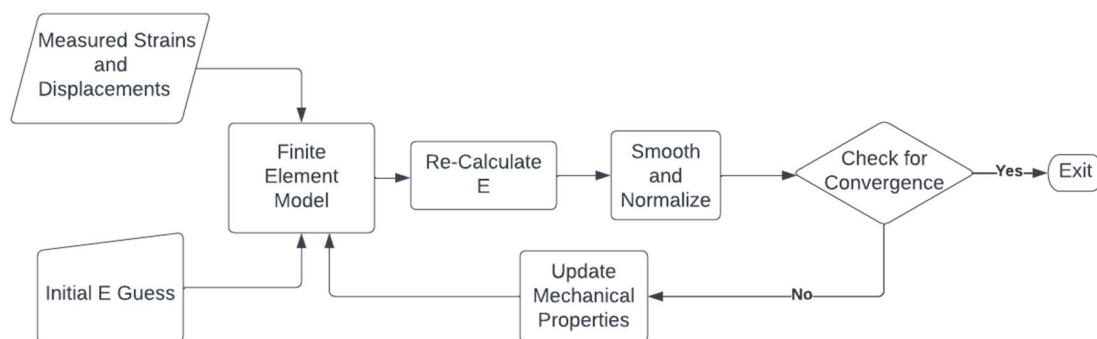


Figure 1.7 An overview of the iterative reconstruction algorithm used to calculate the Young’s modulus of the tissue being studied. This is an iterative technique whereby the Young’s modulus is calculated by repeatedly simulating the stress field and recalculating the E field using Hooke’s law until convergence is achieved.

First, an initial guess of the Young’s modulus (E) is made before setting up the finite element model, using measured displacements. The finite element analysis is performed, and from the calculated stresses and measured strains, E is calculated, smoothed, and normalized and then convergence is checked based on the difference between the current and previous iterations. If the difference is less than a tolerance, the reconstruction is complete, otherwise the model is updated and recalculated.

1.9 Overview of Current Issues

One of the greatest problems in the usage and development of QUSE is the problem of data quality. This is caused by the freehand nature of the procedure, which results in inconsistencies of the ultrasound probe orientation between the pre- and post-compression frames, resulting in poor image quality due to out-of-plane motion and inconsistent pressure application. In the case where good data are available, elastography produces good quality images with no extra hardware, which makes it a very attractive imaging modality.

Unfortunately, there is no way to efficiently assess data quality automatically which means that data assessment needs to be done manually, making the technique clinically unfeasible. There are, however, three methods to deal with this problem, the latter two of those mentioned are explored in this thesis. The first method is to improve the protocol by which elastography is performed such that data quality is guaranteed. This can occur by way of training or through using an additional hardware device employed for force application. Unfortunately, both ways of improving the protocol decrease the clinical convenience of the method, which makes them unattractive as much of the value of QUSE is in its convenience. The second method addresses the issue by allowing for convenient manual assessment of data by optimizing the methodology to real-time rates, which allows clinicians to actively search for high-quality images and discarding the rest. The final method involves developing an automatic method by which data quality can be analyzed *en masse*, replacing manual assessment. This would allow a compression “video” to be taken and analyzing all options in the video for suitability for elastography.

Moreover, one other issue with the lack of data quality is hampering the development of new displacement estimation algorithms. Without a well-founded method of data quality control, it can be very difficult, if not impossible to determine whether the algorithm has failed due to a fundamental flaw in the methodology or the lack of data quality, especially when dealing with clinical data.

These issues with elastography have contributed to the formation of the research objectives this thesis sets out to achieve, which are outlined in the next section.

1.10 Research Objectives

This thesis has the overarching objective to advance the tools available to implement ultrasound elastography, moving towards a new generation of real-time ultrasound elastography systems. More specifically, there are four major objectives:

1. Categorization and comparison of existing displacement estimation algorithms at the full-inversion stiffness reconstruction level.
2. Developing a new in-silico method to generate more realistic data.
3. Developing a method to assess the quality of the underlying radiofrequency pair acquired for elastography to determine the suitability of the displacement estimate.

1.11 Thesis Outline

This work is presented in a total of 5 chapters, the current one being the introduction, followed by 3 chapters addressing the objectives outlined in the previous section. Then, a conclusion and discussion chapter will be provided.

1.11.1 Chapter 2: Categorization and Comparison of Displacement Estimators at the Full Stiffness Reconstruction Level

One major gap in the current literature is the lack of comparison and analysis of displacement estimators at the full stiffness reconstruction level rather than just at the strain level where the latter provides a crude estimate of the stiffness distribution. This has led to the development of increasingly complex and sophisticated displacement estimators that may or may not lead to better stiffness reconstruction results. Ultimately, the metric which is being measured is the change in stiffness of the lesion. The chief concern with the more sophisticated algorithms is the concern for over-smoothing, leading to a loss of potentially clinically relevant details in the image. Moreover, an assessment of computational complexity versus image quality needs to be done if the technique is to be implemented in a real-time system. The results show that the simpler and older algorithms have a high

quality to complexity ratio, and are recommended in a real-time system, with more sophisticated algorithms reserved for post-acquisition analysis.

1.11.2 Chapter 3: Elastosynth - An Open-Source software package for the generation of realistic in-silico data for ultrasound elastography

This chapter showcases a new software package that allows for the generation of more realistic synthetic ultrasound elastography data, and addressing the limitations associated with current synthetic techniques. Namely there are two major concerns: realism and runtime. Current techniques are limited to homogenous phantoms which do not reflect the reality of clinical scenarios where the tissue is known to be highly heterogeneous. Moreover, current techniques require hours upon hours for the simulation of a single ultrasound acquisition, which makes it impossible to generate massive datasets necessary for interesting applications involving machine learning. In this chapter, I introduce a new method by which heterogeneity can be automatically generated. Moreover, a bespoke finite element solver is described which is designed for the express purpose of handling highly heterogeneous simulations. Finally, the ultrasound simulation process was optimized by ensuring that the only scatterers used in the simulation are the ones likely to contribute to the resulting signal.

1.11.3 Chapter 4: A Method to Quantitatively Assess the Quality of Displacement Estimations

As discussed in Chapter 3 and in Section 1.9, one way of addressing the data quality issue is to allow for automatic assessment of radiofrequency data after acquiring a compression video. This chapter presents a methodology-agnostic way to objectively assess the quality of a displacement estimate automatically before triaging truly bad frame-pairs from ones that could potentially be good. The method we propose uses the displacement estimate to warp the pre-compression radiofrequency image to approximate the post-compression image, and then using correlation and mean squared error to compare the estimated post-compression image to the actual post-compression image. The hypothesis is that given a very high-quality displacement estimate and good data, the correspondence between the

warped pre-compression image and the real post-compression image is near perfect, namely their correlation is above 0.9 and mean-squared errors is less than 0.5.

1.11.4 Chapter 5: Discussion and Conclusions

This chapter summarizes all that was discussed in previous chapters, proposes future work, and concludes this dissertation.

1.12 References

- [1] “Breast cancer statistics, Canadian Cancer Society,” 2016.
<https://cancer.ca/en/cancer-information/cancer-types/breast/statistics> (accessed Jan. 19, 2022).
- [2] M. Arnold *et al.*, “Current and future burden of breast cancer: Global statistics for 2020 and 2040,” *The Breast*, vol. 66, pp. 15–23, 2022, doi: 10.1016/j.breast.2022.08.010.
- [3] F. Guo, Y. fang Kuo, Y. C. T. Shih, S. H. Giordano, and A. B. Berenson, “Trends in breast cancer mortality by stage at diagnosis among young women in the United States,” *Cancer*, vol. 124, no. 17, pp. 3500–3509, Sep. 2018, doi: 10.1002/CNCR.31638.
- [4] M. K. Shetty, “Breast cancer screening and diagnosis: A synopsis,” *Breast Cancer Screening and Diagnosis: A Synopsis*, pp. 1–458, Jan. 2015, doi: 10.1007/978-1-4939-1267-4/COVER.
- [5] “Ontario Breast Screening Program – Cancer Care Ontario.”
<https://www.cancercareontario.ca/en/cancer-care-ontario/programs/screening-programs/ontario-breast-obsp> (accessed Sep. 05, 2023).
- [6] Y. Gao, B. Reig, L. Heacock, D. L. Bennett, S. L. Heller, and L. Moy, “Magnetic Resonance Imaging in Screening of Breast Cancer,” *Radiol Clin North Am*, vol. 59, no. 1, p. 85, Jan. 2021, doi: 10.1016/J.RCL.2020.09.004.

- [7] S. J. Lord *et al.*, “A systematic review of the effectiveness of magnetic resonance imaging (MRI) as an addition to mammography and ultrasound in screening young women at high risk of breast cancer,” *Eur J Cancer*, vol. 43, no. 13, pp. 1905–1917, Sep. 2007, doi: 10.1016/J.EJCA.2007.06.007.
- [8] D. Thigpen, A. Kappler, and R. Brem, “diagnostics The Role of Ultrasound in Screening Dense Breasts-A Review of the Literature and Practical Solutions for Implementation,” *Diagnostics (Basel, Switzerland)* vol. 8,1 20. 16 Mar. 2018, doi: 10.3390/diagnostics8010020.
- [9] R. F. Brem, M. J. Lenihan, J. Lieberman, and J. Torrente, “Screening breast ultrasound: Past, present, and future,” *American Journal of Roentgenology*, vol. 204, no. 2, pp. 234–240, Feb. 2015, doi: 10.2214/AJR.13.12072/ASSET/IMAGES/LARGE/02_13_12072_02D.JPEG.
- [10] F. X. Bosch, J. Ribes, M. Díaz, and R. Cléries, “Primary liver cancer: Worldwide incidence and trends,” *Gastroenterology*, vol. 127, no. 5, pp. S5–S16, Nov. 2004, doi: 10.1053/J.GASTRO.2004.09.011.
- [11] C. T. Frenette, A. J. Isaacson, I. Bargellini, S. Saab, and A. G. Singal, “A Practical Guideline for Hepatocellular Carcinoma Screening in Patients at Risk”, *Mayo Clinic proceedings. Innovations, quality & outcomes* vol. 3,3 302-310. 11 Jul. 2019, doi: 10.1016/j.mayocpiqo.2019.04.005.
- [12] C. W. Molter, E. F. Muszynski, Y. Tao, T. Trivedi, A. Clouvel, and A. J. Ehrlicher, “Prostate cancer cells of increasing metastatic potential exhibit diverse contractile forces, cell stiffness, and motility in a microenvironment stiffness-dependent manner,” *Front Cell Dev Biol*, vol. 10, p. 932510, Sep. 2022, doi: 10.3389/FCELL.2022.932510/BIBTEX.
- [13] X. Wang *et al.*, “Alterations in mechanical properties are associated with prostate cancer progression,” *Medical Oncology*, vol. 31, no. 3, pp. 1–10, Mar. 2014, doi: 10.1007/S12032-014-0876-9/FIGURES/5.

- [14] S. Molla, D. R. Katti, and K. S. Katti, “Mechanobiological evaluation of prostate cancer metastasis to bone using an in vitro prostate cancer testbed”, *J Biomech.* Jan. 2021, doi: 10.1016/j.jbiomech.2020.110142.
- [15] K. Hoyt *et al.*, “Tissue elasticity properties as biomarkers for prostate cancer,” *Cancer Biomark*, vol. 4, no. 4–5, p. 213, 2008, doi: 10.3233/CBM-2008-44-505.
- [16] Z. Liu *et al.*, “Heterogeneous Responses to Mechanical Force of Prostate Cancer Cells Inducing Different Metastasis Patterns,” *Advanced Science*, vol. 7, no. 15, Aug. 2020, doi: 10.1002/ADVS.201903583.
- [17] G. S. van Tienderen *et al.*, “Tumor decellularization reveals proteomic and mechanical characteristics of the extracellular matrix of primary liver cancer,” 2023, doi: 10.1016/j.bioadv.2023.213289.
- [18] Y. Kim, J. W. Hong, J. Kim, and J. H. Shin, “Comparative study on the differential mechanical properties of human liver cancer and normal cells,” *Biomaterials advances* vol. 146 (2023): <http://dx.doi.org/10.1080/19768354.2013.789452>,
- [19] F. Ti, X. Chen, H. Yang, S. Liu, and T. J. Lu, “A theory of mechanobiological sensation: strain amplification/attenuation of coated liquid inclusion with surface tension,” *Acta Mechanica Sinica/Lixue Xuebao*, vol. 37, no. 1, pp. 145–155, Jan. 2021, doi: 10.1007/S10409-020-01017-3.
- [20] G. Zhang, M. Long, Z. Z. Wu, and W. Q. Yu, “Mechanical properties of hepatocellular carcinoma cells,” *World J Gastroenterol*, vol. 8, no. 2, pp. 243–246, 2002, doi: 10.3748/WJG.V8.I2.243.
- [21] W. Pei *et al.*, “Regional biomechanical imaging of liver cancer cells,” *J Cancer*, vol. 10, no. 19, p. 4481, 2019, doi: 10.7150/JCA.32985.
- [22] A. Mohammadalipour, F. Benencia, M. M. Burdick, and D. F. Tees, “Abstract 3766: Mechanical properties of cancer cells: A possible biomarker for stemness.”

Cancer Research, vol. 73, no. 8_Supplement, pp. 3766–3766, Apr. 2013.

doi:10.1158/1538-7445.am2013-3766

[23] J. E. Kim, D. S. Reynolds, M. H. Zaman, and M. Mak, “Characterization of the mechanical properties of cancer cells in 3D matrices in response to collagen concentration and cytoskeletal inhibitors,” *Integrative Biology*, vol. 10, no. 4, pp. 232–241, Apr. 2018, doi: 10.1039/C8IB00044A.

[24] Marina. L. Yubero *et al.*, “Effects of energy metabolism on the mechanical properties of breast cancer cells,” *Communications Biology*, vol. 3, no. 1, Oct. 2020.

doi:10.1038/s42003-020-01330-4

[25] W. Yu *et al.*, “Cancer cell mechanobiology: a new frontier for cancer research,” *Journal of the National Cancer Center*, vol. 2, no. 1, pp. 10–17, Mar. 2022, doi:

10.1016/J.JNCC.2021.11.007.

[26] H. Kim, K. Ishibashi, T. Okada, and C. Nakamura, “Supplementary Materials: Mechanical Property Changes in Breast Cancer Cells Induced by Stimulation with Macrophage Secretions in Vitro”, Accessed: Sep. 06, 2023. [Online]. Available: www.mdpi.com/journal/micromachines

[27] G. Runel, N. Lopez-Ramirez, J. Chlasta, and I. Masse, “cells Biomechanical Properties of Cancer Cells,” 2021, doi: 10.3390/cells10040887.

[28] M. S. Nikoli, G. Scarcelli, and K. Tanner, “Multimodal microscale mechanical mapping of cancer cells in complex microenvironments”, doi: 10.1016/j.bpj.2022.09.002.

[29] T. Fuhs *et al.*, “Rigid tumours contain soft cancer cells,” *Nature Physics* 2022 18:12, vol. 18, no. 12, pp. 1510–1519, Sep. 2022, doi: 10.1038/s41567-022-01755-0.

[30] P. Katira, M. H. Zaman, and R. T. Bonnecaze, “How Changes in Cell Mechanical Properties Induce Cancerous Behavior,” 2012, doi: 10.1103/PhysRevLett.108.028103.

- [31] I. Kang, D. Panneerselvam, V. P. Panoskaltsis, S. J. Eppell, R. E. Marchant, and C. M. Doerschuk, “Changes in the Hyperelastic Properties of Endothelial Cells Induced by Tumor Necrosis Factor- α ,” *Biophys J*, vol. 94, pp. 3273–3285, doi: 10.1529/biophysj.106.099333.
- [32] A. Samani, J. Zubovits, and D. Plewes, “Elastic moduli of normal and pathological human breast tissues: An inversion-technique-based investigation of 169 samples,” *Phys Med Biol*, vol. 52, no. 6, pp. 1565–1576, Mar. 2007, doi: 10.1088/0031-9155/52/6/002.
- [33] S. C. H. Dempsey, J. J. O’Hagan, and A. Samani, “Measurement of the hyperelastic properties of 72 normal homogeneous and heterogeneous ex vivo breast tissue samples,” *J Mech Behav Biomed Mater*, vol. 124, p. 104794, Dec. 2021, doi: 10.1016/J.JMBBM.2021.104794.
- [34] * A Manduca *et al.*, “Magnetic resonance elastography: Non-invasive mapping of tissue elasticity,” *Med Image Anal*, vol. 5, pp. 237–254, 2001, Accessed: Aug. 30, 2023. [Online]. Available: www.elsevier.com/locate/media
- [35] S. A. Kruse *et al.*, “Magnetic resonance elastography of the brain,” *NeuroImage*, vol. 39, no. 1, pp. 231–237, Jan. 2008. doi:10.1016/j.neuroimage.2007.08.030
- [36] [1] G. Low, “General Review of Magnetic resonance elastography,” *World Journal of Radiology*, vol. 8, no. 1, p. 59, 2016. doi:10.4329/wjr.v8.i1.59
- [37] S. K. Venkatesh, M. Yin, and R. L. Ehman, “Magnetic resonance elastography of liver: Technique, analysis, and clinical applications,” *Journal of Magnetic Resonance Imaging*, vol. 37, no. 3, pp. 544–555, Mar. 2013, doi: 10.1002/JMRI.23731.
- [38] Y. K. Mariappan, K. J. Glaser, and R. L. Ehman, “Magnetic resonance elastography: A Review,” *Clinical Anatomy*, vol. 23, no. 5, pp. 497–511, Jun. 2010. doi:10.1002/ca.21006

- [39] T. A. Krouskop, T. M. Wheeler, F. Kallel, B. S. Garra, and T. Hall, “Elastic moduli of breast and prostate tissues under compression,” *Ultrason Imaging*, vol. 20, no. 4, pp. 260–274, 1998, doi: 10.1177/016173469802000403.
- [40] R. Righetti, M. Righetti, J. Ophir, and T. A. Krouskop, “The feasibility of estimating and imaging the mechanical behavior of poroelastic materials using axial strain elastography,” *Phys Med Biol*, vol. 52, no. 11, p. 3241, May 2007, doi: 10.1088/0031-9155/52/11/020.
- [41] C. Papadacci, E. A. Bunting, and E. E. Konofagou, “3D Quasi-Static Ultrasound Elastography With Plane Wave In Vivo,” *IEEE Trans Med Imaging*, vol. 36, no. 2, p. 357, 2017, doi: 10.1109/TMI.2016.2596706.
- [42] J. Jiang and B. Peng, “A Comparative Study of Displacement De-Noising Strategies: An in Vivo Feasibility Study Using 3D Whole Breast Ultrasound Data,” in *2018 IEEE International Ultrasonics Symposium (IUS)*, IEEE, 2018. Accessed: Aug. 23, 2022. [Online]. Available: <https://ieeexplore.ieee.org/document/8579998/>
- [43] T. Varghese, “Quasi-static ultrasound elastography,” *Ultrasound Clinics*, vol. 4, no. 3, pp. 323–338, Jul. 2009. doi:10.1016/j.cult.2009.10.009
- [44] J. L. Gennisson, T. Deffieux, M. Fink, and M. Tanter, “Ultrasound elastography: Principles and techniques,” *Diagn Interv Imaging*, vol. 94, no. 5, pp. 487–495, May 2013, doi: 10.1016/J.DIII.2013.01.022.
- [45] R. M. S. Sigrist, J. Liau, A. El Kaffas, M. C. Chammas, and J. K. Willmann, “Ultrasound Elastography: Review of Techniques and Clinical Applications,” *Theranostics*, vol. 7, no. 5, pp. 1303–1329, 2017, doi: 10.7150/THNO.18650.
- [46] M. S. Taljanovic *et al.*, “Shear-Wave Elastography: Basic Physics and Musculoskeletal Applications,” <https://doi.org/10.1148/rg.2017160116>, vol. 37, no. 3, pp. 855–870, May 2017, doi: 10.1148/RG.2017160116.

- [47] N. H. Afdhal, "Fibroscan (Transient Elastography) for the Measurement of Liver Fibrosis," *Gastroenterol Hepatol (N Y)*, vol. 8, no. 9, p. 605, Sep. 2012, Accessed: Aug. 02, 2023. [Online]. Available: [/pmc/articles/PMC3594956/](https://pubmed.ncbi.nlm.nih.gov/3594956/)
- [48] A. M. Osman, A. El Shimy, and M. M. Abd El Aziz, "2D shear wave elastography (SWE) performance versus vibration-controlled transient elastography (VCTE/fibroscan) in the assessment of liver stiffness in chronic hepatitis," *Insights into Imaging*, vol. 11, no. 1, Mar. 2020. doi:10.1186/s13244-020-0839-y
- [49] H. Rivaz, E. Boctor, P. Foroughi, R. Zellars, G. Fichtinger, and G. Hager, "Ultrasound Elastography: A Dynamic Programming Approach," *IEEE Trans Med Imaging*, vol. 27, no. 10, pp. 1373–1377, Oct. 2008, doi: 10.1109/TMI.2008.917243.
- [50] J. Luo and E. Konofagou, "A fast normalized cross-correlation calculation method for motion estimation," *IEEE Trans Ultrason Ferroelectr Freq Control*, vol. 57, no. 6, pp. 1347–1357, 2010, doi: 10.1109/TUFFC.2010.1554.
- [51] H. S. Hashemi and H. Rivaz, "Global Time-Delay Estimation in Ultrasound Elastography," *IEEE Trans Ultrason Ferroelectr Freq Control*, vol. 64, no. 10, pp. 1625–1636, Oct. 2017, doi: 10.1109/TUFFC.2017.2717933.
- [52] M. Ashikuzzaman and H. Rivaz, "Second-Order Ultrasound Elastography With L1-Norm Spatial Regularization," *IEEE Trans Ultrason Ferroelectr Freq Control*, vol. 69, no. 3, 2022, Accessed: Aug. 23, 2022. [Online]. Available: <https://ieeexplore.ieee.org/document/9674909/>
- [53] M. Mirzaei, A. Asif, and H. Rivaz, "Combining Total Variation Regularization with Window-Based Time Delay Estimation in Ultrasound Elastography," *IEEE Trans Med Imaging*, vol. 38, no. 12, pp. 2744–2754, Dec. 2019, doi: 10.1109/TMI.2019.2913194.
- [54] N. Kheirkhah, A. Sadeghi-Naini, and A. Samani, "Analytical Estimation of Out-of-plane Strain in Ultrasound Elastography to Improve Axial and Lateral Displacement

Fields,” *Proceedings of the Annual International Conference of the IEEE Engineering in Medicine and Biology Society, EMBS*, vol. 2020-July, pp. 2055–2058, Jul. 2020, doi: 10.1109/EMBC44109.2020.9176086.

[55] A. Samani, J. Bishop, and D. B. Plewes, “A constrained modulus reconstruction technique for breast cancer assessment,” *IEEE Trans Med Imaging*, vol. 20, no. 9, pp. 877–885, Sep. 2001, doi: 10.1109/42.952726.

[56] “Ultrasound Physics and Technical Facts for the Beginner | Sonoguide.” <https://www.acep.org/sonoguide/basic/ultrasound-physics-and-technical-facts-for-the-beginner> (accessed Sep. 06, 2023).

[57] A. Manbachi and R. S. C. Cobbold, “Development and application of piezoelectric materials for ultrasound generation and detection,” *Ultrasound*, vol. 19, no. 4, pp. 187–196, Nov. 2011, doi: 10.1258/ULT.2011.011027/ASSET/IMAGES/LARGE/10.1258_UL.2011.011027-FIG14.JPEG.

[58] A. Carovac, F. Smajlovic, and D. Junuzovic, “Application of Ultrasound in Medicine,” *Acta Informatica Medica*, vol. 19, no. 3, p. 168, 2011, doi: 10.5455/AIM.2011.19.168-171

[59] J. A. Jensen, “FIELD: A program for simulating ultrasound systems,” *Med. Biol. Eng. Comput.*, vol. 34, no. SUPPL. 1, pp. 351–352, 1996, Accessed: Sep. 14, 2023.

[Online]. Available: <https://orbit.dtu.dk/en/publications/field-a-program-for-simulating-ultrasound-systems>

[60] J. A. Jensen and N. B. Svendsen, “Calculation of Pressure Fields from Arbitrarily Shaped, Apodized, and Excited Ultrasound Transducers,” *IEEE Trans. Ultrason. Ferroelectr. Freq. Control*, vol. 39, no. 2, pp. 262–267, 1992, doi: 10.1109/58.139123.

[61] H. an Li, M. Zhang, K. Yu, X. Qi, and J. Tong, “A Displacement Estimated Method for Real Time Tissue Ultrasound Elastography,” *Mobile Networks and*

Applications, vol. 26, no. 5, pp. 2014–2023, Oct. 2021, doi: 10.1007/S11036-021-01735-3/TABLES/2.

[62] H. Rivaz, E. M. Boctor, M. A. Choti, and G. D. Hager, “Real-time regularized ultrasound elastography,” *IEEE Transactions on Medical Imaging*, vol. 30, no. 4, pp. 928–945, Apr. 2011. doi:10.1109/tmi.2010.2091966

[63] A. Zayed, S. Member, H. Rivaz, and S. Member, “Fast Strain Estimation and Frame Selection in Ultrasound Elastography Using Machine Learning,” *IEEE Trans Ultrason Ferroelectr Freq Control*, vol. 68, no. 3, 2021, doi: 10.1109/TUFFC.2020.2994028.

[64] M. Ashikuzzaman, G. Student Member, T. J. Hall, H. Rivaz, and S. Member, “Incorporating Gradient Similarity for Robust Time Delay Estimation in Ultrasound Elastography,” *IEEE Trans Ultrason Ferroelectr Freq Control*, vol. 69, no. 5, 2022, doi: 10.1109/TUFFC.2022.3164287.

[65] N. Kheirkhah, S. C. H. Dempsey, H. Rivaz, A. Samani, and A. Sadeghi-Naini, “A Tissue Mechanics Based Method to Improve Tissue Displacement Estimation in Ultrasound Elastography,” *Proceedings of the Annual International Conference of the IEEE Engineering in Medicine and Biology Society, EMBS*, vol. 2020-July, pp. 2051–2054, Jul. 2020, doi: 10.1109/EMBC44109.2020.9175869.

[66] N. Kheirkhah, A. Sadeghi-Naini, and A. Samani, “Analytical Estimation of Out-of-plane Strain in Ultrasound Elastography to Improve Axial and Lateral Displacement Fields,” *Proc. Annu. Int. Conf. IEEE Eng. Med. Biol. Soc. EMBS*, vol. 2020-July, pp. 2055–2058, Jul. 2020, doi: 10.1109/EMBC44109.2020.9176086.

[67] R. D. (Robert D. Cook, “Finite element modeling for stress analysis,” p. 320, 1995, Accessed: Mar. 04, 2024. [Online]. Available: <https://www.wiley.com/en-us/Finite+Element+Modeling+for+Stress+Analysis-p-9780471107743>

Chapter 2

2 Comparative Study of Ultrasound Tissue Motion Tracking Techniques for Effective Breast Ultrasound Elastography

A variant of this chapter has been published in journal of Applied Science 2023, 13(21), 11912; <https://doi.org/10.3390/app132111912> under the creative commons license.*

2.1 Introduction

To design a real-time imaging system for ultrasound elastography, an assessment needs to be done as to which displacement estimator should be used. Unfortunately, most displacement estimators currently do not run at real-time rates. Therefore, an assessment needs to be done to determine if the currently available real-time methods are of sufficient quality, or whether work needs to be put into optimizing the higher quality estimators. Moreover, due to the development of a real-time optimization of a tissue mechanics-based strain enhancement algorithm (STREAL), each studied motion estimator should be revisited with and without STREAL, as it may provide the needed boost to quality with very low computational requirement.

Moreover, the strain images are not as good as the underlying stiffness distribution in terms of diagnostic quality, especially with highly heterogeneous tissues, and currently in the literature there has been no comparison of these displacement estimators at the full-stiffness reconstruction level. Due to the nature of the reconstruction algorithm, which has in-built de-noising and tissue mechanics elements, it may prove that more advanced displacement estimators add unjustifiable computational processing for highly diminishing returns in terms of image quality.

The candidate algorithms of initial displacement estimation include analytic minimization in 2D (AM2D) [1,2], Global Ultrasound Elastography (GLUE) [3], OVERWIND [4], and SOUL [5]. These were chosen as candidates because they are well-motivated direct

calculation methods that vary in complexity and quality, while their codes are publicly available for use in research. They represent a wide range of methods, including first-order derivatives, second-order derivatives, and window-based approaches. This study provides unique insight into the performance of these displacement estimators considering computational time restrictions (real-time rates) and at a wholly new full reconstruction level. Full stiffness reconstruction leading to tissue Young's modulus images is a much more direct method to interpret the results of elastography, which may vastly improve the readability of these images.

2.2 Methods

2.2.1 Strain Refinement Algorithm

The strain-enhancement (STREAL) method presented in [6] has three major steps: Laplacian filtering, incompressibility enforcement, and compatibility enforcement. The first is the simplest: a Laplacian operator is applied to reduce the noise in the displacement image. Then the incompressibility of the tissues is enforced to further enhance the quality of the displacement field. Then the compatibility of tissues, which is interpreted as tissue displacement continuity enforcement, is enforced to compute high-quality axial and lateral strain images. The overall method is described in Figure 2.1. Tissue incompressibility enforcement relies on an assumption of the underlying tissue behavior. Sometimes this follows the plane strain behavior assumption, where out-of-plane strains are assumed to be negligible. In most cases, including clinical applications, the plain strain assumption is insufficient; hence, the Boussinesq model is used to approximate the 3D tissue deformation based on a semi-infinite medium mechanics [7].

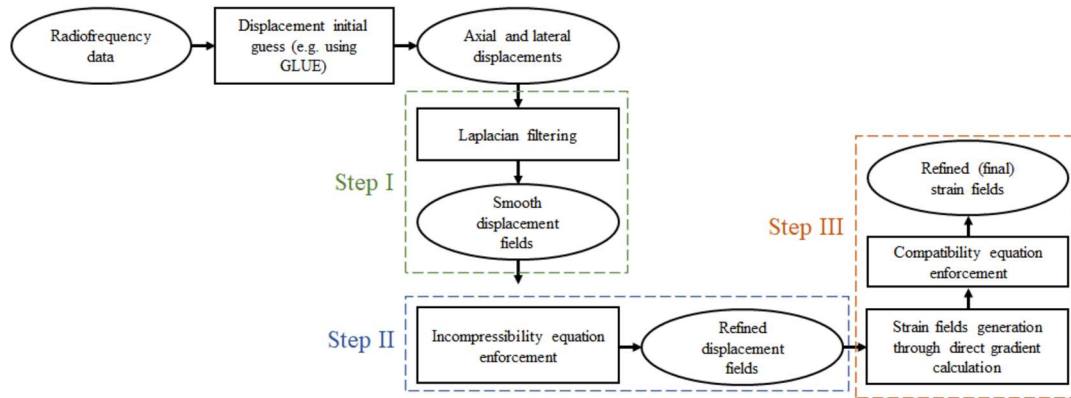


Figure 2.1 An overview of the STREAL methodology and its 3-step process. The first step is a second order derivative filtering procedure. The second step enforces the incompressibility of tissue. The third step enforces the compatibility of tissue (no apparent tearing). Note that this procedure requires an estimate of out-of-plane deformation. Figure taken from [7].

2.2.2 Data Generation

Three kinds of data were used for this investigation: fully in-silico ultrasound data, a tissue-mimicking phantom, and clinical data.

Full synthetic in-silico ultrasound data was generated by first running a simulation of tissue compression in ABAQUS (ABAQUS 2019, Dassault Systèmes Simulia Corp., Johnston, RI, USA) with a strain level of 1% and then using the FIELD II toolbox [8,9] using a central frequency of 5 MHz. To generate this data, scatterers were simulated and then displaced using the nodal displacements generated from the ABAQUS simulation. Twenty-three different phantom models, including uni-focal and multi-focal phantoms with inclusion stiffnesses ranging from 40 to 60 kPa and background stiffnesses from 18 to 23 kPa, were simulated. The full method of generating in-silico ultrasound data is described in [10]. These phantoms reflect a “perfect” data acquisition scenario without any contamination with out-of-plane displacement or other irregularities. The synthetic data also allow for a large enough data sample to conduct statistical analyses on the performance

of these displacement estimators, which is normally not possible with the handful of tissue mimicking phantoms usually presented in similar investigations.

For another level of validation on non-synthetic data, a tissue mimicking phantom manufactured by the Computerized Imaging Reference Systems (CIRS; Norfolk, VA, USA) was used as a second level of control. The ultrasound probe was controlled with a mechanical device to apply displacement in 2.54 mm (0.1 inch) increments. The probe used was a VF10-5 linear array with a central frequency of 6.67 MHz and a sampling frequency of 40 MHz (Antares Siemens System – Issaquah, WA, USA). Finally, radiofrequency frame pairs of 3 patients were used from [2] to compare the differences in performance on clinical data acquired with the same ultrasound machine and probe. Note that the clinical data was segmented by a clinician using the B-Mode image available in [2]. Since the underlying segmentations are not publicly available, it was not possible to include the figure in this thesis. The tissue mimicking phantom was used to bridge the gap between entirely idealized data and clinical data to assess the performance of the estimators on high-quality but nonetheless “real” data.

2.2.3 Displacement Estimators

For each of the 23 models, the radiofrequency images were processed with the following displacement estimators:

- Analytic Minimization in 2D [3]
- Global Ultrasound Elastography [3]
- OVERWIND [4]
- Second-Order Ultrasound Elastography [5]

The resulting displacement and strain images were collected, and an estimate of run-time on an Intel i7 8700-based workstation was measured. The same was repeated on the tissue-mimicking phantoms and clinical data. Once these data were acquired, the displacements and strains were further improved using the STREAL algorithm in conjunction with the analytical Boussinesq model to estimate the out-of-plane strain [7,8].

2.2.4 Young's Modulus and Data Processing

An iterative reconstruction algorithm was used to recover the Young's modulus of all the data [12,13]. In this algorithm, an initial guess of the Young's modulus is made before a finite element (FE) model of the US field of view is generated, where the loading is provided as prescribed displacement boundary conditions obtained from the measured displacement field. The FE method is run, and based on the resulting stresses and the strain calculated from the US motion tracking, the Young's modulus is recalculated. This is repeated until the Young's modulus values converge. For the synthetic dataset, all generated data, including both pre- and post-STREAL, were used to reconstruct the Young's modulus (E) images, while this image reconstruction method was also carried out using the ground truth displacements obtained through the FE simulation. The synthetic reconstructed data was processed as follows:

1. The inclusion-to-background Young's modulus ratio was calculated, and a percent difference was calculated between the measured ratio using displacement estimators and the reconstruction performed with the ground-truth displacement. This can provide an idea of the diagnostic power of each estimator, as the ratio is what determines potential malignancy.
2. The Hausdorff distance was calculated between the border of the segmented inclusions of the synthetic data reconstruction and the ground truth reconstruction. This metric was chosen to measure the change in shape of the inclusion. Segmentation was performed with Otsu's method.
3. The mean squared error (MSE) between the resultant Young's modulus images and the ground truth was calculated.
4. The Young's modulus ratios, Hausdorff distance, and MSE were then statistically compared using an ANOVA test with Bonferroni corrections.
5. Using the same thresholding procedure as in step 2, the specificity, sensitivity, and kappa statistic were calculated for agreement with the ground truth for each displacement estimator.

Sensitivity, Specificity and the Kappa statistic were included to provide more diagnostically relevant error metrics, as they provide information about the behaviour of the imaging system. In general, sensitivity measures the chance that an area of pathology appears in the image, specificity measures the extent to which areas that appear in the image are actually pathological, and the kappa statistic is an accuracy measure that takes into account random chance agreement.

For the tissue mimicking phantom and clinical examples, strain images for the axial and lateral images were also generated, along with CNR, SNR, and inclusion to the background Young's modulus ratios. The CNR and SNR were calculated using two regions of interest, one on the inclusion and one on the background. Both regions were chosen manually based on the strain images and clinical segmentations such that the inclusion region encompasses the whole lesion while the background was chosen to be in the most homogenous region. Both regions were chosen to be as close in size as possible. One departure this thesis makes from normal practice is in the definition of SNR and CNR. In most cases, the denominator is the standard deviation of the signal, but in this investigation, we use the standard deviation of the background. This is because the lesions we observe are expected to be heterogenous, and so the normal formulation would be unfairly low, as the standard deviation would be high. However, the background is also heterogeneous, so CNR and SNR should be interpreted in a more qualitative manner, as a higher CNR and SNR may not actually reflect the underlying stiffness distribution. Therefore, CNR and SNR serve as more of a sanity check, and should not be discussed without mentioning or interpreting the resultant image.

2.3 Results

For each displacement estimator, with and without refinement using the STREAL method, Figure 2.2 illustrates errors in the reconstructed inclusion-to-background Young's modulus ratios, Hausdorff distances between the truth and reconstructed outlines of the inclusion, and MSE between ground truth and reconstructed Young's modulus images obtained for the phantoms' datasets. Statistical significance ($p < 0.05$) between results generated by pairs of displacement estimators, both with and without refinement using the

STREAL method, is also indicated in this figure. As seen in this figure, the AM2D displacement estimator with STREAL enhancement provides the most accurate inclusion-to-background Young's modulus reconstruction ratio, while, on average, the STREAL procedure reduces this error to less than one third compared to its pre-STREAL counterpart. The AM2D estimator with STREAL also leads to improved MSE, while its Hausdorff distance is not significantly different from other estimators. The latter implies that, compared to other estimators, while AM2D improves the quantitative distribution of the Young's modulus ratio significantly, it does not improve the estimated shape of the inclusion significantly. More information and a visual representation of the effects of the different displacement estimations are presented in Figure 2.4.

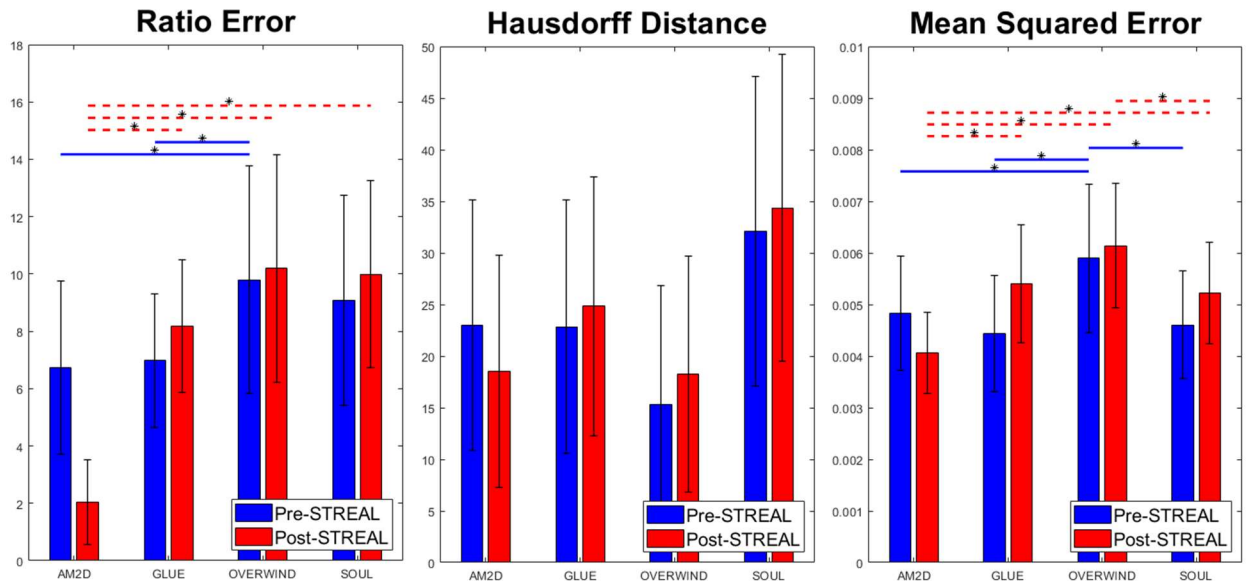


Figure 2.2 Errors in reconstructed inclusion-to-background Young's modulus ratios, Hausdorff distances between truth and reconstructed outlines of the inclusion, and MSE between ground truth and reconstructed Young's modulus images obtained using the four displacement estimation methods of AM2D, GLUE, OVERWIND, and SOUL with and without STREAL. The red and blue lines with stars indicate statistical significance ($p < 0.05$) between results generated by pairs of estimators. In this comparison, pre- and post-STREAL were separate groups; hence, the statistical comparisons are between estimators, not pre- and post-STREAL.

Table 2.1 Specificity, sensitivity, and kappa statistics for the agreement of thresholded inclusions of each displacement estimator compared to the ground truth.

Displacement Estimator	Specificity	Specificity	Sensitivity	Sensitivity	Kappa Statistic	Kappa Statistic
	Pre-STREAL	Post-STREAL	Pre-STREAL	Post-STREAL	Pre-STREAL	Post-STREAL
AM2D	0.99 ± 0.00	0.99 ± 0.01	0.96 ± 0.02	0.97 ± 0.03	0.92 ± 0.02	0.91 ± 0.02
GLUE	0.99 ± 0.00	0.98 ± 0.01	0.95 ± 0.04	0.95 ± 0.05	0.90 ± 0.02	0.88 ± 0.03
OVERWIND	0.99 ± 0.00	0.98 ± 0.01	0.93 ± 0.03	0.93 ± 0.05	0.90 ± 0.03	0.88 ± 0.03
SOUL	0.99 ± 0.01	0.98 ± 0.01	0.94 ± 0.02	0.94 ± 0.04	0.86 ± 0.03	0.85 ± 0.03

When applied to synthetic data, the AM2D estimator provides accurate inclusion to background Young’s modulus ratio estimation while preserving the quality of inclusion shape (Hausdorff distance). It generally compares well with the ground truth Young’s modulus distribution according to the small MSE values and very high specificity, sensitivity, and Kappa statistics, as can be seen in Table 2.1. In terms of runtime, however, AM2D runs in around 0.1 s, whereas GLUE, OVERWIND, and SOUL are approximately 8 s, 20 s, and 40 s, respectively. To compare the quality of the reconstructed Young’s modulus, Figure 2.3 illustrates an example obtained through processing a synthetic data sample. As can be seen, the AM2D estimator provides a faithful reconstruction of the Young’s modulus when combined with STREAL enhancement. The “ground truth” reconstruction image was obtained by processing the ground truth displacement field, which was used to move the scatterers, using the iterative Young’s modulus reconstruction algorithm described earlier.

To further compare the quality of Young’s modulus reconstruction in conjunction with each of the displacement field estimators, Figure 2.4 shows images of reconstructed Young’s modulus in tissue mimicking phantoms. Reconstructed images are shown for each displacement estimator with and without STREAL enhancement. This figure also

demonstrates that the AM2D estimator provides an accurate reconstructed image as compared to the “ground truth” image, but at a very low computational cost.

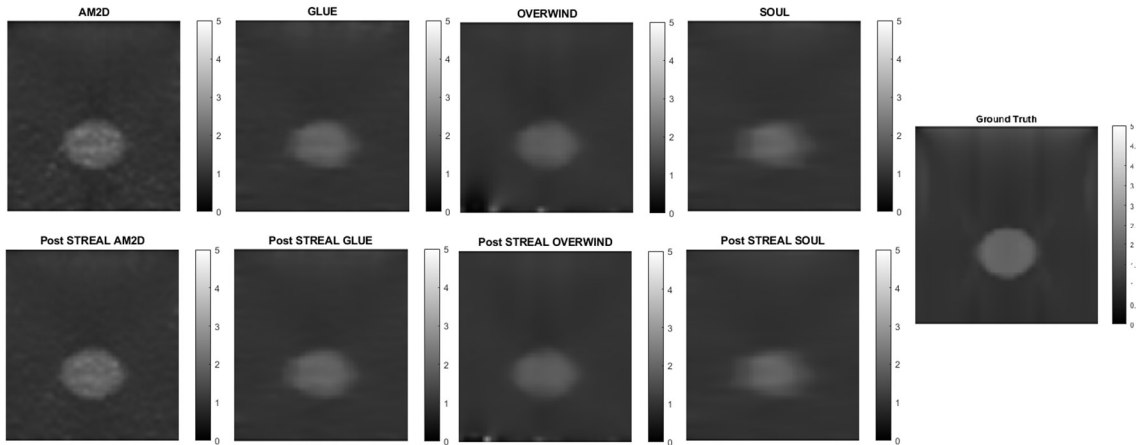


Figure 2.3 An example of Young’s modulus image reconstruction obtained with synthetic displacement data generated by each displacement field estimator with and without STREAL enhancement. The “ground truth” reconstruction image was obtained by processing the ground truth displacement field using the iterative Young’s modulus reconstruction algorithm.

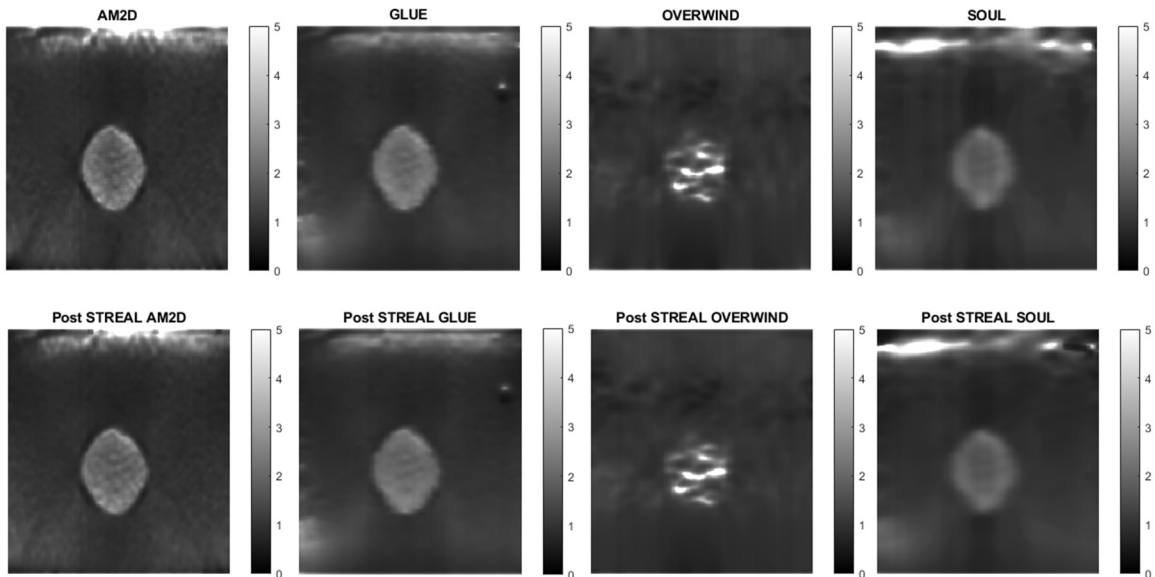


Figure 2.4 Reconstructed Young’s modulus images of a tissue mimicking phantom obtained with each displacement estimator with and without STREAL enhancement.

To evaluate the performance and effectiveness of the four displacement estimators in the context of quality of reconstructed Young's modulus images, contrast-to-noise ratio (CNR), signal-to-noise ratio (SNR), and inclusion-to-background Young's modulus ratios for each reconstructed image were computed, and results pertaining to the tissue mimicking phantom are summarized in Table 2.2. This table indicates that all estimators lead to high CNR and SNR for reconstructed Young's modulus images, while using STREAL enhancement with the AM2D and GLUE estimators leads to little change in the respective image CNR and SNR. The table shows that, among the estimators, OVERWIND consistently led to a substantial increase in the CNR and SNR of the reconstructed Young's modulus images. The ground truth inclusion to background Young's modulus ratio is 1.86. This indicates that the AM2D, GLUE, and SOUL displacement estimators lead to reasonably high accuracy, while the OVERWIND estimator shows poor performance in Young's modulus reconstruction.

Table 2.2 CNR, SNR, and inclusion to background Young's Modulus ratio values obtained for reconstructed Young's Modulus images of phantoms computed using each displacement estimator with and without STREAL.

Displacement Estimator	CNR	CNR	SNR	SNR	Ratio	Ratio
	Pre-STREAL	Post-STREAL	Pre-STREAL	Post-STREAL	Pre-STREAL	Post-STREAL
AM2D	38.3	34.4	19.9	17.9	2.08	2.08
GLUE	47.4	44.4	24.1	27.9	2.17	2.19
OVERWIND	35.6	44.7	21.7	27.8	2.6	2.7
SOUL	61.5	39.0	32.1	20.8	2.1	2.1

Strain imaging is common for obtaining approximate distribution tissue stiffness. To evaluate the performance and effectiveness of the four displacement estimators in the

context of strain image quality, axial and lateral strains pertaining to the phantoms' dataset were analyzed. Figure 2.5 illustrates axial strain images of the tissue mimicking phantom obtained with each displacement estimator, with and without STREAL enhancement. Table 2.3 presents results summary of corresponding CNR, SNR and Young's modulus ratio values obtained for the phantom dataset using each displacement estimator with and without STREAL enhancement. The figure and table indicate that the AM2D estimator provides a reasonably good-quality axial strain image but at a very low computational cost compared to other estimators. The table also indicates that the CNR and SNR values of axial strain images were slightly improved through the application of STREAL enhancement. Furthermore, while they have further deviation from the true values, the Young's ratio values obtained from these images once again shows that AM2D leads to the most accurate estimates.

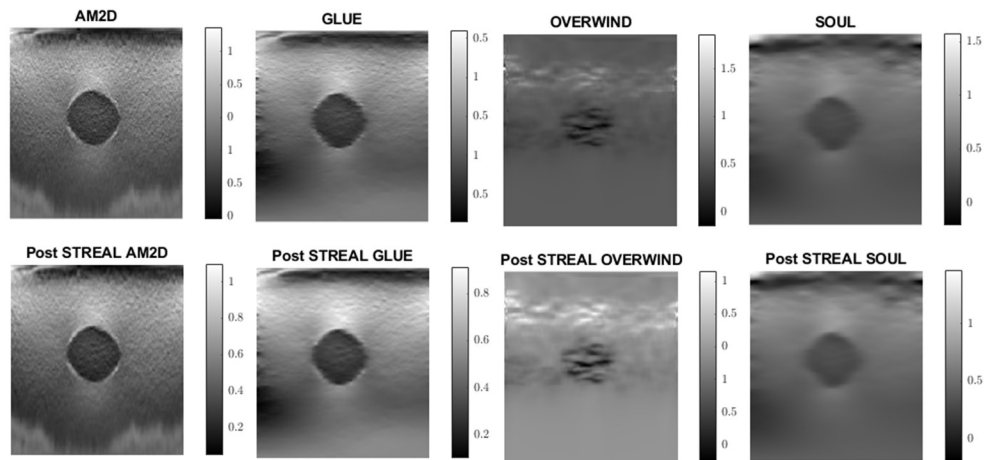


Figure 2.5 Axial Strain Images of the tissue mimicking phantom obtained using each displacement field estimator applied with and without STREAL enhancement. The differences between each image and its STREAL version are subtle.

Table 2.3 CNR and SNR values obtained for axial strain images of tissue mimicking phantom computed using each displacement estimator with and without STREAL.

Displacement Estimator	CNR	CNR	SNR	SNR	Ratio	Ratio
	Pre-STREAL	Post-STREAL	Pre-STREAL	Post-STREAL	Pre-STREAL	Post-STREAL
AM2D	12.6	14.55	1.15	1.4	2.22	2.19
GLUE	11.6	11.7	4.7	4.8	2.88	2.87
OVERWIND	48.0	48.4	46.2	46.9	4.0	3.95
SOUL	28.6	28.9	7.7	7.9	2.59	2.61

Similar analysis was performed to evaluate the quality of lateral strain images using each of the displacement estimators with and without STREAL. As an example, Figure 2.6 illustrates lateral strain images of the tissue mimicking phantom obtained with each displacement estimator, with and without STREAL. Table 2.4 presents results summary of pertinent CNR and SNR values obtained for the phantom dataset using each displacement estimator with and without STREAL. The figure and table indicate that the CNR and SNR improvements of lateral strain achieved through STREAL are highly remarkable. More particularly, Figure 2.6 shows that, through STREAL, the lateral strain image obtained with the AM2D estimator transforms from almost an entirely noisy image to a relatively high-quality image where the inclusion is highly distinguishable. This is confirmed by the data given in Table 2.4 which shows that the CNR and SNR were increased by factors of over 20 and 5.3 times, respectively. It is noteworthy that the strain ratios are not reported in the table as lateral strains do not provide a good estimate of this ratio due to the high spatial variability of the stresses in the lateral direction.

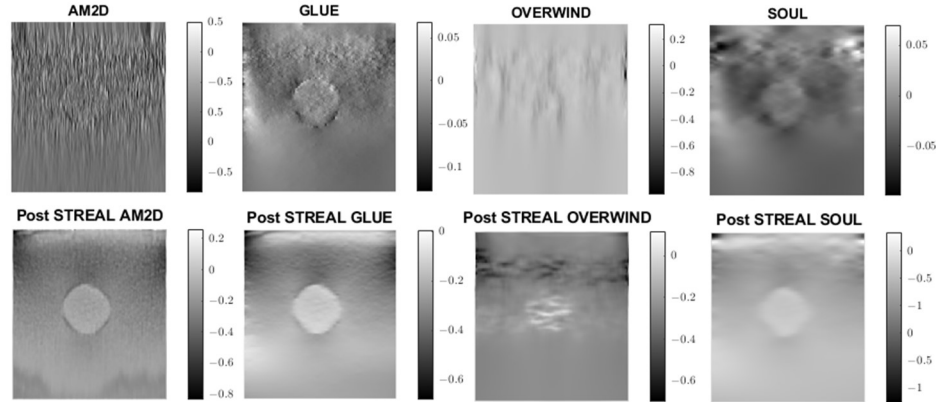


Figure 2.6 Lateral strain images of the tissue mimicking phantom obtained using each displacement field estimator applied with and without STREAL. Lateral strain images obtained with STREAL enhanced show remarkable improvement over their pre-enhancement counterparts.

Table 2.4 CNR and SNR values obtained for lateral strain image of the tissue mimicking phantom computed using each displacement estimator with and without STREAL.

Displacement Estimator	CNR		SNR	
	Pre-STREAL	Post-STREAL	Pre-STREAL	Post-STREAL
AM2D	0.47	9.7	0.29	0.45
GLUE	6.8	16.8	2.2	4.5
OVERWIND	3.3	17.5	10.0	29.9
SOUL	7.1	14.3	1.67	2.2

For evaluating the performance of the displacement estimators with and without STREAL on clinical data, constructed Young's modulus, axial strain and lateral strain images pertaining to 3 patients in the dataset are presented. Figures 2.7, 2.8 and 2.9 show images of the reconstructed Young's modulus, axial strain and lateral strain of, respectively for Patient 1. Similarly, Figures 2.10, 2.11 and 2.12 show images of the reconstructed

Young's modulus, axial strain and lateral strain, respectively for Patient 2, while Figures 2.13, 2.14 and 2.15 show images of the reconstructed Young's modulus, axial strain and lateral strain, respectively for Patient 3. Each reconstruction is associated with a table of CNR, SNR and young's modulus ratio (Tables 2.5-2.7). Generally, the quality of all images generated using the OVERWIND estimator is poor compared to images generated using other estimators. Except OVERWIND estimator, other estimators led to reasonably high-quality images. Among AM2D, GLUE and SOUL estimators, AM2D led to noisier images while it preserved necessary information, including stiffness values and tumor shape. This once again indicates the advantage of the AM2D estimator which has much higher computational efficiency at the cost of losing little image quality. Like the phantom case, it is also observed that STREAL has the highest influence on lateral strain images with all estimators. Again, this enhancement transforms almost entirely noisy lateral strain images to high-quality images where both tumor shape and its stiffness can be estimated. For lateral strain images, the STREAL in conjunction with AM2D, GLUE and SOUL estimators demonstrates remarkable improvement as this enhancement transforms very low-quality images to images where the tumors are quite distinguishable.

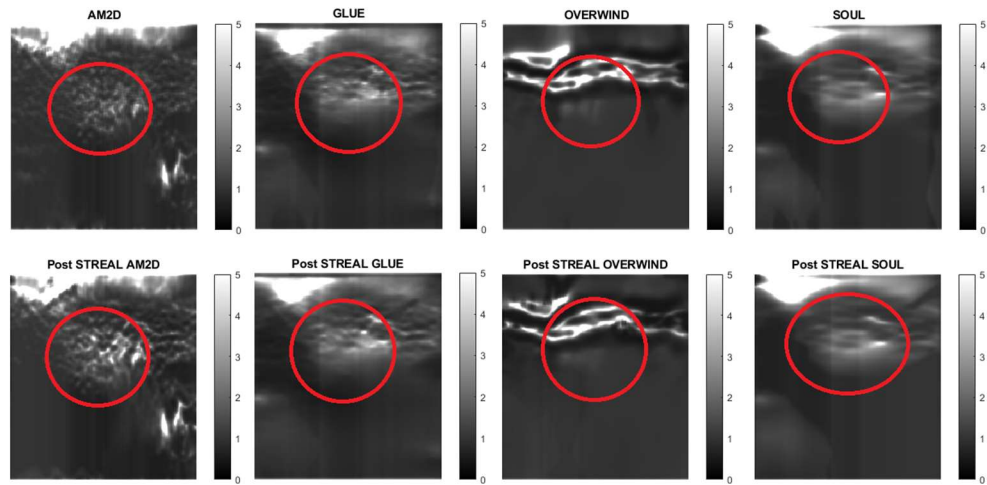


Figure 2.7 Reconstructed Young's modulus images of Patient 1 computed from displacement fields obtained by each displacement estimator with and without STREAL. Approximate tumor ROI is highlighted in red based on outlines provided in [2]. AM2D provides reasonably high-quality images at a very low computational cost.

Table 2.5 CNR, SNR and Inclusion to background ratios obtained for stiffness images of Patient 1 computed using each displacement estimator with and without STREAL.

Displacement Estimator	CNR	CNR	SNR	SNR	Ratio	Ratio
	Pre-STREAL	Post-STREAL	Pre-STREAL	Post-STREAL	Pre-STREAL	Post-STREAL
AM2D	32.9	658.0	14.7	416.7	1.8	2.7
GLUE	15.2	15.7	5.5	5.9	1.6	1.6
OVERWIND	42.0	42.2	15.3	15.0	1.6	1.6
SOUL	9.8	10.6	2.1	2.2	1.3	1.3

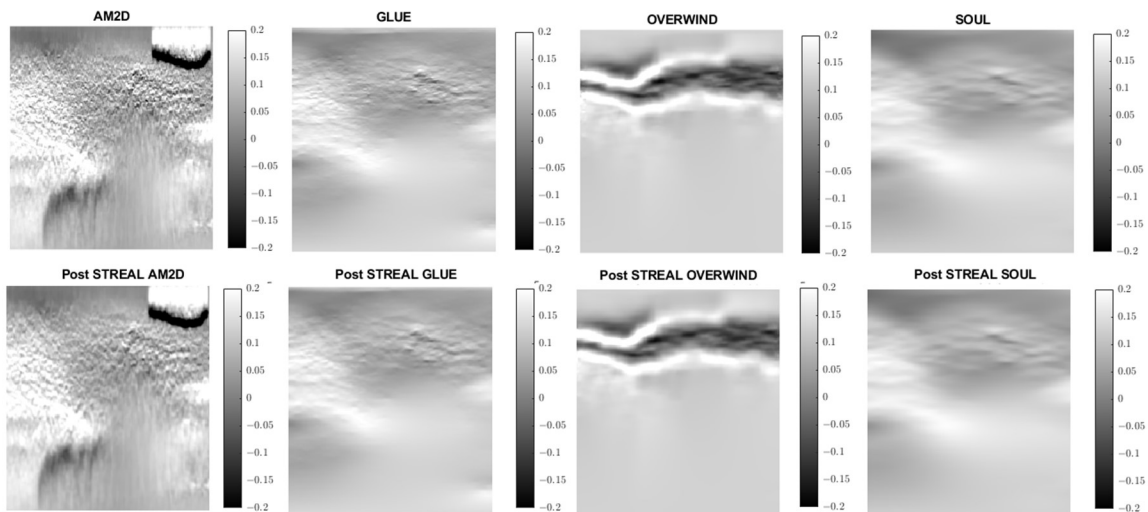


Figure 2.8 Axial strain images of Patient 1 computed from displacement fields obtained by each displacement estimator with and without STREAL. AM2D provides reasonably high-quality images at a very low computational cost.

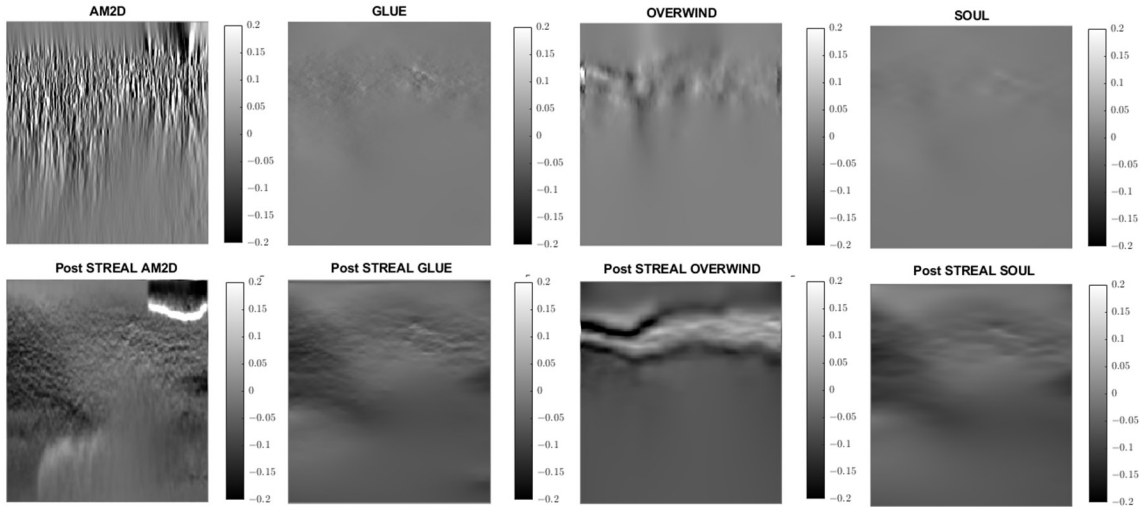


Figure 2.9 Lateral strain images of Patient 1 computed from displacement fields obtained by each displacement estimator with and without STREAL. AM2D with STREAL provides reasonably high-quality images at a very low computational cost.

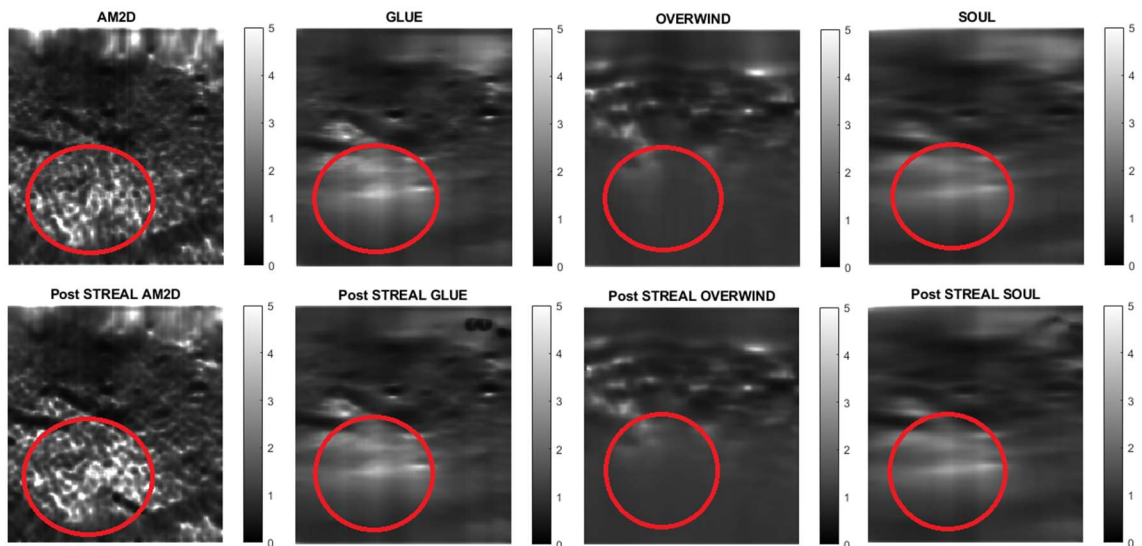


Figure 2.10 Reconstructed Young's modulus images of Patient 2 computed from displacement fields obtained by each displacement estimator with and without STREAL. Approximate tumor ROI is highlighted in red [2]. AM2D provides a reasonably high-quality image at a very low computational cost.

Table 2.6 CNR, SNR and inclusion to background ratio values obtained for axial strain images of Patient 2 computed using each displacement estimator with and without STREAL.

Displacement Estimator	CNR	CNR	SNR	SNR	Ratio	Ratio
	Pre-STREAL	Post-STREAL	Pre-STREAL	Post-STREAL	Pre-STREAL	Post-STREAL
AM2D	10.1	16.3	7.0	12.3	3.3	4.1
GLUE	14.6	15.1	9.8	9.7	3.0	2.8
OVERWIND	3.1	3.36	0.62	0.72	1.2	1.27
SOUL	16.4	17.2	10.2	11.1	2.6	2.83

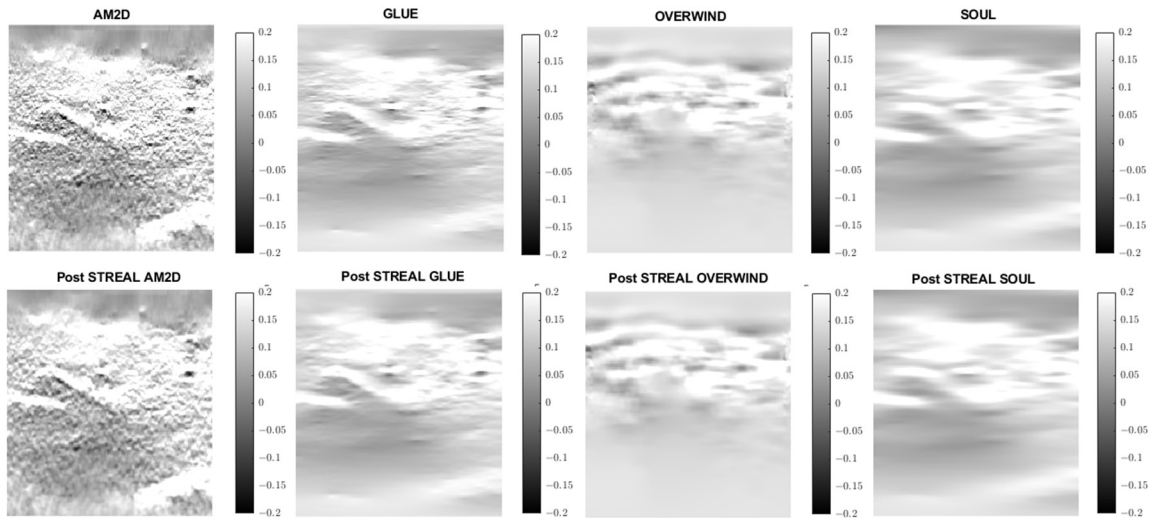


Figure 2.11 Axial strain images of Patient 2 computed from displacement fields obtained by each displacement estimator with and without STREAL. AM2D provides reasonably high-quality images at a very low computational cost.

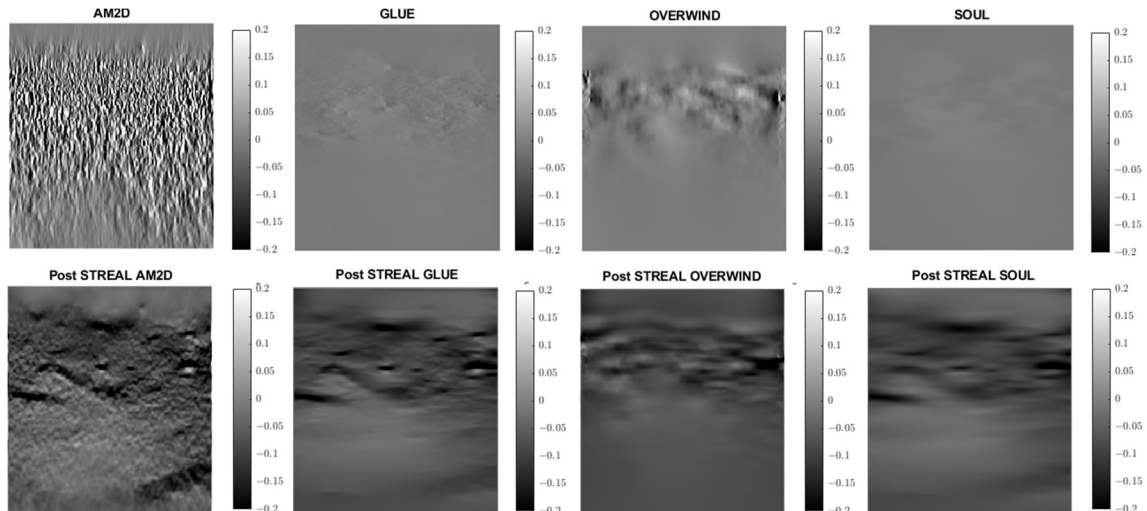


Figure 2.12 Lateral strain images of Patient 2 computed from displacement fields obtained by each displacement estimator with and without STREAL. AM2D with STREAL provides reasonably high-quality images at a very low computational cost.

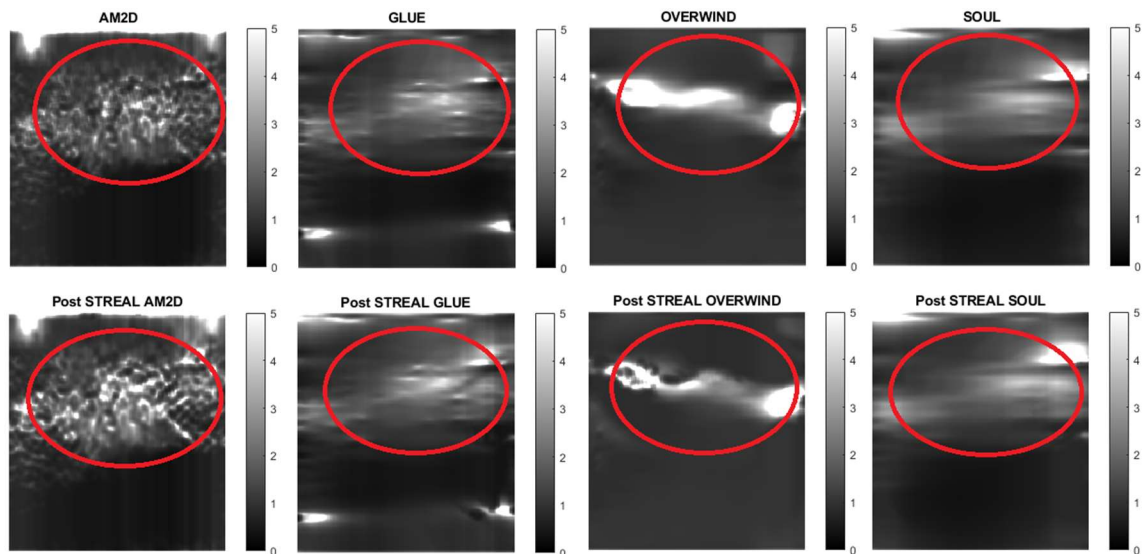


Figure 2.13 Reconstructed Young's modulus images of Patient 3 computed from displacement fields obtained by each displacement estimator with and without STREAL. Approximate tumor ROI is highlighted in red [2]. AM2D provides a reasonably high-quality image at a very low computational cost.

Table 2.7 CNR, SNR, and inclusion to background values obtained for stiffness images of Patient 3 computed using each displacement estimator with and without STREAL

Displacement Estimator	CNR	CNR	SNR	SNR	Ratio	Ratio
	Pre-STREAL	Post-STREAL	Pre-STREAL	Post-STREAL	Pre-STREAL	Post-STREAL
AM2D	50.0	35.1	40.7	29.6	5.4	6.3
GLUE	12.6	10.6	9.5	7.4	4.0	3.3
OVERWIND	59.1	89.3	37.8	44.0	2.8	2.0
SOUL	40.9	34.9	34.4	27.1	5.9	2.7

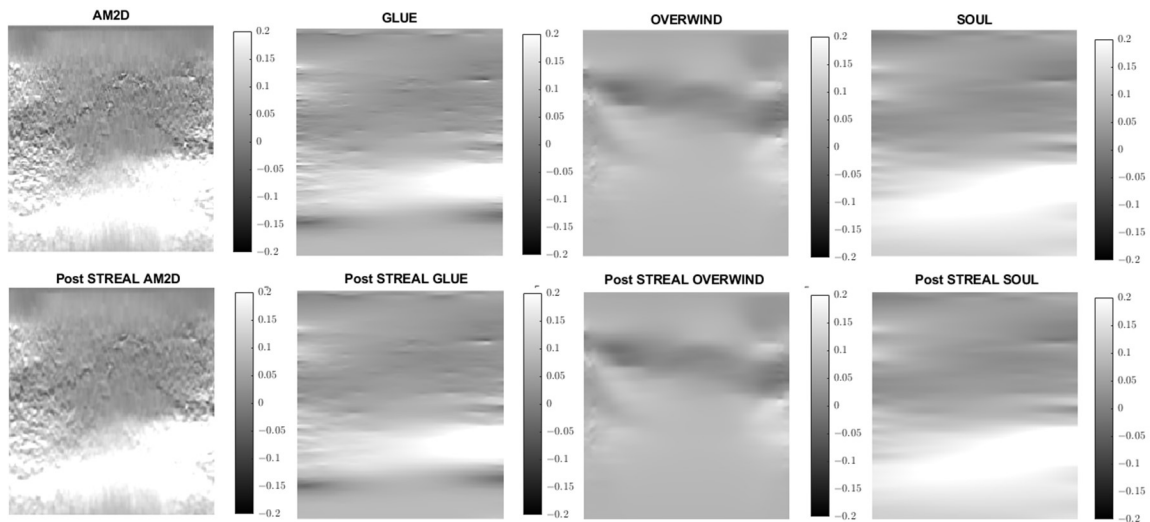


Figure 2.14 Axial strain images of Patient 3 computed from displacement fields obtained by each displacement estimator with and without STREAL. AM2D provides reasonably high-quality images at a very low computational cost.

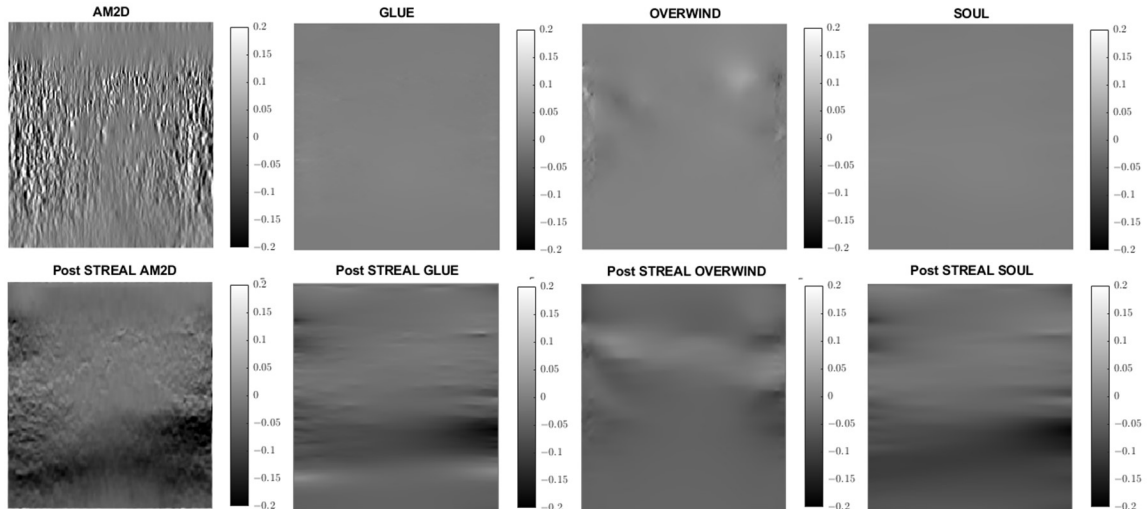


Figure 2.15 Lateral strain images of Patient 3 computed from displacement fields obtained by each displacement estimator with and without STREAL. AM2D with STREAL provides reasonably high-quality images at a very low computational cost.

Overall, in all images the AM2D estimator shows a good ability of clearly showing increased stiffness with clear heterogeneity within the tumor. GLUE and SOUL show much smoother versions of the same image in AM2D, while OVERWIND provides only some increase in the stiffness of the ROI. Figure 2.16 shows a hypothetical image fusion of B-mode and Young's modulus image generated for Patients 1, 2 and 3 that can be provided in the clinic. The Young's modulus images are obtained through data inversion of displacements computed by the AM2D estimator with STREAL.

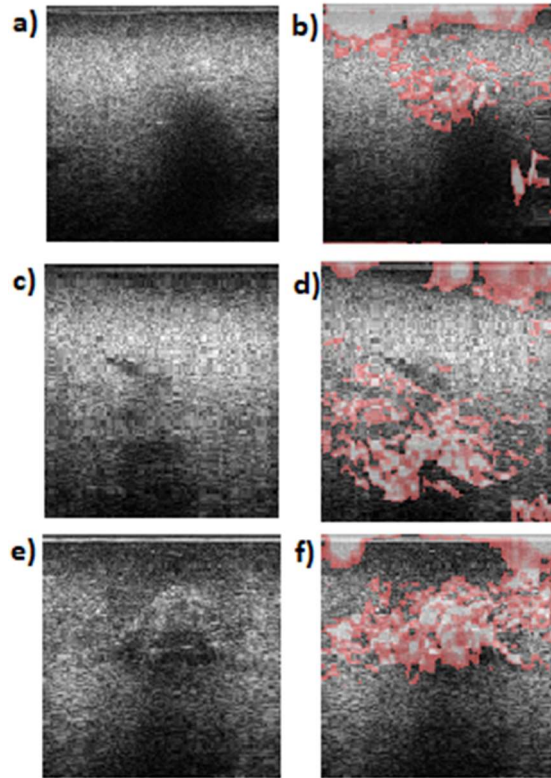


Figure 2.16 B-Mode images alongside Segmented Young's modulus images computed from displacements estimated through the AM2D estimator with STREAL, which are overlaid on top of B-mode images of a) and b) Patients 1, c) and d) Patient 2 and e) Patient 3. Highlighted are regions with Young's modulus values larger than 1.5 times the median of Young's modulus of respective background tissue. Apart from artefacts at the top of the images, the stiffness elevation in the tumor area is consistent with their respective ROIs. Moreover, the stiffness image reveals features that are not immediately obvious from the B-Mode.

2.4 Discussion

This investigation evaluates the performance of four commonly used tissue displacement estimation methods developed for US elastography. The methods are, namely, AM2D, GLUE, OVERWIND, and SOUL. They were evaluated both as stand-alone methods and in combination with the STREAL method, which was recently developed to enhance tissue displacement fields aimed at US elastography applications.

The assessment was performed using datasets consisting of data pertaining to in-silico and tissue mimicking phantoms undergoing US imaging in addition to clinical data. When applied to synthetic data, compared with the other measures, the AM2D displacement estimator, by far, provides the best quality of Young's modulus reconstruction with much higher computational efficiency compared to other estimators. This estimator has the added benefit of substantially improving the inclusion-to-background Young's modulus ratio when combined with the STREAL method founded on tissue mechanics regularization. The other displacement estimators tend to blur the edges of the inclusion, which may be the source of the ratio error as it leads to the underestimation of the inclusion's Young's modulus. The in-silico phantoms results indicate that both OVERWIND and SOUL estimators provide minimal improvements over GLUE but take much longer to compute compared to AM2D. This makes them difficult to recommend in a real-time scenario where run-time is of the utmost importance. Tissue mechanics-based regularization applied through the STREAL method provides the most improvement when applied to the AM2D estimator. This may be partially due to the displacement field over-smoothing effect applied in other methods, which can lead to excessive loss of actual displacement information. Furthermore, the more advanced and complicated displacement estimators have increasingly many parameters, which makes it more difficult to accurately tune the algorithm for maximum performance. Moreover, the sophisticated window-based approach in OVERWIND was designed to handle large changes in displacement and preserve value; however, it is possible that this same mechanism can sometimes allow artifacts and issues in the displacement field to pass through where they otherwise should be smoothed. SOUL, on the other hand, provides a much smoother image than GLUE; however, the former risks excessive smoothing, while the potential benefit is not worth the increased runtime and should be reconsidered if its algorithm implementation is optimized.

When applied to the tissue mimicking phantom, the AM2D estimator performed very well relative to the other estimator as it produces high-quality images for a very low runtime requirement. The quality of the reconstructed images measured by CNR and SNR is comparable, while the STREAL led to little change in these measures except for OVERWIND, where the enhancement led to substantial improvement. For strain images,

the STREAL led to only a little improvement of axial strain with all four displacement estimators, whereas the improvement achieved with the lateral strain was highly remarkable, especially with the AM2D estimator. This observation is consistent with [7]. Overall, the difference in reconstruction quality with and without STREAL is quite subtle and, in some cases, seems to decrease CNR and SNR. The decrease in metrics is of relatively trivial magnitude compared to the overall CNR and SNR and could be attributed to subtle changes in the noise content. Nonetheless, the idealistic nature of the tissue mimicking phantoms and indeed the in-silico phantoms means that the quality of the axial displacement alone is enough to reconstruct the Young's modulus with high quality. While this indicates that STREAL has left little room for improvement in the studied phantoms, the impacts of STREAL are best exemplified in the clinical cases where the prominence of the inclusion was increased since the noise in these cases is substantial in both axial and lateral directions.

In the clinical cases presented in this investigation, the AM2D estimator provides Young's modulus images with remarkable heterogeneity. While this is consistent with a heterogeneous stiffness distribution expected in tumor tissue, a lack of underlying ground truth makes this difficult to ascertain. The GLUE estimator provides a more homogenous-appearing mass, which may be more appealing to clinicians. Moreover, the OVERWIND and SOUL estimators do not appear to provide a significant benefit as compared to the GLUE estimator, which has a significantly higher runtime. It must be noted that the CNR/SNR and ratios of the clinical reconstruction should be interpreted cautiously as the underlying stiffness distribution and, more importantly, its heterogeneity are unknown; hence naïve comparisons of SNR and CNR are not appropriate as the true variance in the background is not known. When looking at situations where STREAL seems to decrease SNR and CNR, this should not be taken to be an "inferior" image, as it is quite likely that increased heterogeneity being captured in the image could cause decreased SNR and CNR. Therefore, qualitative assessment of the produced images are of the utmost importance. When looking at sensitivity, specificity, and kappa statistics, all four displacement estimators perform extremely well (excess of 0.9), and none emerges as significantly superior, as with all metrics exceeding 0.9, differences are likely well beyond the point of

diminishing returns. Clinical investigation may be warranted to determine if these differences are clinically significant.

One important aspect of the AM2D estimator is its ability to create high quality strain images at high speed for real-time image assessment. This study indicates that the AM2D estimator with STREAL is vastly superior in its quality to runtime ratio, as can be seen in both the tissue mimicking phantom and clinical examples, where the inclusion or tumor is clearly visible.

It is noteworthy that with all of the tissue motion tracking techniques using US, the quality of the estimated displacement field is highly dependent on the consistency of the selected pair of RF frames corresponding to the pre- and post-compression states of the tissue. In other words, the two frames must represent the same tissue plane as much as possible. The greater the deviation from this situation, the lower the quality of the estimated displacement field. The recently developed method known as PCA-GLUE [14], which is a variant of the GLUE method optimized with machine learning, can be used for assessing RF frame pair quality. Given the high speed of the AM2D displacement estimator, it should also be possible to consider it a good candidate for real-time frame pair quality assessment before near imaging at near real-time rates. This concept is demonstrated in the flowchart shown in Figure 2.18. A clinician would use this system to image the breast or liver during a routine ultrasound screening procedure, potentially bypassing the need for biopsy.

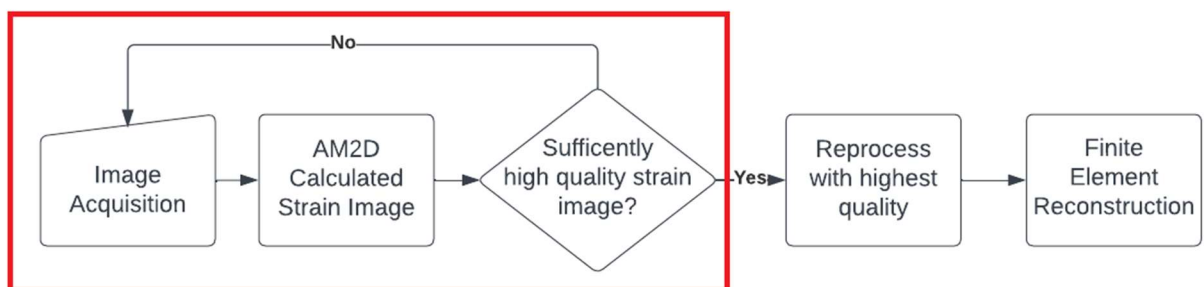


Figure 2.17 A hypothetical flow chart for a real-time US elastography system that could be deployed in the clinical setting. The red box indicates a real-time loop that the clinician

can use to assess the quality of images in real time, where once a sufficiently high-quality strain image is found, it can be processed to reconstruct a reliable Young's modulus image.

This investigation clearly demonstrates the image quality superiority of full-reconstruction imaging, where it is observed that SNR and CNR values are substantially higher for the tissue mimicking phantom at the reconstructed Young's modulus level compared to their strain image counterparts. Moreover, Young's modulus images are much easier to interpret, as can be seen in Figures 2.7, 2.10, and 2.13, with an overlay indicating substantially (1.5+ x than background tissue) stiffer tissue.

Some limitations of this study include the small number of tissue mimicking and clinical examples and the lack of underlying validation for the stiffness field of the clinical examples. Some future suggestions for this work would be to develop better tissue-mimicking samples that include heterogeneity, whether synthetic or physical, to evaluate the preservation of heterogeneity in the sample. Another obvious future direction is including a large clinical study to achieve more concrete conclusions. Moreover, a prototype imaging system should be developed and taken to clinical trials to determine which displacement estimator results in improved decision-making ability. Alternatively, data could be collected along with biopsy-confirmed results to attempt to create a diagnostic criterion for this new generation elastography system.

Some notable non-inclusions in this study are normalized correlation coefficient methods and their variants, and deep-learning-based methods. Normalized correlation coefficient methods were not included in this investigation because the quality of the strain images; they produce low-quality displacement fields compared to the selected four estimators. The lack of sufficient quality associated with these methods is expected to impact reconstructed Young's modulus images [15,16]. Moreover, Normalized correlation coefficient methods are not as computationally efficient as dynamic programming methods. Deep-learning-based methods were also not included in this investigation, as the performance of the network is highly dependent on the training data and the very specific architecture used [11,17–21], and deep learning methods should be evaluated on a case-by-case basis. Moreover, this investigation is primarily a CPU-based comparison; hence,

including deep learning would lead to largely invalid conclusions about computation efficiency, as either they would be unfairly hampered by running on CPU or unfairly advantaged by running on GPU.

The diagnosis of breast cancer is an inherently multi-faceted and non-binary process where clinicians must consider many different sources of evidence and come to a probability of malignancy or benign findings, which will inform the clinical course of action. Mathematical tools have been developed for this precise situation, including Dempster-Shafer Theory (DS Theory) and Fuzzy Logic, which are meant to provide a mathematical framework for integrating multiple sources of evidence and to deal with “continuous” logic, where probabilities are used rather than Boolean values.

DS Theory is based upon Bayesian theories of subjective probability. It deals with mathematical constructs called “belief functions,” which integrate the answers to one question to influence the confidence or “belief” in a related question. In the domain of breast cancer diagnosis, it has been used to create new neural network methodologies that integrate multiple measures of breast lesion texture and pharmacokinetic parameters [22] to achieve superior results compared to traditional classifiers.

Fuzzy logic was developed specifically to handle situations in which the truth value of some statement is not a Boolean value and is in fact a continuum between 0 and 1. In the case of breast cancer, it is not simply enough to assign it malignant or benign, as it cannot be known whether all benign lesions will remain that way or whether a malignant lesion will necessarily become life-threatening (overdiagnosis). Fuzzy logic was developed to tackle such an issue and has been used in diagnostic methods specifically to diagnose breast cancers [23].

The potential future direction of this work is to integrate the elastography technique identified as highly effective into such classification methodologies to improve the accuracy of breast cancer detection systems. Moreover, combination imaging systems could be explored, for instance using compression due to mammography to create a dual mammography-elastography system.

2.5 Conclusion

These results show that at the full-reconstruction level the choice of algorithm is highly data-quality dependent. If high quality data is reasonably available, simpler displacement estimators like AM2D may be used to great effect, however I hypothesize that when dealing with imperfect data, GLUE may be a better option with some optimization required. As it currently stands, OVERWIND and SOUL are too computationally intensive to be considered in a real-time system despite potentially yielding better results.

2.6 References

- [1] H. Rivaz, E. Boctor, P. Foroughi, R. Zellars, G. Fichtinger, and G. Hager, “Ultrasound Elastography: A Dynamic Programming Approach,” *IEEE Trans Med Imaging*, vol. 27, no. 10, pp. 1373–1377, Oct. 2008, doi: 10.1109/TMI.2008.917243.
- [2] H. Rivaz, E. M. Boctor, M. A. Choti, and G. D. Hager, “Real-time regularized ultrasound elastography,” *IEEE Transactions on Medical Imaging*, vol. 30, no. 4, pp. 928–945, Apr. 2011. doi:10.1109/tmi.2010.2091966
- [3] M. Ashikuzzaman, C. J. Gauthier, and H. Rivaz, “Global Ultrasound Elastography in Spatial and Temporal Domains,” *IEEE Trans Ultrason Ferroelectr Freq Control*, vol. 66, no. 5, 2019, doi: 10.1109/TUFFC.2019.2903311.
- [4] H. S. Hashemi and H. Rivaz, “Global Time-Delay Estimation in Ultrasound Elastography,” *IEEE Trans Ultrason Ferroelectr Freq Control*, vol. 64, no. 10, pp. 1625–1636, Oct. 2017, doi: 10.1109/TUFFC.2017.2717933.
- [5] M. Mirzaei, A. Asif, and H. Rivaz, “Combining Total Variation Regularization with Window-Based Time Delay Estimation in Ultrasound Elastography,” *IEEE Trans Med Imaging*, vol. 38, no. 12, pp. 2744–2754, Dec. 2019, doi: 10.1109/TMI.2019.2913194.

- [6] M. Ashikuzzaman and H. Rivaz, "Second-Order Ultrasound Elastography With L1-Norm Spatial Regularization," *IEEE Trans Ultrason Ferroelectr Freq Control*, vol. 69, no. 3, 2022, Accessed: Aug. 23, 2022. [Online]. Available: <https://ieeexplore.ieee.org/document/9674909/>
- [7] N. Kheirkhah, S. Dempsey, A. Sadeghi-Naini, and A. Samani, "A novel tissue mechanics-based method for improved motion tracking in quasi-static ultrasound elastography," *Med. Phys.*, vol. 50, no. 4, pp. 2176–2194, Apr. 2023, doi: 10.1002/MP.16110.
- [8] N. Kheirkhah, A. Sadeghi-Naini, and A. Samani, "Analytical Estimation of Out-of-plane Strain in Ultrasound Elastography to Improve Axial and Lateral Displacement Fields," *Proceedings of the Annual International Conference of the IEEE Engineering in Medicine and Biology Society, EMBS*, vol. 2020-July, pp. 2055–2058, Jul. 2020, doi: 10.1109/EMBC44109.2020.9176086.
- [9] J. A. Jensen, "Field: A Program for Simulating Ultrasound Systems," *Med Biol Eng Comput*, vol. 34, no. sup. 1, pp. 351–353, 1997, Accessed: Sep. 13, 2023. [Online]. Available: <https://orbit.dtu.dk/en/publications/field-a-program-for-simulating-ultrasound-systems>
- [10] J. A. Jensen and N. B. Svendsen, "Calculation of Pressure Fields from Arbitrarily Shaped, Apodized, and Excited Ultrasound Transducers," *IEEE Trans Ultrason Ferroelectr Freq Control*, vol. 39, no. 2, pp. 262–267, 1992, doi: 10.1109/58.139123.
- [11] A. K. Z. Tehrani and H. Rivaz, "Displacement Estimation in Ultrasound Elastography Using Pyramidal Convolutional Neural Network," *IEEE Trans. Ultrason. Ferroelectr. Freq. Control*, vol. 67, no. 12, 2020, Accessed: Aug. 24, 2022. [Online]. Available: <https://ieeexplore.ieee.org/document/8990076/>

- [12] A. Samani, J. Bishop, and D. B. Plewes, "A constrained modulus reconstruction technique for breast cancer assessment," *IEEE Trans Med Imaging*, vol. 20, no. 9, pp. 877–885, Sep. 2001, doi: 10.1109/42.952726.
- [13] M. M. Doyley, P. M. Meaney, and J. C. Bamber, "Evaluation of an iterative reconstruction method for quantitative elastography," *Phys. Med. Biol*, vol. 45, pp. 1521–1540, 2000.
- [14] A. Zayed, S. Member, H. Rivaz, and S. Member, "Fast Strain Estimation and Frame Selection in Ultrasound Elastography Using Machine Learning," *IEEE Trans Ultrason Ferroelectr Freq Control*, vol. 68, no. 3, 2021, doi: 10.1109/TUFFC.2020.2994028.
- [15] J. Luo and E. Konofagou, "A fast normalized cross-correlation calculation method for motion estimation," *IEEE Trans Ultrason Ferroelectr Freq Control*, vol. 57, no. 6, pp. 1347–1357, 2010, doi: 10.1109/TUFFC.2010.1554.
- [16] M. Mirzaei, A. Asif, M. Fortin, and H. Rivaz, "3D normalized cross-correlation for estimation of the displacement field in ultrasound elastography," *Ultrasonics*, vol. 102, p. 106053, Mar. 2020. doi:10.1016/j.ultras.2019.106053
- [17] D. Perdios, M. Vonlanthen, F. Martinez, M. Arditi, and J. P. Thiran, "CNN-Based Ultrasound Image Reconstruction for Ultrafast Displacement Tracking," *IEEE Trans Med Imaging*, vol. 40, no. 3, pp. 1078–1089, 2021, doi: 10.1109/TMI.2020.3046700.
- [18] A. K. Z. Tehrani, M. Sharifzadeh, E. Boctor, and H. Rivaz, "Bi-Directional Semi-Supervised Training of Convolutional Neural Networks for Ultrasound Elastography Displacement Estimation," *IEEE Trans Ultrason Ferroelectr Freq Control*, vol. 69, no. 4, 2022, Accessed: Aug. 23, 2022. [Online]. Available: <https://ieeexplore.ieee.org/document/9694663/>
- [19] A. Mallampati and M. Almekkawy, "Measuring Tissue Elastic Properties Using Physics Based Neural Networks," in *LAUS 2021 - 2021 IEEE UFFC Latin America*

Ultrasonics Symposium, Proceedings, IEEE, 2021. doi:
10.1109/LAUS53676.2021.9639231.

[20] C. Hoerig, J. Ghaboussi, and M. F. Insana, “Data-Driven Elasticity Imaging Using Cartesian Neural Network Constitutive Models and the Autoprogressive Method,” *IEEE Trans Med Imaging*, vol. 38, no. 5, 2019, doi: 10.1109/TMI.2018.2879495.

[21] A. K. Z. Tehrani, M. Amiri, and H. Rivaz, “Real-time and High Quality Ultrasound Elastography Using Convolutional Neural Network by Incorporating Analytic Signal,” in *2020 42nd Annual International Conference of the IEEE Engineering in Medicine & Biology Society (EMBC)*, IEEE, 2020. Accessed: Aug. 23, 2022. [Online]. Available: <https://ieeexplore.ieee.org/document/9176025/>

[22] Z. Liu *et al.*, “A classifier-combined method for grading breast cancer based on Dempster-Shafer evidence theory,” *Quant. Imaging Med. Surg.*, vol. 13, no. 5, pp. 3288–3297, 2023, doi: 10.21037/qims-22-652.

[23] N. F. Idris and M. A. Ismail, “Breast cancer disease classification using fuzzy-ID3 algorithm with FUZZYDBD method: Automatic fuzzy database definition,” *PeerJ Comput. Sci.*, vol. 7, pp. 1–22, 2021, doi: 10.7717/PEERJ-CS.427.

Chapter 3

3 Elastosynth – An Open-source software package for the generation of realistic in-silico data for ultrasound elastography

A variant of this chapter will be submitted as a journal paper for publication in Computer Methods and Programs in Biomedicine

3.1 Introduction

As discussed in Section 1.10 on current issues with ultrasound elastography, the lack of data quality can affect the development of new displacement estimation techniques, as it becomes extremely difficult to determine if an algorithm fails due to a fundamental flaw, or due to a lack of data quality. Moreover, it is currently very difficult to properly evaluate the performance of displacement estimators as clinical data has no ground truth for comparison, and phantoms are too simple to draw definitive conclusions about performance on clinical data.

This has turned the literature towards synthetic or fully in-silico generation of tissue mimicking phantoms. To this end, other researchers have utilized finite element solvers like ABAQUS, combined with ultrasound simulation software like FIELD II [1,2]. This method is used to simulate the elastography procedure to generate “perfect data” with an underlying ground truth which provides a necessary accuracy assessment of displacement estimation.

These synthetic datasets have been used extensively, however, there are two major limitations. First, the FIELD II system is very computationally intensive, which limits the number of samples that can be generated. Moreover, ABAQUS or any other finite element solver does not normally support highly heterogeneous simulations in a user-friendly way.

This is generally because highly heterogeneous simulations are niche applications that do not appear in many other contexts.

To address this gap, I have developed an open-source code that solves both issues by optimizing the FIELD II system and creating a custom finite element solver which natively supports simulation of highly heterogeneous tissue. I have also developed a procedural generation algorithm which, given some parameters, can randomly generate unique and heterogeneous ultrasound elastography phantoms. The proposed US data generation algorithm employs an optimization procedure that reduces the run-time of the generation procedure by several orders of magnitude. This allows for the mass generation of many unique phantoms with heterogeneity that mimics clinical cases. This will allow for a realistic assessment of displacement algorithm quality that achieves statistical significance.

3.2 Background

The current state-of-the-art in “control” procedures in ultrasound elastography is quite meager, generally restricted to manufactured tissue mimicking phantoms or synthetic phantoms [3,4]. Tissue mimicking phantoms are essentially homogenous samples with a single or very few circular inclusions. Such phantoms suffer from two issues: 1) infeasible to manufacture a large number of tissue mimicking phantoms often necessary for developing machine learning based algorithms, 2) impracticality to manufacture phantoms with continuous heterogeneity which mimics biological tissues. As such, researchers have pursued US data generation in-silico where FIELD II [1,2] can be employed. In the context of such in-silico phantoms, the major reason behind the popularity of generating phantoms with homogenous tissue parts is the lack of a user-friendly way to specify highly heterogeneous finite element simulation necessary to estimate post-compression scatterer displacements. This is largely because all major finite element solvers are not designed to support continuously variable stiffness fields and are mostly designed to deal with large sections of homogenous materials, which is a much more common workflow in other fields of engineering. This poses a major problem since biological tissues can be highly heterogeneous. This leads to a situation where it becomes very difficult to properly validate algorithms developed in a situation where a ground truth is unavailable for comparison.

This gives rise to the first design objective – achieve a user-friendly way to specify and simulate ultrasound interaction with arbitrarily complex material properties. This will allow researchers to generate high-fidelity synthetic data to properly assess the merits of developed ultrasound elastography techniques, including tissue motion tracking algorithms.

3.3 Design Considerations

As discussed in the previous section, this software package has two major design considerations that can be extended as follows:

1. Create a convenient image-based way to specify arbitrarily heterogenous material properties field.
2. Provide a convenient procedural simulation functionality to generate massive amounts of unique elastography samples.
3. Devise an adaptable and convenient workflow support ranging from automatic data generation to customizable simulations.
4. Accelerate the runtime of data generation.

3.4 Methods and Capabilities

The overall capabilities of this software package are broken down into 3 major modules. Table 3.1 describes the 3 modules and their general roles and capabilities.

Table 3.1 An overview of the three major modules contained within Elastosynth. Each module has a specific task and can be used independently of each other. The first is the procedural phantom generator, which is used to generate phantom geometry based on parameters provided. The second module performs finite element modelling, which is responsible for simulating the compression of the phantom. The final module generates the radiofrequency data using FIELD II.

Procedural Phantom Generation	Finite Element Modelling	Radiofrequency Data Generation
Responsible for generating unique phantoms based on pre-determined parameters for inclusion numbers, inclusion sizes, stiffnesses and tissue heterogeneity.	Responsible for simulating the mechanical behaviour of specified phantoms based on specified boundary conditions, generating a displacement field for US data simulation.	Uses FIELD II to simulate the radiofrequency data based on the simulated phantom and a specified transducer and image options.

3.4.1 Procedural Phantom Generation

The procedural phantom generator is chiefly responsible for the generation of unique phantoms for ultrasound elastography, capable of randomly generating phantoms based on

parameters that control the number of inclusions, their sizes, their stiffnesses, and the degree of heterogeneity on an inclusion-by-inclusion basis. The first major methodology innovation involves the randomization of inclusion locations, which uses a Monte-Carlo approach to make sure that the inclusions are in a valid configuration. Figure 3.1 describes the algorithm.

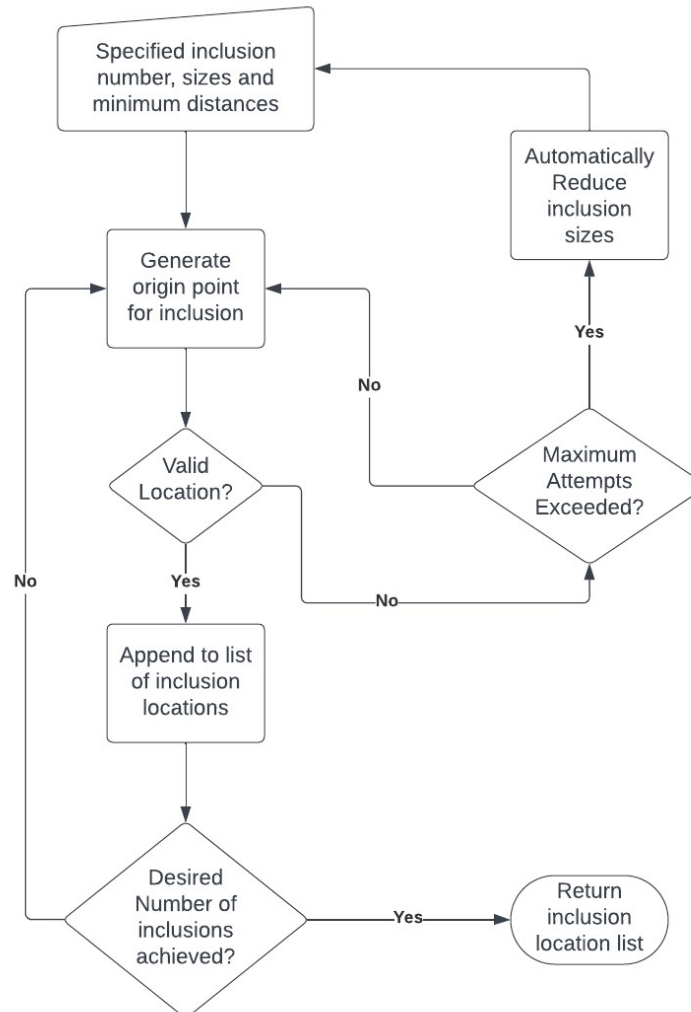


Figure 3.1 The algorithm used to generate randomized inclusion locations for the elastography phantom uses a Monte-Carlo approach to finding valid locations.

The algorithm begins with a set of inclusion sizes, minimum distances between inclusions and the number of inclusions. The function begins with a randomly generated point to

correspond to the location of the first inclusion. Then, for each subsequent inclusion, a random location is generated and checked for validity (non-overlapping, respecting minimum distance between inclusions), this continues until the location is accepted or the maximum attempts elapse. If successful, the inclusion location is appended to an array and the process is repeated until the desired number of inclusions is generated. If the maximum attempts elapse, the specified inclusion sizes are reduced and overwritten, and the algorithm is run again.

The next major capability of the procedural phantom generation module is the heterogeneity generator function, which takes homogenous inclusions and backgrounds and turns them into heterogenous stiffness fields based on specified parameters. Figure 3.2 illustrates the process.

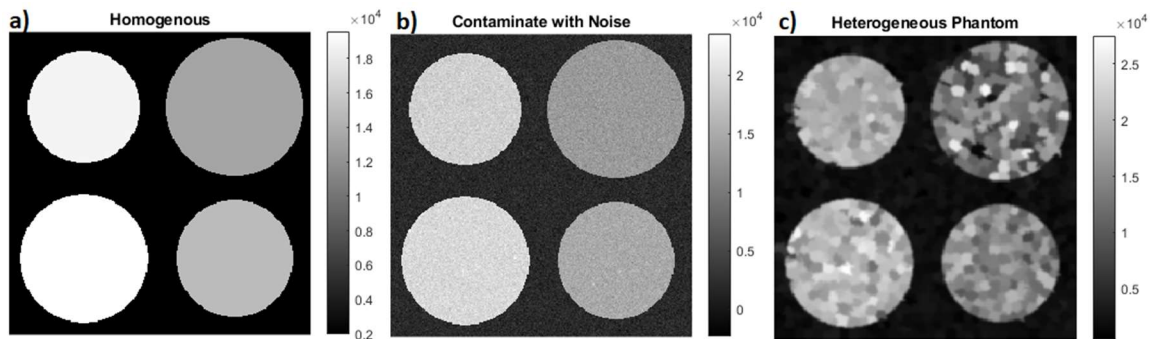


Figure 3.2 Generation of a heterogeneous stiffness field from an initially homogenous image (a). This was achieved through a three step process which begins with noise contamination of the homogenous phantom (b), followed by superpixel segmentation and then further changing the superpixel E values which results in a heterogeneous phantom (c).

The generation of heterogeneous phantoms is a 3-step process. It begins with a “clean” stiffness image with homogenous inclusions and background, with randomized stiffnesses. The second step is to contaminate the image with Gaussian noise to generate the first layer of heterogeneity. This noisy image is then segmented into a variable number of regions based on a super-pixel segmentation algorithm which groups pixels into larger regions based on proximity and similarity. The regions are then reassigned to generate the resultant image, however in each region the mean stiffness is changed based on a randomly

generated value which increases or decreases the local stiffness within the super-pixel. This allows for each super-pixel to have a slightly different Young's modulus, leading to heterogenous regions in the resultant image.

3.4.2 Finite Element Modelling

The finite element engine of the software is a bespoke solver written in C++, using the Armadillo matrix library, designed specifically for use with highly heterogenous stiffness images. The tradeoff for this stiffness heterogeneity is that the simulator only simulates 2D grid-based simulations to emulate ultrasound elastography. Moreover, because it does not require many of the preprocessing and validation, steps that normally precede an analysis in more traditional finite element software can be sidestepped, making it a light-weight solver module. Figure 3.3 illustrates a sample displacement and strain output from a plane stress phantom. In this phantom, a zero-displacement boundary condition was imposed at the bottom, and a prescribed displacement of 0.5 mm at the top. As can be seen, the heterogeneity of the inclusions and the background is apparent.

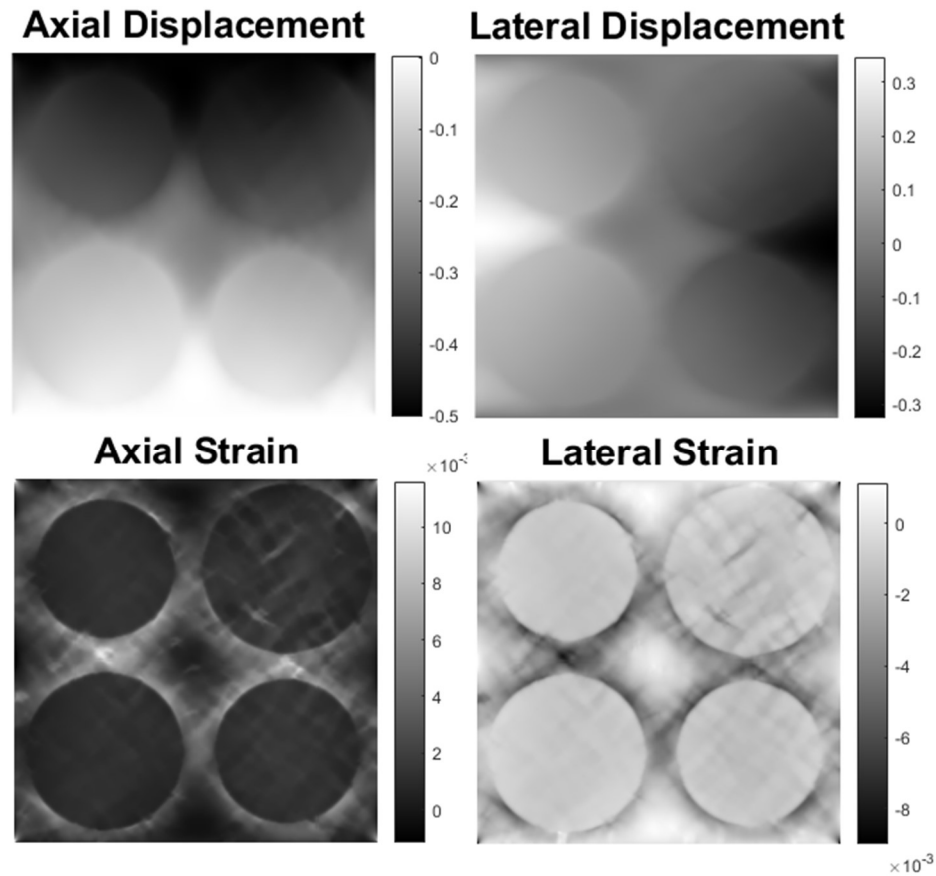


Figure 3.3 Finite element simulation of the phantom illustrated in Figure 3.2. See Figure 4.1 for strain images simulated using a homogenous sample.

3.4.3 Generation of Radiofrequency Data

The overwhelming majority of the generation of radiofrequency data is performed by FIELD II [1,2], in terms of the radiofrequency data generation. A general overview of the method is given below:

1. Generate a scatterer field with prescribed scattering coefficients.
2. Specify transducer specification.
3. Calculate the acoustic pressure field from the transducer emission.
4. Solve the wave equation approximately to estimate the return signals.
5. Repeat for each line in the radiofrequency data.

The code process is largely unaltered, however, to capture the deformation of the underlying tissues, two ultrasound images are generated, the first of which has unaltered scatterers, and the second is generated by moving the scatterers based on the finite element simulation where the displacement at each scatterer is interpolated from the finite element simulation. Figure 3.4 shows the scatterer-by-scatterer displacement values.

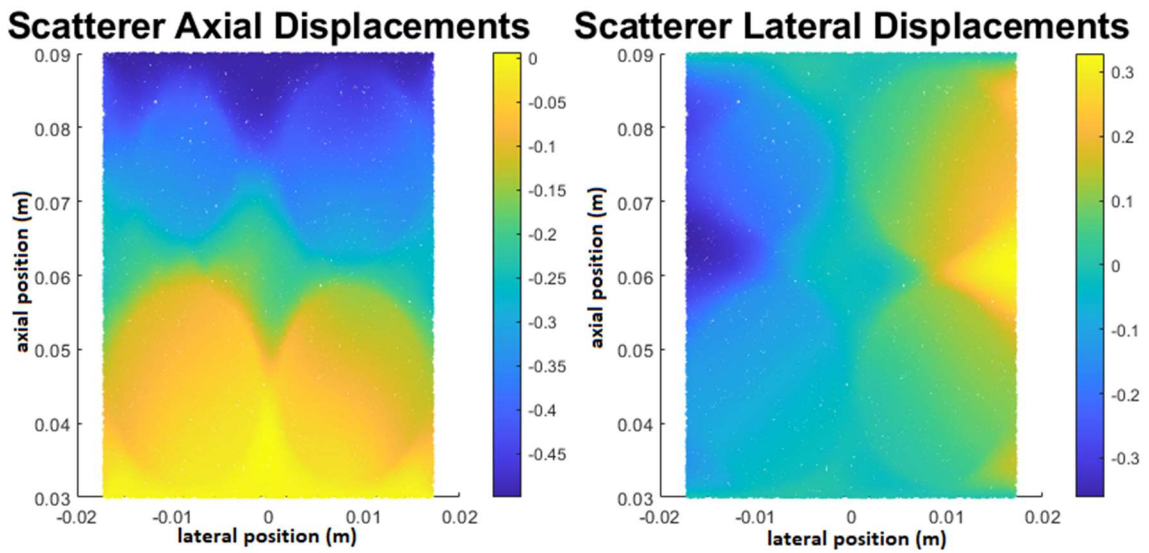


Figure 3.4 Scatterer displacements used to move the scatterers in the generation of the second frame. These were taken from the finite element simulation and resampled to the location of the randomly generated scatterers.

3.5 Comparison to Clinical Data

Figure 3.5 illustrates a comparison of a synthetically simulated sample compared with a real clinical sample taken from Chapter 2 after being passed through AM2D, STREAL and the iterative reconstruction algorithm. As can be seen, the heterogeneity of the synthetic example is very realistic, although the background appears to be too heterogeneous. Moreover, the regions of heterogeneity in the clinical example seem to be larger. However, both parameters can be controlled in the generation of synthetic samples. The most unrealistic thing about these data is the shape of the inclusion, however that can be manually specified. This shows that displacement estimators can be used on synthetic data,

and it can be compared to the known ground truth. This addresses the problem that quantitative measurement is very difficult, as clinical scenarios have no ground truth.

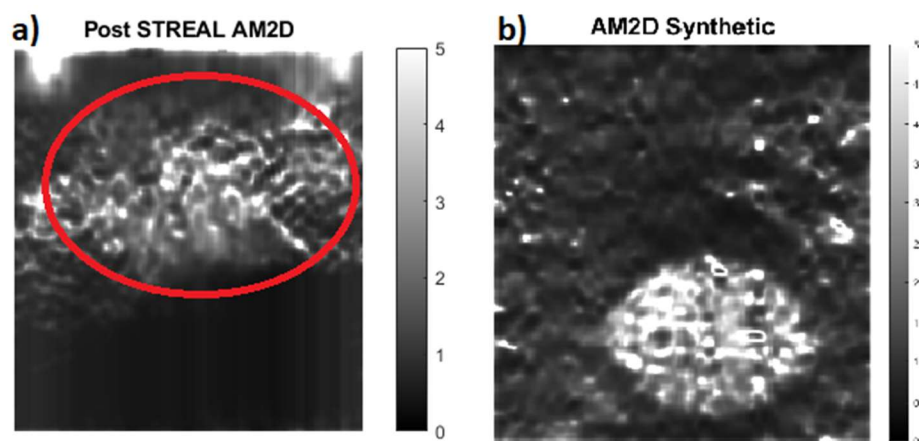


Figure 3.5 A comparison of Young's modulus reconstruction using clinical data (a) with a tumor in the circled ROI versus a reconstruction with a synthetic data sample (b). As can be seen, both images show very similar heterogeneity patterns, illustrating that heterogeneity has been effectively captured.

3.6 Optimization Procedure

To address the issue of long compute times, an optimization procedure is introduced by which the scatterers involved in the calculation of the radiofrequency response of the tissues are truncated to only those within a certain distance of the query points.

Normally, the entire response from all scatterers is calculated from the pressure wave emission, however the actual signal calculated in the post-beamformed data from the software is only influenced by the scatterers near the desired sampling points. As can be seen in Figure 3.6, there is no degradation of the displacement estimation even when only 1% of scatterers on either side of the A-Line are used. Displacement degradation is only seen when 0.7% of the scatterers are used. Even so, 1% yields two orders of magnitude speed improvement, which allows for the generation of hundreds of thousands of samples in the time it took to generate several thousand, unlocking dataset sizes that may allow robust deep learning methodologies.

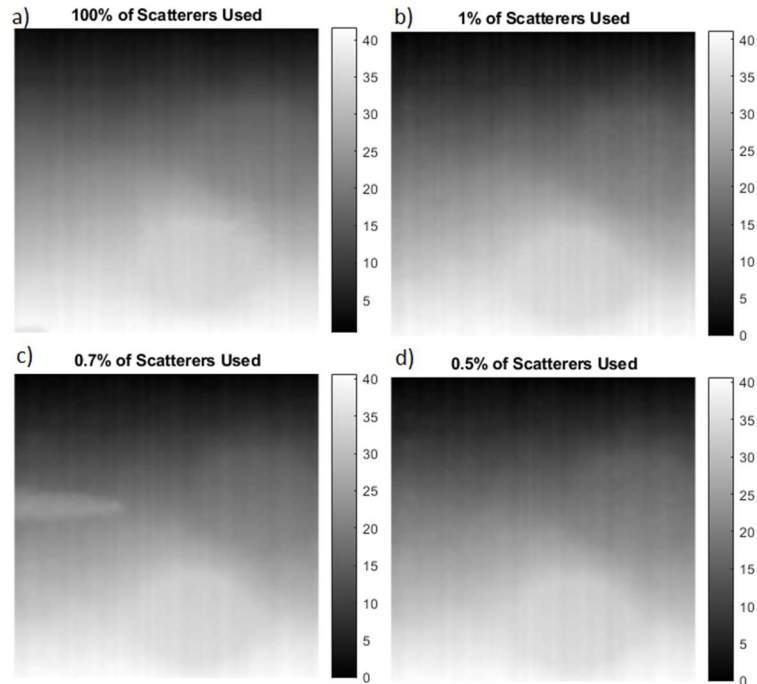


Figure 3.6 Displacement estimation using synthetic data where 100% (a), 1% (b), 0.7% (c), and 0.5% (c) of the scatterers are used, as can be seen, an artefact only appears at 0.7%, which means 1% can be safely used.

3.7 Supported Workflows

Figure 3.7 is a flow chart describing the currently supported workflows. Note that this may not be a complete list as of the publication of this document, as future updates may have led to added features. There is a main pathway that starts from the generation of a parameter dataset, which contains information required for creating phantoms, it then proceeds to a generator, which creates the underlying Young's modulus distribution. Finally, the finite element results then flow from the finite element solver all the way to the radiofrequency generator. At each stage, however, the user can inject their own custom data into the process, bypassing the previous steps.

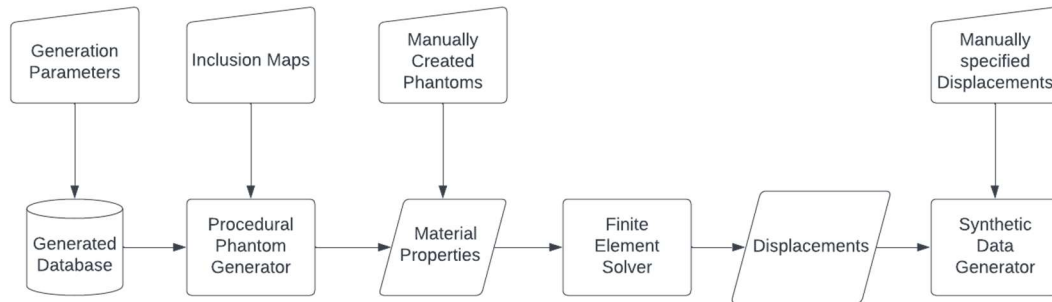


Figure 3.7 Currently supported workflows. The main workflow includes starting from a parameter dataset and flowing through the whole generation pipeline. However, at every opportunity, the user may input custom data into the process to avoid earlier steps, allowing for manual and custom phantom generation.

In general, user inputs can be done at any step in the process. From left to right, the most general and automated workflow is to specify a series of parameters to generate any number of phantoms completely systematically. The next supported workflow allows manual specification of inclusion maps and using the in-built heterogeneity generator. If the material properties to be simulated are known, they may be specified explicitly. Finally, if the desired displacements are known, they may be specified to be used directly by the radiofrequency pair generator.

3.8 Discussion and Significance

This software sets out and successfully achieves the goal of creating a user-friendly package for the creation of synthetic ultrasound elastography data. We implemented a procedural RF data generation software which can generate data pertaining to randomly distributed, uniquely heterogenous inclusions within a specified field of view. Moreover, a finite element solver was implemented with the goal of dealing with continuously variable stiffness field, subject to the constraint that the finite element simulation is a square field of view. Moreover, the radiofrequency simulation portion of the process was optimized, leading to computation acceleration of two orders of magnitude, allowing for massive numbers of generated data.

By significantly expanding the capabilities of in-silico synthetic data generation, new datasets of arbitrarily heterogenous examples can be generated to properly compare performance of algorithms with statistical significance. Moreover, with these new capabilities, we can generate more realistic clinical examples including well-integrated tumors without well-defined boundaries whereas this was previously impossible.

Future work includes expanding the simulation capabilities of the finite element solver to include more element types than just plane strain and plane stress. Moreover, using real clinical data to train generative artificial intelligence to generate models with high fidelity. Finally, adding the capability to simulate purposeful data corruption would be very useful.

3.9 Hardware/Software Specification and Distribution

There are no hardware specifications set in stone, however, a minimum of 8 GB of RAM is recommended for the finite-element simulations. The software is currently available in source code format or in Matlab toolbox format, precompiled for Windows and Linux. While compilation for Mac is expected to work, this has not been validated, nor provided as a pre-compiled software. Documentation is available upon request. The package itself is as of yet unreleased and will be released with the paper accompanying this chapter.

3.10 References

- [1] J. A. Jensen, "FIELD: A program for simulating ultrasound systems," *Med. Biol. Eng. Comput.*, vol. 34, no. SUPPL. 1, pp. 351–352, 1996, Accessed: Sep. 14, 2023. [Online]. Available: <https://orbit.dtu.dk/en/publications/field-a-program-for-simulating-ultrasound-systems>
- [2] J. A. Jensen and N. B. Svendsen, "Calculation of Pressure Fields from Arbitrarily Shaped, Apodized, and Excited Ultrasound Transducers," *IEEE Trans. Ultrason. Ferroelectr. Freq. Control*, vol. 39, no. 2, pp. 262–267, 1992, doi: 10.1109/58.139123.
- [3] N. Kheirkhah, A. Sadeghi-Naini, and A. Samani, "Analytical Estimation of Out-of-plane Strain in Ultrasound Elastography to Improve Axial and Lateral Displacement Fields," *Proc. Annu. Int. Conf. IEEE Eng. Med. Biol. Soc. EMBS*, vol. 2020-July, pp. 2055–2058, Jul. 2020, doi: 10.1109/EMBC44109.2020.9176086.
- [4] R. D. (Robert D. Cook, "Finite element modeling for stress analysis," p. 320, 1995, Accessed: Mar. 04, 2024. [Online]. Available: <https://www.wiley.com/en-us/Finite+Element+Modeling+for+Stress+Analysis-p-9780471107743>
- [5] N. Kheirkhah, S. Dempsey, A. Sadeghi-Naini, and A. Samani, "A novel tissue mechanics-based method for improved motion tracking in quasi-static ultrasound elastography," *Med. Phys.*, vol. 50, no. 4, pp. 2176–2194, Apr. 2023, doi: 10.1002/MP.16110.
- [6] A. K. Z. Tehrani and H. Rivaz, "Displacement Estimation in Ultrasound Elastography Using Pyramidal Convolutional Neural Network," *IEEE Trans. Ultrason. Ferroelectr. Freq. Control*, vol. 67, no. 12, 2020, Accessed: Aug. 24, 2022. [Online]. Available: <https://ieeexplore.ieee.org/document/8990076/>
- [7] Z. Liu *et al.*, "A classifier-combined method for grading breast cancer based on Dempster-Shafer evidence theory," *Quant. Imaging Med. Surg.*, vol. 13, no. 5, pp. 3288–3297, 2023, doi: 10.21037/qims-22-652.

- [8] N. F. Idris and M. A. Ismail, "Breast cancer disease classification using fuzzy-ID3 algorithm with FUZZYDBD method: Automatic fuzzy database definition," *PeerJ Comput. Sci.*, vol. 7, pp. 1–22, 2021, doi: 10.7717/PEERJ-CS.427.
- [9] A. Samani, J. Bishop, and D. B. Plewes, "A constrained modulus reconstruction technique for breast cancer assessment," *IEEE Trans. Med. Imaging*, vol. 20, no. 9, pp. 877–885, Sep. 2001, doi: 10.1109/42.952726.
- [10] A. Mallampati and M. Almekkawy, "Measuring tissue elastic properties using physics based Neural Networks," *2021 IEEE UFFC Latin America Ultrasonics Symposium (LAUS)*, Oct. 2021. doi:10.1109/laus53676.2021.9639231
- [11] J. Jiang and B. Peng, "A comparative study of displacement de-noising strategies: An in vivo feasibility study using 3D whole breast ultrasound data," *2018 IEEE International Ultrasonics Symposium (IUS)*, Oct. 2018. doi:10.1109/ultsym.2018.8579998
- [12] T. A. Krouskop, T. M. Wheeler, F. Kallel, B. S. Garra, and T. Hall, "Elastic moduli of breast and prostate tissues under compression," *Ultrason. Imaging*, vol. 20, no. 4, pp. 260–274, 1998, doi: 10.1177/016173469802000403.
- [13] D. Perdios, M. Vonlanthen, F. Martinez, M. Arditi, and J. P. Thiran, "CNN-Based Ultrasound Image Reconstruction for Ultrafast Displacement Tracking," *IEEE Trans. Med. Imaging*, vol. 40, no. 3, pp. 1078–1089, 2021, doi: 10.1109/TMI.2020.3046700.
- [14] C. Hoerig, J. Ghaboussi, and M. F. Insana, "Data-Driven Elasticity Imaging Using Cartesian Neural Network Constitutive Models and the Autoprogressive Method," *IEEE Trans. Med. Imaging*, vol. 38, no. 5, 2019, doi: 10.1109/TMI.2018.2879495.
- [15] J. L. Gennisson, T. Deffieux, M. Fink, and M. Tanter, "Ultrasound elastography: Principles and techniques," *Diagn. Interv. Imaging*, vol. 94, no. 5, pp. 487–495, May 2013, doi: 10.1016/J.DIII.2013.01.022.
- [16] T. Varghese, "Quasi-Static Ultrasound Elastography," *Ultrasound Clin.*, vol. 4,

no. 3, p. 323, Jul. 2009, doi: 10.1016/J.CULT.2009.10.009.

[17] H. S. Hashemi and H. Rivaz, "Global Time-Delay Estimation in Ultrasound Elastography," *IEEE Trans. Ultrason. Ferroelectr. Freq. Control*, vol. 64, no. 10, pp. 1625–1636, Oct. 2017, doi: 10.1109/TUFFC.2017.2717933.

[18] M. Mirzaei, A. Asif, and H. Rivaz, "Combining Total Variation Regularization with Window-Based Time Delay Estimation in Ultrasound Elastography," *IEEE Trans. Med. Imaging*, vol. 38, no. 12, pp. 2744–2754, Dec. 2019, doi: 10.1109/TMI.2019.2913194.

[19] H. Rivaz, E. M. Boctor, M. A. Choti, and G. D. Hager, "Ultrasound elastography using multiple images," *Medical Image Analysis*, vol. 18, no. 2, pp. 314–329, Feb. 2014. doi:10.1016/j.media.2013.11.002

[20] M. Mirzaei, A. Asif, and H. Rivaz, "Ultrasound elastography utilizing pre-beam-formed data," *2019 IEEE 16th International Symposium on Biomedical Imaging (ISBI 2019)*, Apr. 2019. doi:10.1109/isbi.2019.8759302

[21] N. Mohammadi, M. M. Doyley, and M. Cetin, "Combining physics-based modeling and Deep Learning for ultrasound elastography," *2021 IEEE International Ultrasonics Symposium (IUS)*, Sep. 2021. doi:10.1109/ius52206.2021.9593781

[22] M. Ashikuzzaman, T. J. Hall, and H. Rivaz, "Incorporating Gradient Similarity for Robust Time Delay Estimation in Ultrasound Elastography," *IEEE Trans. Ultrason. Ferroelectr. Freq. Control*, vol. 69, no. 5, pp. 1738–1750, May 2022, doi: 10.1109/TUFFC.2022.3164287.

[23] A. Khadem and S. K. Setarehdan, "Smoothing-spline based strain estimation in ultrasound elastography," *2007 IEEE International Conference on Signal Processing and Communications*, 2007. doi:10.1109/icspc.2007.4728410

[24] A. Zayed, S. Member, H. Rivaz, and S. Member, "Fast Strain Estimation and Frame Selection in Ultrasound Elastography Using Machine Learning," *IEEE Trans.*

Ultrason. Ferroelectr. Freq. Control, vol. 68, no. 3, 2021, doi: 10.1109/TUFFC.2020.2994028.

[25] M. Ashikuzzaman and H. Rivaz, "Second-Order Ultrasound Elastography With L1-Norm Spatial Regularization," *IEEE Trans. Ultrason. Ferroelectr. Freq. Control*, vol. 69, no. 3, 2022, Accessed: Aug. 24, 2022. [Online]. Available: <https://ieeexplore.ieee.org/document/9674909/>

[26] X. Wei *et al.*, "Unsupervised Convolutional Neural Network for Motion Estimation in Ultrasound Elastography," *IEEE Trans. Ultrason. Ferroelectr. Freq. Control*, vol. 69, no. 7, pp. 2236–2247, 2022, doi: 10.1109/TUFFC.2022.3171676.

[27] H. Rivaz, E. M. Boctor, M. A. Choti, and G. D. Hager, "Real-time regularized ultrasound elastography," *IEEE Transactions on Medical Imaging*, vol. 30, no. 4, pp. 928–945, Apr. 2011. doi:10.1109/tmi.2010.2091966

[28] H. Rivaz, E. Boctor, P. Foroughi, R. Zellars, G. Fichtinger, and G. Hager, "Ultrasound Elastography: A Dynamic Programming Approach," *IEEE Trans. Med. Imaging*, vol. 27, no. 10, pp. 1373–1377, Oct. 2008, doi: 10.1109/TMI.2008.917243.

[29] H. Li, J. Poree, B. Chayer, M.-H. Roy Cardinal, and G. Cloutier, "A global strain estimation algorithm for non-invasive vascular ultrasound elastography," *2019 IEEE International Ultrasonics Symposium (IUS)*, Oct. 2019. doi:10.1109/ultsym.2019.8925886

[30] Q. Zhang, Z. Cui, X. Niu, S. Geng, and Y. Qiao, "Image Segmentation with Pyramid Dilated Convolution Based on ResNet and U-Net," *Lect. Notes Comput. Sci. (including Subser. Lect. Notes Artif. Intell. Lect. Notes Bioinformatics)*, vol. 10635 LNCS, pp. 364–372, 2017, doi: 10.1007/978-3-319-70096-0_38/FIGURES/5.

[31] A. K. Z. Tehrani, M. Sharifzadeh, E. Boctor, and H. Rivaz, "Bi-Directional Semi-Supervised Training of Convolutional Neural Networks for Ultrasound Elastography Displacement Estimation," *IEEE Trans. Ultrason. Ferroelectr. Freq. Control*, vol. 69,

no. 4, 2022, Accessed: Aug. 24, 2022. [Online]. Available:
<https://ieeexplore.ieee.org/document/9694663/>

[32] A. K. Tehrani, M. Amiri, and H. Rivaz, "Real-time and high quality ultrasound elastography using convolutional neural network by incorporating analytic signal," *2020 42nd Annual International Conference of the IEEE Engineering in Medicine & Biology Society (EMBC)*, Jul. 2020. doi:10.1109/embc44109.2020.9176025

Chapter 4

4 Data Quality Analyzer – Towards Optimal Radio-frequency Frame Pair Selection for Ultrasound Elastography

A variant of this chapter will be submitted as a journal paper for publication in a yet to be decided journal.

4.1 Introduction

In elastography, it is well established that the quality of the stiffness image is highly dependent on the accuracy of the measured displacement field generated by displacement estimation algorithms. Many methods have been developed for tissue motion tracking where tissue displacements are estimated by processing US radio-frequency (RF) data of the tissue as acquired at two states of pre- and post-mechanical stimulation [1]–[8]. This is either done in real time, where the current frame is compared to some frame in the past, or by the acquisition of an RF data video before assessing all possible and reasonable frame pairs. However, all such methods generally assume that there is no significant out-of-plane movement of the tissue scatterers. However, this assumption is rarely met, and only select RF data pairs successfully fulfill this assumption. This leads to a situation where most data are entirely insufficient for the purposes of diagnostic imaging, and due to the massive number of possible frame pairs, manually analyzing the data is a laborious process which makes quasi-static elastography difficult to use.

In general, there are three major ways of overcoming this issue. One is through improving the quality of the data by creating new techniques for acquisition. The second pursues developing displacement trackers that are robust to inferior data. Finally, the third involves assessing the data quality in more efficient ways by allowing real-time imaging or developing automatic assessment tools. The first solution is less often pursued as it detracts from the low-cost convenient nature of ultrasound elastography by complicating the hardware setup. The second method is also widely pursued by integrating tissue

mechanics, smoothing, multiple frame-pairs, and other such methods to create robust estimators [9]–[16]. In general, however, the more robust the displacement estimator, the more computationally intensive it is to solve, hence, without extensive optimization, such estimators are difficult to use in the clinical setting. The final solution of allowing real-time assessment of data allows clinicians to assess data in a far more convenient way, lessening the clinical burden of manual assessment. In this chapter we propose a new method by which automatic assessment of data quality can be performed, allowing for a quantitative measure of data quality, and the ability to assess a series of RF frame pairs for at least initial assessment and pruning.

There are currently very few methods proposed to assess the quality of a pair of RF data frames acquired for tissue motion-tracking. Most of these methods are not displacement estimator agnostic, hence they cannot be used independent of the estimators' methodologies. For instance, PCA-GLUE was recently proposed for data quality assessment [17]. This is a machine learning based method developed using data pertaining to tissue mimicking phantoms and only 3 patients, thus it may not be rigorous for clinical applications. The current work seeks to develop a displacement-estimator agnostic methodology for assessing the quality of the displacement field for ultrasound elastography. Ideally, the methodology should run in near real-time rates to be useful as a data analyzer tool at the bedside. However, including automatic assessment of displacement quality allows for the analysis of an ultrasound RF-video after-the-fact. This relaxes the requirement for real-time operation, making the use of more computationally intensive displacement estimators more feasible. Moreover, this circumvents the requirement that the tool be installed on the ultrasound machine if RF data can be exported from the machine. These all make the clinical convenience and feasibility of the technique much better. Moreover, to provide a proper control protocol for this investigation, I aim to develop a way to purposefully contaminate synthetic data to simulate the effects of inadequate data acquisition. This data contamination method can also be used in the development of algorithms by checking their robustness against known data corruption.

To achieve the above proposal, a dataset pertaining to tissue-mimicking phantoms was created in-silico using finite element modelling and an ultrasound computer simulator

(FIELD II) facilitated by the methods proposed in Chapter 3. This data was generated to simulate various levels of data corruption generated by out-of-plane movement of scatterers. In addition to data quality assessment, this method can be employed for validating displacement estimators using data of more realistic quality, rather than relying on perfect in-silico synthetic data samples [9], [11], [18], [19]. This will allow for the development of more robust displacement estimators through quantifying the robustness of developed algorithms against out-of-plane displacement. Moreover, this method may allow for automatic tuning of user-defined parameters for other displacement algorithms.

In summary, this chapter seeks to provide two major contributions: A displacement estimator-agnostic methodology for assessing displacement quality and to provide a method for purposefully corrupting in-silico RF data to generate more realistic data for development of motion tracking methods. The methods proposed in this chapter can be further developed for optimal selection of paired frames of RF data aimed at generating high quality ultrasound elastography. Note that this method does not actually do anything to improve displacement estimates, but simply provides a quantitative way to evaluate the quality that already exists.

4.2 Methods

4.2.1 Overview of Proposed Method

The proposed method of displacement quality assessment assumes that RF signal decorrelation is the main contributor to the degradation of estimated displacement field. The source of this decorrelation is out-of-plane displacement of the tissue which results from the tissue mechanical stimulation in ultrasound elastography. The proposed assessment method is based on the premise that a perfect displacement field corresponding to two RF frames of pre- and post-deformation can be used to warp the pre-deformation RF frame to estimate the post-deformation RF frame with high accuracy. As such, to assess the accuracy of the displacement field, the ability of this field to regenerate the measured post-compression RF data frame can be assessed. This can be performed by measuring the similarity of the pre-deformation RF frame warped using the displacement field with the

measured post-compression RF frame used to estimate the displacement field. The higher this similarity the better the displacement field estimate.

4.2.2 Evaluation Algorithm

The proposed methodology centers around Equation 4.1 that describes the “perfect” displacement field, which collapses into Equation 4.2 if no out-of-plane displacements of the scatterers is assumed in the generated image.

$$S_2(x, y, z) = S_1(x + d_x, y + d_y, z + d_z) \quad 4.1$$

$$I_2(i, j) = I_1(i + d_i, j + d_j) \quad 4.2$$

Where d_x, d_y, d_z, d_i, d_j are functions which describe the displacement of the signal produced by the scatterers (S , which is the signal represented as a 3D function) and the change in location corresponding to the signal at the pixel described by (i, j) . I_1 and I_2 , are the pre- and post- compression RF data, respectively. The hypothesis is that the closer the displacement field in satisfying Equation (4.2), the better. This is well motivated as displacement estimators already consider a version of Equation 2 when generating the initial estimate [11], [15], [18], [20]–[22]. To evaluate this metric, the forward displacement operation is performed on I_1 , and is compared to the measured I_2 using the correlation between the two images and the mean-squared-error between the two.

This forward operation is achieved by considering the estimated displacement field as a geometric operation and performing the image warping to generate the signal produced by I_1 and the displacement field, which should be identical to I_2 in the perfect case. This method uses computationally inexpensive metrics and processes by posing the problem as a geometric operation.

4.2.3 Synthetic Data, Tissue Mimicking and Clinical Data

To verify that the algorithm works, FIELD II along with a finite element model to generate the ground truth displacements shown in Figure 4.1. The inclusion and background have a young’s modulus of $[X]$ and $[Y]$, respectively. Then, the radiofrequency

data were acquired by generating a random field of scatterers and solving the wave equation for the field of scatterers to generate the first RF frame I_1 . Then, using the ground truth displacement, the scatterers were moved according to the displacement at their location to generate the second RF frame I_2 (see Chapter 3 for more details).

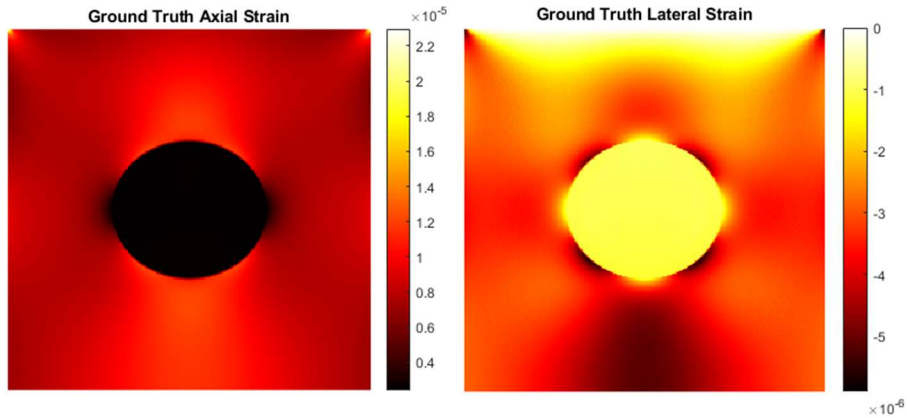


Figure 4.1 Axial and Lateral strain images for the ground truth finite element phantom with Young's Moduli X and Y for the inclusion and background, respectively.

To corrupt the data of the first RF frame I_1 with out-of-plane movement, a variable amount of out-of-plane displacement was added from a Gaussian distribution with 100 standard deviations ranging from 0-15mm, where 0 represents perfect data with no out-of-plane displacements. The forward model described earlier was used to warp frame I_1 to generate the second RF frame I_2 . As potential measures for accuracy and similarity with the target I_{12} , the MSE, Correlation, CNR, and SNR for each amount of corruption were recorded and analyzed. Moreover, the strain images generated from the displacement estimation was visualized for inspection of the degradation of quality.

To test the viability of this method in practice, RF videos of clinical breast cancer cases were analyzed pair-by-pair using the proposed method to find the best and worst frame pairs. Then the top 5 and bottom 5 pairs were visualized and manually assessed and compared in order to validate the capabilities of the algorithm. Histograms and tables for MSE and Correlation were generated for the clinical cases.

4.3 Results

Figure 4.2 illustrates the CNR, SNR, Correlation and MSE metrics for each corrupted synthetic data sample generated as described earlier, which henceforth is referred to as “warped” correlation and MSE. As expected, this figure shows that as the corruption increases, the metrics proposed for quality assessment decrease. As can be seen, the correlation and MSE worsen with corruption, and CNR and SNR become noisier with higher level of data corruption. Among the 4 metrics, CNR and SNR exhibit a highly oscillatory behavior at high level of decorrelation with no clear increase or decrease trend, indicating low reliability for RF frame pair quality assessment.

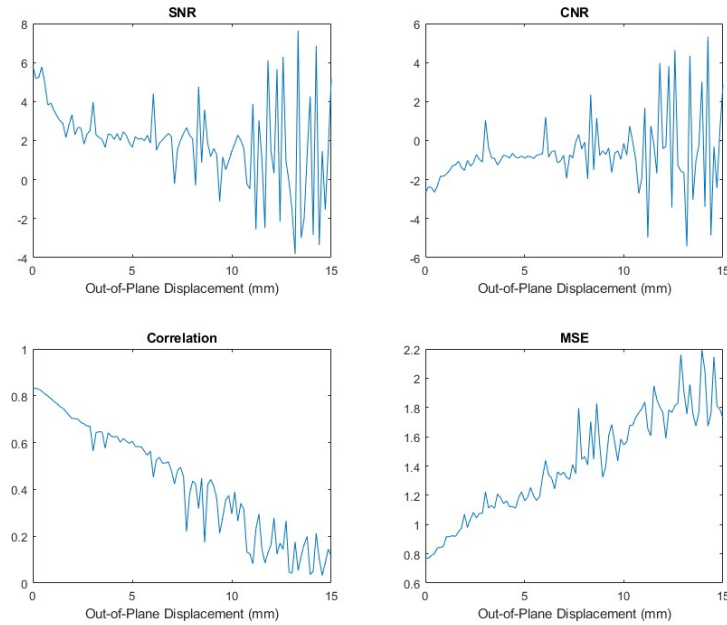


Figure 4.2 Metrics of quality as the out-of-plane displacement increases (standard deviation of out-of-plane displacement in mm) for the synthetic data. As the out-of-plane corruption increases, SNR and CNR become unreliable, while MSE and Correlation scores progressively get worse. Interestingly, at higher corruption levels we see less consistent trends.

Axial strain images were computed for various levels of out-of-plane displacement corruption. Figure 4.3 illustrates the progressive degradation of the generated axial strain images derived from the corrupted RF data of the synthetic data.

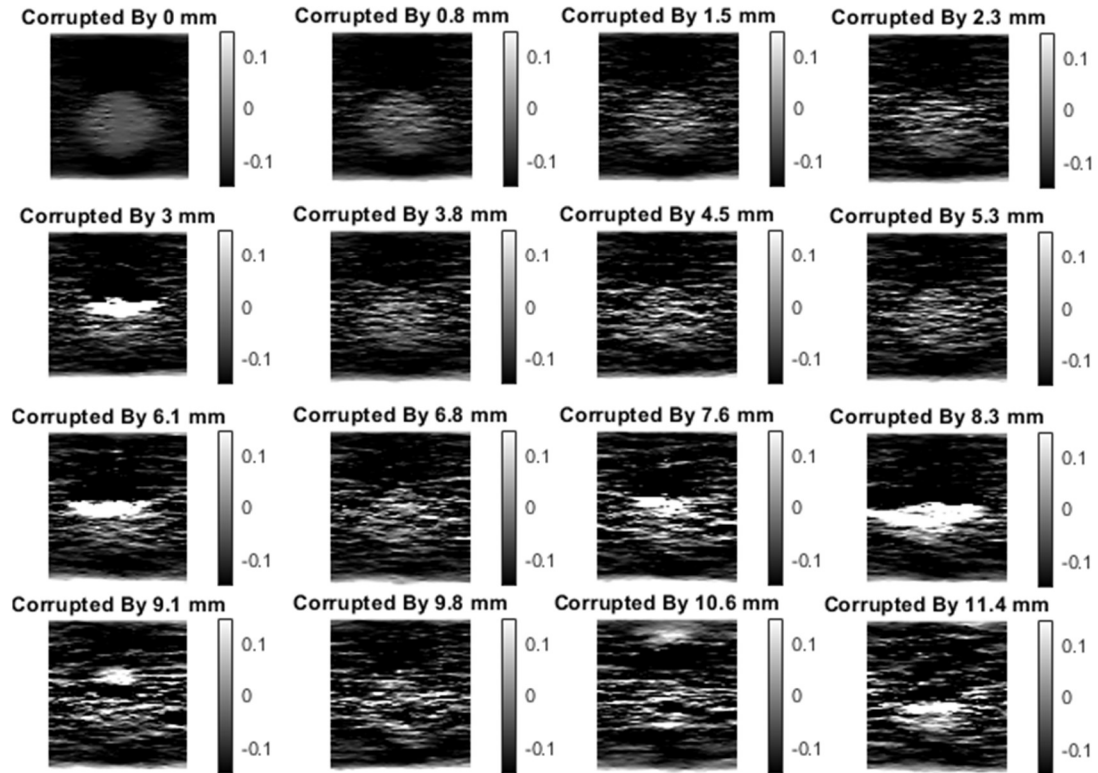


Figure 4.3 The progressive degradation of axial strain image quality and increased artefacts with increasing out-of-plane displacement data corruption of synthetic phantoms. The artefacts appear in the form of unrealistically high- and low-strain areas.

One may speculate that assessing the correlation between unwarped I_1 and I_2 maybe sufficient for assessing the quality of RF data frame pair while being computationally less expensive. To test this hypothesis, we calculated the correlation and MSE of I_2 and the unwarped I_1 , which was corrupted by the same variable levels of out-of-plane displacements this procedure without warping is henceforth known as naïve correlation. Figure 4.4 illustrates the variations of these parameters vs. out-of-plane displacement. As can be seen in this figure, “naïve” correlation and MSE show a similar pattern, however, the magnitudes of these parameters are much less desirable as they cover

small range of values, while the worsening pattern is much noisier and less reliable. As such, it can be concluded that using warping-based method is superior.

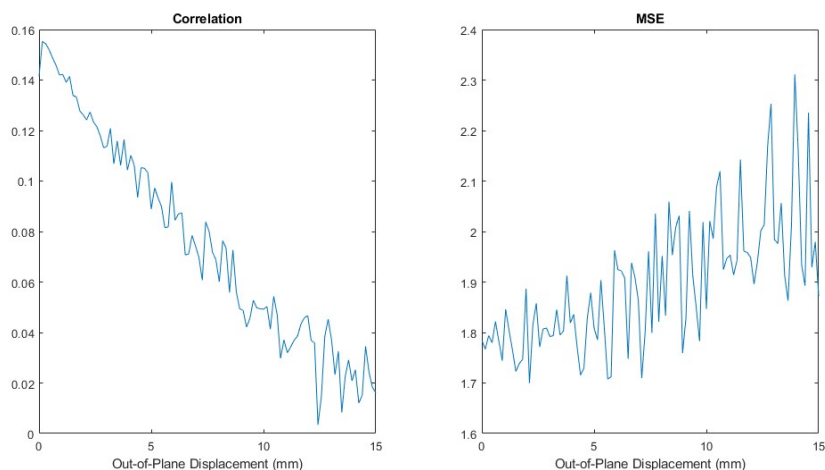


Figure 4.4 Correlation without warping shows a similar pattern to the warped correlation where correlation and mean squared error become progressively worse with increased out-of-plane displacement. Without warping however, the values for the errors are much less convincing, as correlation starts at 0.16. Therefore, warped correlation is a much more robust method than naïve correlation.

The following are two figures (Figures 4.6 and 4.9) which compare the top 5 ranked frame-pairs with the bottom 5 frame pairs. As can be seen, the top 5 frame pairs are far smoother and provide a much less obstructed view of the strain. In Figures 4.7 and 4.10 the histograms for all valid frame combinations can be seen, which shows a large bias towards low-quality frame combinations in clinical example 2 (Figure 4.10) while clinical example 1 (Figure 4.7) has a larger proportion of frame pairs with better correlation. Figures 4.5 and 4.8 are B-Mode images of the patient tumors shown in the strain images.

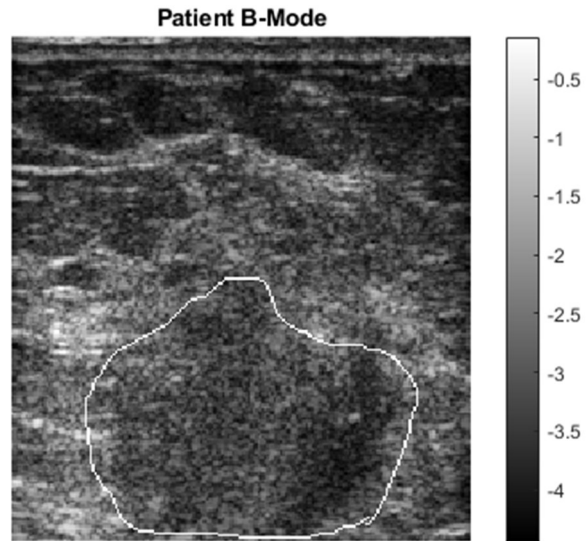


Figure 4.5 B-Mode image of the patient breast tumour, segmented by a clinician.

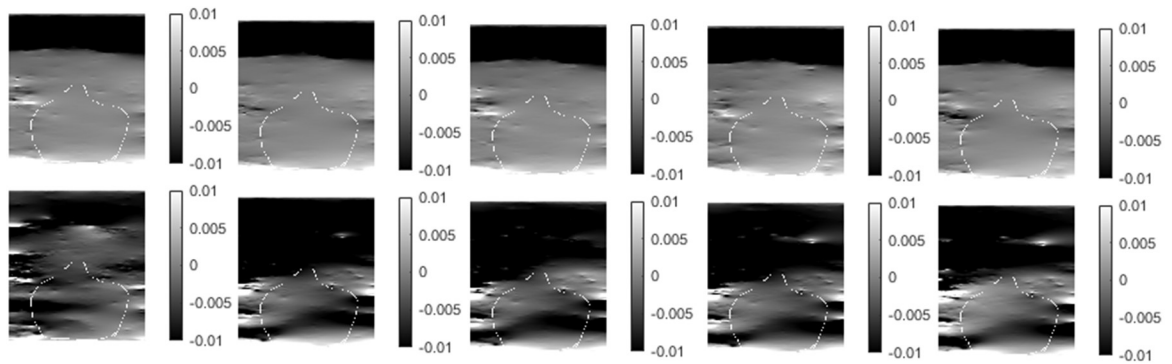


Figure 4.6 First clinical example for top 5 ranked frame-pairs (top) and bottom-5 frame-pairs (bottom row) as can be seen the low bottom 5 frame-pairs are inferior compared to the top 5. The tumour boundary is outlined in white.

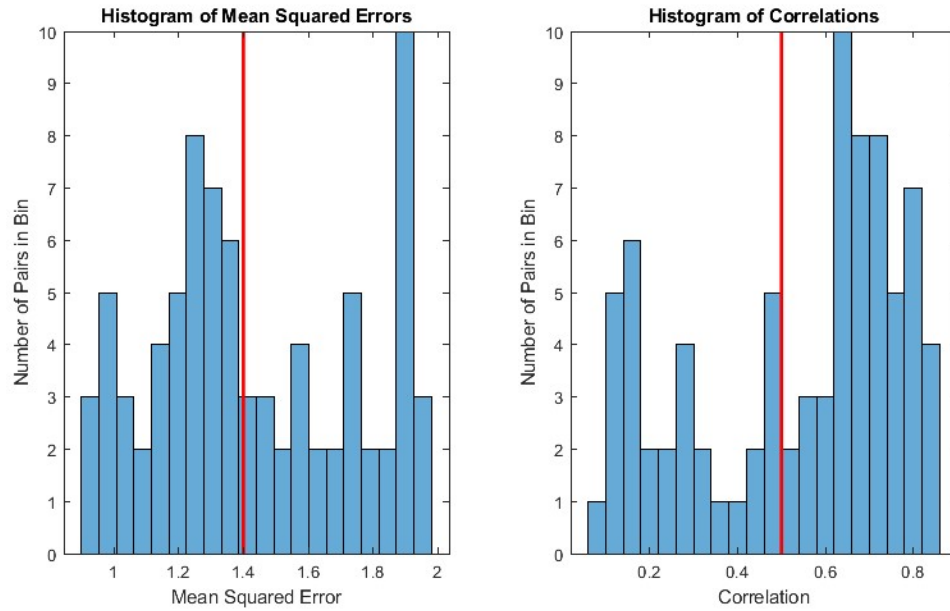


Figure 4.7 The histogram of mean squared error and correlation coefficients for each pair in clinical example 1. For this example, the majority of pairs are at least passable in terms of correlation coefficients, with the standard taken arbitrarily at 0.5 correlation and 1.4 MSE.

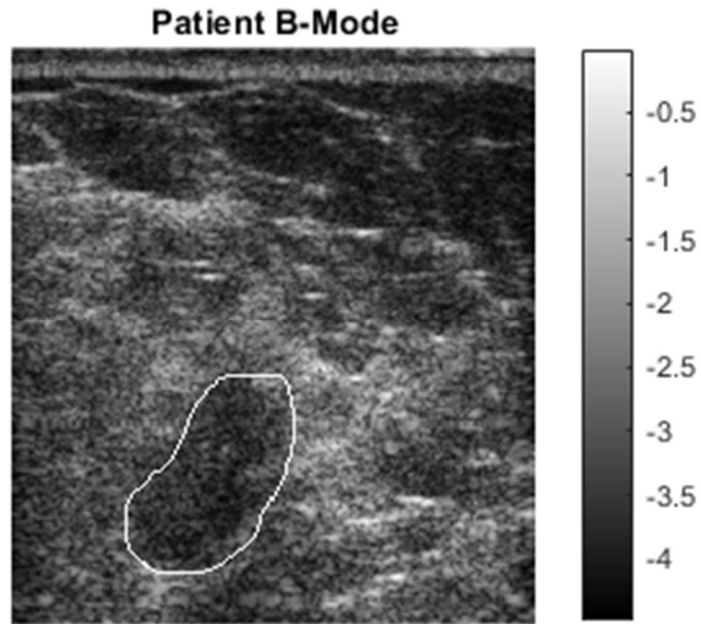


Figure 4.8 B-Mode image of the patient breast tumour, segmented by a clinician.

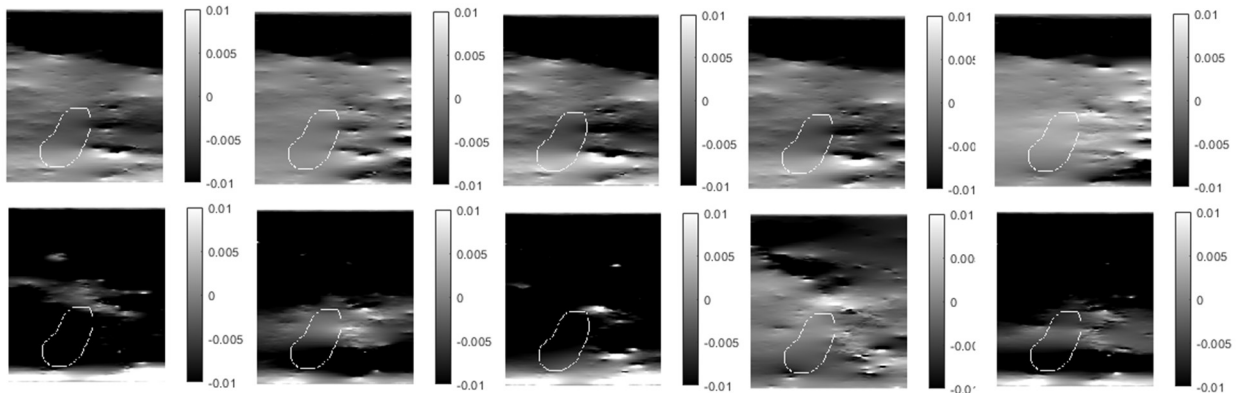


Figure 4.9 Second clinical example for top 5 ranked frame-pairs (top) and bottom-5 frame-pairs (bottom row) as can be seen the low bottom 5 frame-pairs are inferior compared to the top 5. The tumour boundary is outlined in white.

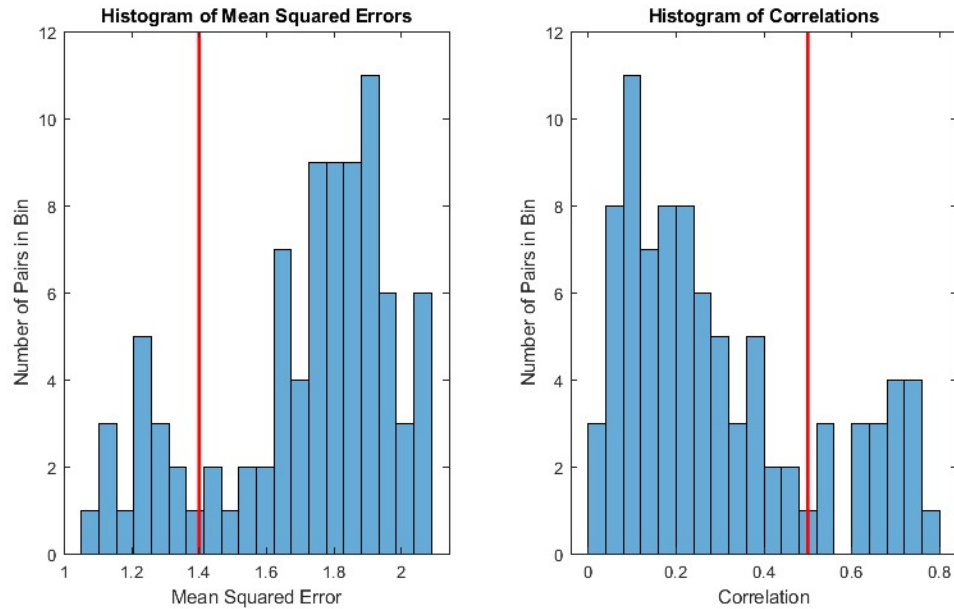


Figure 4.10 The histogram of mean squared error and correlation coefficients for each pair in clinical example 1. For this particular example, the majority of pairs are of very low quality and should not be used for elastography, with the standard taken arbitrarily at 0.5 correlation and 1.4 MSE.

Overall, as shown in Table 4.1, the top-5 frame pairs have overwhelmingly superior Correlations and MSE measures compared to the bottom-5 frame pairs, showing a high degree of contrast in the measures, especially with correlation coefficients, which range from 0 up to 0.8+ (Figures 4.6 and 4.8)

Table 4.1 Mean MSE and Correlation for top 5 and bottom 5 frame pairs for clinical examples 1 and 2, as can be seen, there is a considerable difference in error metrics between the two groups

Clinical Example	Mean MSE Top-5	Mean MSE Bottom-5	Mean Correlation Top-5	Mean Correlation Bottom-5
1	0.95	1.93	0.83	0.12
2	1.12	1.95	0.75	0.04

4.4 Discussion

The methodology presented has shown that it is quite sensitive to out-of-plane displacement contaminating the data acquired. Both the correlation and mean-squared-error show clear variation with increasing out-of-plane corruption in the synthetic data sample, while the CNR and SNR metrics proved unreliable in data corruption assessment. It is interesting to note that when the out-of-plane displacement increases, it is not simply a degradation of the SNR, but in fact as seen in Figure 4.2, there are increasingly larger and more unrealistically high-strain regions of the image. The reason for this is unknown, however we hypothesize that when there is a significant string of scatterers which have an out of plane displacement, the displacement tracking algorithms are led astray, which leads to regions of extremely high strain values. This also explains why CNR and SNR do not simply decay but lead to extremely high or extremely low values. More investigation into this may yield new ways to deal with the issue of out-of-plane strain. Moreover, the correlation and MSE metrics may allow for automatic or semi-automatic determination of parameters for displacement estimators, which are currently determined using ad-hoc methods [10], [11], [18], [20], [21]. The standard in this thesis was arbitrarily chosen to be

0.5 and 1.4 for Correlation and MSE, respectively. However, this needs to be determined for clinical data based on agreement to biopsy gold standards.

Unlike other methods [17] which use machine learning and are displacement estimator-specific, the proposed method requires no manual data labelling and is displacement estimator agnostic. This is helpful going forward, as this method can be used on any displacement estimation methodology developed in the future. However, due to our advancement in generating synthetic data, new datasets can be developed for training new methods by labelling data as “good” or “bad” based on the degree of out-of-plane displacements applied. This would allow for far larger datasets to be used in a variety of situations to train new displacement evaluation algorithms. Alternatively, each example could be compared to the ground truth displacement as a label. Nonetheless, purposefully corrupting synthetic data in a realistic way may open many doors for progress in ultrasound elastography.

Another objective of this investigation is to introduce a new method to simulate data corruption in a synthetic data sample generated in-silico to improve the realism of data generated from in-silico methods. As can be seen in Figure 4.2, the method proposed indeed simulates data corruption due to out-of-plane displacement due to the progressive decrease in image quality as out-of-plane displacement increases. It can even be compared to Figures 4.6 and 4.9, in the bottom row where we see similar artefacts which include areas of unrealistic high strain regions, like what can be seen in the high-corruption examples of Figure 4.3. Seeing similar artefacts in both the simulated and clinical examples is a good indication that the corruption method can be used to inform algorithmic design, as it appears to be capable of simulating some artefacts. Admittedly, applying a normally distributed out-of-plane component to the displacement is not very realistic, however, it does demonstrate the decrease in data quality. Future investigations can be carried out with more realistic out-of-plane displacements generated by analytical approximations or finite element modelling. Moreover, realistic operator errors such as rotation of the probe can be applied to the data. This can help propel the progress of quasi-static elastography significantly, as it now allows for more realistic synthetic modelling of the technique, leading to larger datasets for development and testing of displacement estimators.

Unfortunately, based on Figures 4.4 and 4.5, this methodology alone cannot definitively decide that a frame pair will generate a good diagnostic image, it can at least lessen the search window significantly by discarding obviously bad frame-pairs. Moreover, this allows for a second line of defense against false positives. As can be seen artefacts may erroneously appear very stiff, so the presence of inclusion can be disregarded if the scan quality metrics are low. Perhaps when combined with other methods such as [17], the performance will be improved. Moreover, methods could be developed which take into consideration manual outlining of an ROI from B-Mode images. For instance, SNR and CNR with outlining may distinguish between frames where the inclusion is visible and those that are not. There can also be filtering based on the number of frames which include non-physiologically high strain values, or measures of noise, like the norm of the Laplacian of the displacement field, or the divergence of the displacement field. The computed displacement field could also be checked against known tissue mechanical properties like incompressibility [26] using reasonable approximations for out-of-plane strain in order to punish significant deviations from plausible physical behaviour. Another avenue could be to design a deep learning based displacement estimator that simultaneously estimates the displacement field and labels it as either suitable or unsuitable [5-6], [9],[19], [24-26].

While one of the initial objectives of this paper was to alleviate the real-time requirement of elastography, this methodology can also be applied to give the clinician a real-time objective measurement of the quality of the observed strain image, which can be highly valuable in determining if an inclusion in the image is an artefact or indeed a tumor. By leveraging metrics that are already used in the calculation of the displacement estimate, this method can be made computationally free by simply saving and outputting intermediate values from the displacement estimation algorithm, which means that it would not impact the usability of any imaging system it is incorporated in.

Some future work must include extending these metrics with more ways of determining quality, particularly looking at analyzing and detecting artefacts, assessing smoothness, incorporating machine learning in a displacement-agnostic manner, and even potentially incorporating manual segmentation into the analysis.

4.5 References

- [1] A. Samani, J. Bishop, and D. B. Plewes, "A constrained modulus reconstruction technique for breast cancer assessment," *IEEE Trans. Med. Imaging*, vol. 20, no. 9, pp. 877–885, Sep. 2001, doi: 10.1109/42.952726.
- [2] A. Mallampati and M. Almekkawy, "Measuring Tissue Elastic Properties Using Physics Based Neural Networks," 2021. doi: 10.1109/LAUS53676.2021.9639231.
- [3] J. Jiang and B. Peng, "A Comparative Study of Displacement De-Noising Strategies: An in Vivo Feasibility Study Using 3D Whole Breast Ultrasound Data," 2018. Accessed: Aug. 24, 2022. [Online]. Available: <https://ieeexplore.ieee.org/document/8579998/>
- [4] T. A. Krouskop, T. M. Wheeler, F. Kallel, B. S. Garra, and T. Hall, "Elastic moduli of breast and prostate tissues under compression," *Ultrason. Imaging*, vol. 20, no. 4, pp. 260–274, 1998, doi: 10.1177/016173469802000403.
- [5] D. Perdios, M. Vonlanthen, F. Martinez, M. Arditi, and J. P. Thiran, "CNN-Based Ultrasound Image Reconstruction for Ultrafast Displacement Tracking," *IEEE Trans. Med. Imaging*, vol. 40, no. 3, pp. 1078–1089, 2021, doi: 10.1109/TMI.2020.3046700.
- [6] C. Hoerig, J. Ghaboussi, and M. F. Insana, "Data-Driven Elasticity Imaging Using Cartesian Neural Network Constitutive Models and the Autoprogressive Method," *IEEE Trans. Med. Imaging*, vol. 38, no. 5, 2019, doi: 10.1109/TMI.2018.2879495.
- [7] J. L. Gennisson, T. Deffieux, M. Fink, and M. Tanter, "Ultrasound elastography: Principles and techniques," *Diagn. Interv. Imaging*, vol. 94, no. 5, pp. 487–495, May 2013, doi: 10.1016/J.DIII.2013.01.022.
- [8] T. Varghese, "Quasi-Static Ultrasound Elastography," *Ultrasound Clin.*, vol. 4, no. 3, p. 323, Jul. 2009, doi: 10.1016/J.CULT.2009.10.009.
- [9] A. K. Z. Tehrani and H. Rivaz, "Displacement Estimation in Ultrasound

Elastography Using Pyramidal Convolutional Neural Network,” *IEEE Trans. Ultrason. Ferroelectr. Freq. Control*, vol. 67, no. 12, 2020, Accessed: Aug. 24, 2022. [Online]. Available: <https://ieeexplore.ieee.org/document/8990076/>

[10] H. S. Hashemi and H. Rivaz, “Global Time-Delay Estimation in Ultrasound Elastography,” *IEEE Trans. Ultrason. Ferroelectr. Freq. Control*, vol. 64, no. 10, pp. 1625–1636, Oct. 2017, doi: 10.1109/TUFFC.2017.2717933.

[11] M. Mirzaei, A. Asif, and H. Rivaz, “Combining Total Variation Regularization with Window-Based Time Delay Estimation in Ultrasound Elastography,” *IEEE Trans. Med. Imaging*, vol. 38, no. 12, pp. 2744–2754, Dec. 2019, doi: 10.1109/TMI.2019.2913194.

[12] H. Rivaz, E. M. Boctor, M. A. Choti, and G. D. Hager, “Ultrasound elastography using multiple images,” 2013, doi: 10.1016/j.media.2013.11.002.

[13] M. Mirzaei, A. Asif, and H. Rivaz, “Ultrasound Elastography Utilizing Pre-Beam-Formed Data,” 2019. Accessed: Aug. 24, 2022. [Online]. Available: <https://ieeexplore.ieee.org/document/8759302/>

[14] N. Mohammadi, M. M. Doyley, and M. Cetin, “COMBINING PHYSICS-BASED MODELING AND DEEP LEARNING FOR ULTRASOUND ELASTOGRAPHY”.

[15] M. Ashikuzzaman, T. J. Hall, and H. Rivaz, “Incorporating Gradient Similarity for Robust Time Delay Estimation in Ultrasound Elastography,” *IEEE Trans. Ultrason. Ferroelectr. Freq. Control*, vol. 69, no. 5, pp. 1738–1750, May 2022, doi: 10.1109/TUFFC.2022.3164287.

[16] A. Khadem and S. K. Setarehdan, “Smoothing-Spline based Strain Estimation in Ultrasound Elastography,” 2007. Accessed: Aug. 24, 2022. [Online]. Available: <https://ieeexplore.ieee.org/document/4728410/>

[17] A. Zayed, S. Member, H. Rivaz, and S. Member, “Fast Strain Estimation and Frame Selection in Ultrasound Elastography Using Machine Learning,” *IEEE Trans.*

Ultrason. Ferroelectr. Freq. Control, vol. 68, no. 3, 2021, doi: 10.1109/TUFFC.2020.2994028.

[18] M. Ashikuzzaman and H. Rivaz, “Second-Order Ultrasound Elastography With L1-Norm Spatial Regularization,” *IEEE Trans. Ultrason. Ferroelectr. Freq. Control*, vol. 69, no. 3, 2022, Accessed: Aug. 24, 2022. [Online]. Available: <https://ieeexplore.ieee.org/document/9674909/>

[19] X. Wei *et al.*, “Unsupervised Convolutional Neural Network for Motion Estimation in Ultrasound Elastography,” *IEEE Trans. Ultrason. Ferroelectr. Freq. Control*, vol. 69, no. 7, pp. 2236–2247, 2022, doi: 10.1109/TUFFC.2022.3171676.

[20] H. Rivaz, E. M. Boctor, M. A. Choti, and G. D. Hager, “Real-Time Regularized Ultrasound Elastography,” 2010, Accessed: Aug. 24, 2022. [Online]. Available: <http://www.cs.jhu.edu/~rivaz/UltrasoundElastography/>.

[21] H. Rivaz, E. Boctor, P. Foroughi, R. Zellars, G. Fichtinger, and G. Hager, “Ultrasound Elastography: A Dynamic Programming Approach,” *IEEE Trans. Med. Imaging*, vol. 27, no. 10, pp. 1373–1377, Oct. 2008, doi: 10.1109/TMI.2008.917243.

[22] H. Li, J. Porée, B. Chayer, M.-H. R. Cardinal, and G. Cloutier, “A global strain estimation algorithm for non-invasive vascular ultrasound elastography,” 2019. Accessed: Aug. 24, 2022. [Online]. Available: <https://ieeexplore.ieee.org/document/8925886/>

[23] N. Kheirkhah, S. Dempsey, A. Sadeghi-Naini, and A. Samani, “A novel tissue mechanics-based method for improved motion tracking in quasi-static ultrasound elastography,” *Med. Phys.*, vol. 50, no. 4, pp. 2176–2194, Apr. 2023, doi: 10.1002/MP.16110.

[24] Q. Zhang, Z. Cui, X. Niu, S. Geng, and Y. Qiao, “Image Segmentation with Pyramid Dilated Convolution Based on ResNet and U-Net,” *Lect. Notes Comput. Sci. (including Subser. Lect. Notes Artif. Intell. Lect. Notes Bioinformatics)*, vol. 10635

LNCS, pp. 364–372, 2017, doi: 10.1007/978-3-319-70096-0_38/FIGURES/5.

[25] A. K. Z. Tehrani, M. Sharifzadeh, E. Boctor, and H. Rivaz, “Bi-Directional Semi-Supervised Training of Convolutional Neural Networks for Ultrasound Elastography Displacement Estimation,” *IEEE Trans. Ultrason. Ferroelectr. Freq. Control*, vol. 69, no. 4, 2022, Accessed: Aug. 24, 2022. [Online]. Available: <https://ieeexplore.ieee.org/document/9694663/>

[26] A. K. Z. Tehrani, M. Amiri, and H. Rivaz, “Real-time and High Quality Ultrasound Elastography Using Convolutional Neural Network by Incorporating Analytic Signal,” 2020. Accessed: Aug. 24, 2022. [Online]. Available: <https://ieeexplore.ieee.org/document/9176025/>

Chapter 5

5 Conclusions and Future Work

The overarching goal of this thesis was to improve the practical feasibility of ultrasound elastography. The research aims include improving data quality, data collection workflow, and new algorithm development. In general, the problems with elastography stem from data quality issues, which are very difficult to address due to the lack of objective and automatic assessment. Another contributor to the problems is the lack of sufficient acquisition rates for real-time assessment. Moreover, this data quality issue plagues the development cycle of displacement estimators, as it is exceedingly difficult to tell whether the displacement algorithm does not perform, or if the data is of insufficient quality. This work proposes a series of optimizations, guides for algorithm selection, potential real-time imaging system design, a data quality analyzer module, and an open-source software package to generate highly realistic radiofrequency data. The summary of each chapter is summarized in the following sections.

5.1 Chapter 3 – A Comparison of Displacement Estimators

This chapter explores the currently available displacement estimators in the literature and describes an analysis of the quality to runtime ratio they provide with respect to the Young's modulus image. This is a novel and necessary investigation when going towards a clinically available system as more advanced displacement algorithms are too computationally intensive to run in real-time, and so an analysis of which displacement algorithm should be realistically implemented in a real system is a necessary question. Each displacement estimator was analyzed at the level of synthetic data, tissue-mimicking data, and clinical data. It was found that the simplest of the algorithms, AM2D preserves the most amount of detail in the Young's Modulus image with the lowest computational cost. A theoretical imaging system flowchart was proposed for a real system.

This chapter lays the groundwork for exploring what a design for a clinically viable imaging system would look like, a concept that is sorely lacking in the literature. Most publications look for increasingly complex algorithms which provide better results but are generally not considered in the context of what is technically, clinically, and commercially feasible. In this chapter, I showed that even very simple algorithms can produce clinically relevant images, at much lower computational requirements that are much more tractable for implementation into a prototype system. The construction of a clinical prototype also unlocks the realm of clinical validation for this technique, as the clinical and practical viability of quasi-static elastography remains unconvincingly validated. Moreover, clinical data usage allows researchers to target real bottlenecks in the imaging technique and can answer questions such as: Can QUSE actually avert the need for biopsy? Are clinicians comfortable relying on these images in lieu of a biopsy? Is the technique convenient enough to be integrated into the workflow seamlessly? All of which are essential questions to answer if QUSE is to be a widely used technique.

5.2 Chapter 4 – Elastosynth - An Open-Source software package for the generation of realistic in-silico data for ultrasound elastography

This chapter included an exposition of a new open-source software package which can be used to generate realistic radiofrequency data in-silico. It contains a procedural generation module which allows for the generation of arbitrarily heterogeneous phantoms, which can be simulated using a custom finite element solver, and then the radiofrequency can be simulated using FIELD II to calculate the propagation of sound through the tissues. This allows for the generation of known high-quality data to develop new displacement estimators.

The package and proposed methods overcome some of the most challenging obstacles in the development of these algorithms, including the lack of quality data and lack of ground truth comparisons for complex images. Due to the freehand nature of QUSE, data quality is exceedingly difficult to guarantee without looking at the resultant images. This begs the question of how we can validate our algorithm implementation on a clinical

level, as undesirable results can be due to algorithmic issues, or data quality issues. We can keep re-using known good clinical data, but this leads to bias and does not entirely solve the problem, as there is no way of knowing if the problem lies in the quality of the transducer. The innovation in this chapter creates sufficiently complex synthetic data which allows for isolation of potential issues: Data quality can be guaranteed, underlying tissue differences can be exaggerated, and a ground truth can be used to compare to. This will allow for far more robust development of algorithms than is currently possible. Moreover, the increase in computational efficiency allows for the generation of sufficient data to train deep learning models, which unlocks a wider range of techniques for QUSE.

5.3 Chapter 5 - Data Quality Analyzer – Towards Optimal Radio-frequency Frame Pair Selection for Ultrasound Elastography

This chapter proposes a methodology by which the underlying correspondence between pre-and post-deformation radiofrequency data can be compared to check the degree of decorrelation. This is proposed as a first-line assessment of data quality, as highly decorrelated frame-pairs are guaranteed to not yield quality data. The methodology includes a correlation metric which uses the estimated displacement field along with the pre-deformation RF data frame to generate a false post-deformation frame, and then compares it to the true post-deformation image RF data frame. In the ideal case, a perfect displacement image should yield a perfect correspondence to the post-compression image. Results show that on the aggregate, high correlation coefficient corresponds to smoother, higher quality images. This assessment can be performed in real-time and displayed at acquisition-time.

Whereas the previous work makes the development of arbitrarily complex phantoms possible, this work introduces ways to corrupt synthetic data in a more realistic manner. This is essential to quantifying the impact of out-of-plane movements in the formation of the QUSE image, to better understand how to perform QUSE, which was otherwise not possible. Moreover, by allowing for purposeful corruption of data, algorithms can be developed specifically to target this corruption, and in an environment

where the threshold at which the algorithm fails can be rigorously determined. This is a remarkable benefit compared to the current workflow, which does not allow for any quantitative analysis of robustness to out-of-plane movements.

5.4 Future Work

5.4.1 Chapter 2

This analysis has a significant flaw in the methodology, where the only synthetic samples used were homogenous inclusion with homogenous backgrounds. This leads to the problem where the algorithms' robustness to heterogeneity cannot be determined quantitatively. Therefore, this assessment should be re-run with heterogeneous synthetic data generated from elastosynth. This will further validate if indeed the simpler algorithms can be used in lieu of more advanced algorithms. Moreover, this can quantify the transfer function of the imaging system with respect to heterogeneity, allowing for much more realistic and informed interpretation of the images QUSE produces, as any exaggerations or underestimations of heterogeneity can be quantified and used to inform clinical interpretation of QUSE images. Nonetheless, the chief goal of future work would be to implement a clinical system and begin trials to better understand the clinical value of these algorithms.

5.4.2 Chapter 3

Generation of robust and realistic synthetic data is an essential capability to have when developing and validating the development of new elastography related algorithms. In this chapter a methodology for generating arbitrarily heterogeneous phantoms using custom transducers was presented as a novel way of creating extremely diverse in-silico datasets. This work could be expanded to include 3D finite element simulations using generic breast and liver anatomy, which would more accurately simulate a QUSE exam. Moreover, simulated inclusion shapes can be expanded using generative techniques to generate realistically shaped inclusions with clinically relevant features like integration into the tissues or highly irregular shapes. Moreover, there could be even further acceleration of the simulation process by involving GPU acceleration in the finite element simulation and the RF data simulation. Finally, different RF data simulators could be used

to more accurately solve the wave equation, although validation needs to be done to understand whether more accurate simulations have a material impact on the usefulness of the synthetic data.

Given the capacity of this software for large datasets, it is imperative that deep learning approaches to QUSE be explored in depth, ranging from displacement estimation, reconstruction, and potentially even diagnosis, as deep learning may have the potential to increase the clinical utility of this technique substantially, while leveraging GPU hardware accelerations.

5.4.3 Chapter 4

This methodology can be expanded with more and better motivated error metrics such as tissue-mechanics inspired metrics or methods that include B-mode image segmentation. Moreover, by including an optional function to provide a region of interest, the data quality analysis can be greatly improved, and may lead to trivial-time analysis of large quantities of data. However, the inclusion of ROI based measurements is potentially detrimental to the clinical convenience of the technique, so this should be validated by clinical usage to determine if the increased consistency is worth the extra work.

Some lower hanging fruit would be to improve the data corruption procedure to involve more realistic methods for determining out-of-plane movement. For instance, a constant-term displacement can be applied to all scatterers, simulating simple sliding of the probe. Applying rotation of the scatterers about the simulated probe can also capture any rotations of the probe while applying force. Both of these should improve the realism of data corruption. That being said, the gold standard for this would be to mount an accelerometer on a probe being used, and actually measure what realistic perturbations are in the application of force and use this information to generate out-of-plane displacements.

5.5 Closing Remarks

Overall, this work improves and consolidates the methodologies available to perform elastography. Starting from orders of magnitude improvement in the runtime of image improvement algorithms which allows for real-time high-quality imaging, this new methodology could reduce the runtime of more sophisticated displacement estimators significantly. Moreover, by comparing currently available displacement estimators, we create a framework for the selection of algorithms in a clinical system. To further smooth out the development cycle of displacement estimators, I propose a software package to generate realistic in-silico data with an established ground truth. Finally, A data analyzer was developed for initial assessment of displacement estimates to improve the data quality problem. Overall, these advancements should facilitate the development of a clinically viable next generation quasi-static elastography system, which can then go on to clinical testing and validation.

6 Curriculum Vitae

Matthew Caius

EDUCATION AND AWARDS

Master of Engineering Science in Biomedical Engineering

May 2022 – Present

Bachelor of Medical Science (*Honors Specialization in Medical Biophysics*)

Sept 2018 – May 2022

RESEARCH EXPERIENCE

Developing a Novel Reconstruction Technique for Tissue Incompressibility

Sept 2023 – Present

Western University, London, Ontario

- Expand Young's Modulus reconstruction technique to simultaneously reconstruct the incompressibility (Poisson's Ratio) of tissue

Cataloguing and Evaluation of Ultrasound Elastography Methods

Sept 2022 - Present

Western University, London, Ontario

- Implement and optimize the current elastography algorithms
- Evaluate performance of the currently available algorithms in a full stiffness reconstruction application
- Collaboration with another lab out of Concordia University to aid in the development of new displacement estimators

Optimization and Extension of Mechanics-Based Elastography Regularisation Algorithm

May 2022 – Sept 2022

Western University, London, Ontario

- Optimized previous PhD student's image processing algorithm for a **360 000x** speed improvement
- Implemented customizable level of image improvement to allow for real-time operation
- Expanded the capabilities of the algorithm by including more tissue mechanics
- Directed and supervised a summer student for the extension of the algorithm

Machine Learning Estimation of Out-of-plane Strain in Ultrasound Elastography

June 2021 – May 2022

Western University, London, Ontario

- Employed advanced image processing techniques to extract and process breast geometry from breast MRI images, including segmentation, edge detection, and non-rigid registration
- Mesh refinement using MATLAB and open-source tools prior to non-linear finite element simulation of breast tissues using ABAQUS CAE
- Used MATLAB and ABAQUS to generate dataset of expected breast deformation during an ultrasound exam including a variety of breast geometries and probe positions
- Optimized dataset generation scripts, achieving >50% reduction in total compute time
- Designed and implemented statistical finite element modelling by training a neural network and PCA model to predict the expected deformation in a novel situation
- Concisely wrote a scientific report on the project, articulating the significance of the model, the prerequisite background information, methods, results, and limitations of the model

Machine Learning Ultrasound Elastography Model **Fall 2020 – Sept 2021**

Western University, London, Ontario

- Conducted machine learning evaluation of ultrasound radiofrequency data using both feature engineering followed by traditional machine learning and deep learning
- Inter-disciplinary co-operation with software engineering students to create both front-end and back-end software to facilitate the use of the model
- Implementation and design of traditional machine learning, leveraging cloud-based machine learning solutions like Microsoft Azure to select the optimal model
- Memory and runtime optimization of deep learning model for expansion to a larger dataset

EMPLOYMENT

Engineering Teaching Assistant **Sept 2022 – Present**

Western University, London, Ontario

- Aided in the instruction of >50 students per class by marking and facilitating assignments, proctoring, demonstration, and tutoring.
- Biomechanics, Data Structures and Algorithms, Programming, Introduction to Engineering Design

Founder and Director of Biomedical Software Start-Up **May 2022 – Present**

Caius Medical, Newmarket, Ontario

- Biomedical software company specializing in contracting services for medical and scientific compute.
- Finite Element Modelling, Agent Based Modelling, GPU and hardware acceleration
- Developed using Python, C#, C++